Chem Soc Rev

REVIEW ARTICLE

View Article Online
View Journal | View Issue

Check for updates

Cite this: *Chem. Soc. Rev.*, 2020, **49**, 6694

Spectroscopy, microscopy, diffraction and scattering of archetypal MOFs: formation, metal sites in catalysis and thin films†

Miguel Rivera-Torrente, Laurens D. B. Mandemaker, Matthias Filez, Guusje Delen, Beatriz Seoane, Florian Meirer and Bert M. Weckhuysen *

Metal–organic frameworks (MOFs) are a class of porous crystalline materials showing great potential for applications such as catalysis, gas storage, molecular separations, energy storage and drug delivery. The properties that render them interesting stem from their structure (*e.g.* morphology, porosity or metal coordination and geometry). Thus, gaining a deeper understanding strongly relies on the availability and adequate use of advanced characterization tools, which can interrogate MOFs under realistic synthesis as well as catalysis (or sorption) conditions. Herein, we present an overview of the various characterization techniques specifically suitable for the study on the underlying chemistry of the formation mechanisms and adsorption properties of three archetypal MOFs, namely MIL-100, ZIF-8 and HKUST-1. A section on using MOFs as supports for metal atoms or complexes that can be used for catalysis on the robust Zr_6 nodes of UiO-66 or NU-1000, and the characterization techniques used thereof, is presented as well. In addition, we discuss recent developments on the application of nano-spectroscopic characterization for MOF thin-films and explore the potential of MOFs as model systems in catalysis. The conclusions and outlook provide future research possibilities in the field of MOF characterization.

Received 30th May 2020

DOI: 10.1039/d0cs00635a

rsc.li/chem-soc-rev

Open Access Article. Published on 20 August 2020. Downloaded on 2/16/2026 6:59:12 AM.
This article is licensed under a Creative Commons Attribution 3.0 Unported Licence.

1. Introduction

Since their early discovery in the 1990s, metal–organic frameworks (MOFs) have been researched with ever-increasing pace in their marked properties for gas sorption and catalysis.[1–5] To unravel the chemistry of MOF formation and functioning and establish novel structure–function relationships, a toolbox

Inorganic Chemistry and Catalysis, Debye Institute for Nanomaterials Science, Utrecht University, Universiteitsweg 99, 3584 CG Utrecht, The Netherlands. E-mail: b.m.weckhuysen@uu.nl

† Electronic supplementary information (ESI) available: Details on the bibliometric study on tools for MOF characterization. See DOI: 10.1039/d0cs00635a

Miguel Rivera-Torrente

Miguel Rivera-Torrente holds a BSc in Chemistry from Universidad Autónoma de Madrid (UAM) in Spain and a MSc in Chemical Engineering from the University of Strasbourg – École de Chimie, Polymères et Matériaux (ECPM), France. After research stays at BASF and RWTH Aachen (Germany) he pursued a PhD in spectroscopy of metal–Organic frameworks at the Inorganic Chemistry and Catalysis Group of Utrecht University (The Netherlands). He currently works in different areas of catalysis, materials science and polymer chemistry as a Senior Research Specialist in Dow.

Laurens D. B. Mandemaker

Laurens D. B. Mandemaker received his BSc and later MSc degree in Chemistry from Utrecht University (The Netherlands) for the work performed on zeolites using in situ spectroscopic techniques in the Inorganic Chemistry and Catalysis Group. Currently, he is doing a PhD under the supervision of Prof. Bert M. Weckhuysen at Utrecht University. His research focusses on combining microscopic and spectroscopic tools to study the growth, performance and deactivation of metal–organic framework films in gas-sorption or as catalysts.

This journal is © The Royal Society of Chemistry 2020

Open Access Article. Published on 20 August 2020. Downloaded on 2/16/2026 6:59:12 AM.
This article is licensed under a Creative Commons Attribution 3.0 Unported Licence.

of characterization techniques has been assembled and proven crucial for the knowledge build-up in the past decades. Further advances are still required though, particularly to elucidate the gaps in our understanding to better exploit MOF properties and develop protocols for obtaining application-tailored MOFs from this unexplored design space. Despite the significance of this field and the number of research reports, an overview and perspective of advanced MOF characterization tools is, to the best of our knowledge, lacking. Several review articles focused on a single or narrow selection of characterization techniques have been published, including: transmission electron microscopy (TEM),[6] magnetic,[7–12] X-ray[13–15] and vibrational[16,17] spectroscopies. One example of a broader view was provided by Howarth *et al.*,[18] in which a selection of routinely used characterization tools was discussed, such as X-ray diffraction (XRD), thermogravimetrical analysis (TGA) and N_2 physisorption, responding to the need of establishing good practices for a fair comparison of MOF reports in the field.

This review article presents a critical overview of the variety of advanced spectroscopic,[6,7,19–24] scattering and microscopy tools that can be applied in a state-of-the-art way to characterize the most commonly studied MOFs. This approach aims to establish a framework of thinking for moving towards a more complete set of characterization techniques for understanding synthesis, sorption and catalysis in MOFs; by expanding the number of available characterization tools and exemplifying

Matthias Filez

Matthias Filez studied Chemical Engineering and Physics at KU Leuven (Belgium). He received his PhD in 2015 at Ghent University (Belgium) with Prof. Guy B. Marin and Prof. Christophe Detavernier on the "Alternative Design of Pt-based Catalysts: An X-ray Spectroscopic View". After his PhD, he continued as postdoctoral researcher in the group of Prof. Bert M. Weckhuysen at Utrecht University (The Netherlands), where he obtained a Marie Skłodowska-Curie fellowship. Currently, he is postdoctoral researcher in the groups of Prof. Christophe Detavernier (UGent, Belgium) and Prof. Maarten B. J. Roeffaers (KU Leuven, Belgium), where his research focusses on novel approaches in metal nanocatalysis.

Guusje Delen

Guusje Delen is a PhD candidate in the Inorganic Chemistry and Catalysis group at Utrecht University (The Netherlands). Prior to her PhD, she obtained her BSc and MSc degree In Nanomaterials, Chemistry and physics at Utrecht University. She obtained her MSc degree for a thesis on the synthesis of Fe based catalysts for Fischer–Tropsch synthesis. In her PhD under the supervision of Prof. Bert M. Weckhuysen, she focuses on Nano-Spectroscopy of Surface-Anchored Metal–Organic Frameworks.

Florian Meirer

Florian Meirer obtained his ScD degree (2008) in technical physics from the TU Wien (Vienna University of Technology) under Prof. Christina Streli. After postdoctoral stays at the Stanford Synchrotron Radiation Lightsource, USA, (Erwin Schrödinger Fellowship, FWF) and the Fondazione Bruno Kessler, Italy (Marie-Curie cofund fellowship), he moved to Utrecht to work on spectroscopic and spectromicroscopic methods for solid catalyst characterization. He is currently a tenured Assistant Professor and his fields of research include spectromicroscopy and data mining and chemometrics in the fields of heterogenous catalysis and environmental analysis.

Bert M. Weckhuysen

Bert Weckhuysen received his master's degree in chemical and agricultural engineering from Leuven University (Belgium) in 1991. After obtaining his PhD from Leuven University in 1995 under the supervision of Prof. Robert Schoonheydt, he has worked as a postdoc with Prof. Israel Wachs at Lehigh University (USA) and with Prof. Jack Lunsford at Texas A&M University (USA). Weckhuysen has been since 2000 a full professor of inorganic chemistry and catalysis at Utrecht University (The Netherlands). His research interests are in the development of spectroscopy and microscopy techniques for elucidating the working and deactivation principles of catalytic solids, often applied under true reaction conditions.

Open Access Article. Published on 20 August 2020. Downloaded on 2/16/2026 6:59:12 AM.
This article is licensed under a Creative Commons Attribution 3.0 Unported Licence.

their current and future possibilities. We present different showcases where the use of advanced characterization tools is required to decode the complexity of MOF chemistry. Specifically, the most noteworthy traits of three MOFs in their bulk and film forms, namely MIL-100/MIL-101, MAF-4/ZIF-8/ZIF-67 and Cu_3BTC_2/HKUST-1. These topologies have shown potential in catalytic and sorption applications, and had a huge impact on the development of the field throughout the last 20 years.[25] In particular cases, relevant reports in which other topologies (or even composites) have been studied are highlighted together with the most suitable techniques used to study their properties.

2. Chemistry and characterization of archetypal metal–organic frameworks

A large number of topologies have been breakthroughs in MOF chemistry, *e.g.* MOF-5, UiO-66, MFM-300, MIL-53, MOF-74 or CPO-27, MIL-88, MIL-127, NH_2-MIL-125, NU-1000, MOF-808, CAU-10-H, MFU-4l, DUT-5 and many others; following stability and performance criteria, as well as fundamental discovery. The reports on these structures and their properties have boosted the research on microporous crystalline materials with unprecedented properties. For instance, one important feature of MOFs, which differs from those of metal oxides or zeolites, is their flexibility, that endows them with the capacity of expanding or contracting upon gas sorption.[26–28] We advise the curious reader to consult the excellent reviews on the characterization tools authored by Kitagawa *et al.*,[29–33] Férey *et al.*,[34,35] Fletcher *et al.*,[36] Murdock *et al.*[37] and Schneemann *et al.*[26] This is also the case with the chemistry of defects and defect-engineered MOFs, recently reviewed by Fang *et al.*[38] and Dissegna *et al.*[39] which presents a major challenge for the spectroscopist or diffraction expert, but with the potential reward of unravelling fascinating phenomena useful for catalysis, redox chemistry or gas sorption. Other very important aspect that is inherent to the relatively dynamic nature of coordination bonds is metal exchange and mixed-metal MOFs. Again, detailed literature is available in the reviews published by Lalonde,[40] Deria[41] and Evans *et al.*,[42] or Dincă *et al.*[43] and Abedanatanzi *et al.*[44] Another field of recent interest, sparked mainly by Bennett and others,[45–50] is the development and study of disordered and amorphous MOFs. Inspired by those, we have recently shown that,[51] understanding disorder may be of paramount importance for, for example, metal particle deposition. However, for a more detailed analysis and due to their higher practical advantages for technical applications, we have restricted this review article to three (MIL-100/MIL-101, ZIF-8/ZIF-67 and HKUST-1) archetypal MOF topologies for which a vast array of techniques has been used, as described hereafter. Three important aspects that have been deeply studied on these structures are: the formation mechanisms (*e.g.* crystallization and assembly), the formation and chemistry of coordinatively unsaturated sites (CUS) (including changes of the oxidation state of the metal center), and the diffusion of gases within the pores, as well as the interaction of those with metal and linker sites. These points will be addressed by showcasing relevant studies published for the mentioned topologies, as well as briefly outlining their implications in catalysis and gas sorption. Additionally, as highlighted by the groups of Corma[52] or Gates,[53] MOFs offer an excellent platform to be used as supports for metal atoms and complexes in (model) catalysis by post-synthetic modification. Thus, a section addressing the tools and hurdles of characterizing such systems is presented. In this sense, one way of minimising mass transfer issues and reducing the amount of material employed, as well as studying new fundamental properties, is by using thin-films, which are often more difficult to characterize than bulk materials. Section 5 critically discusses the necessity of using micro- and nanoscopy tools for the spatially resolved characterization of MOFs, as demonstrated for other microporous functional materials.[54–56] This selection was made following a bibliometric analysis of relevant literature (*ca.* 2000 research articles and reviews) in the specific MOF fields in which the authors have been working on in the past years. The analysis was carried out based on the appeareance of keywords (see the ESI† for more details), and the papers grouped depending on the features that they study and the techniques used. This allowed us to pinpoint the techniques, mainly X-ray based, but also with spatially resolved tools with nanometric resolution, *i.e.* nanoscopy, that may be interesting to use in the coming years for the study of MOFs and will be discussed in the concluding section.

2.1 Chemistry and characterization of MIL-100 and MIL-101

MIL-100 and MIL-101 have been intensively studied since they were first reported by Férey *et al.* in the mid-2000s as some of the most stable structures to date.[57,58] They consist of 1,3,5-benzenetricarboxylate (BTC) and 1,4-benzenedicarboxylate (BDC), respectively, and μ_3-O-centered trinuclear inorganic clusters $[M_3(\mu_3\text{-}O)(O_2C\text{-}R)_6]$, where M = Cr^{3+}, Fe^{3+},[59] Al^{3+},[60] $V^{3+/4+}$,[61] Sc^{3+},[62] Ti^{3+},[63,64] Mn^{3+}[65] or In^{3+}.[66] In the as-synthesized form, each metallic centre is in an octahedral environment coordinated by one μ_3-O atom, shared with the other two metallic centres building the cluster, four oxygen atoms from the organic linker and one terminal ligand (Fig. 1). While two metallic octahedra per cluster are typically coordinated by terminal aqua ligands, the third terminal ligand is an anionic species, that may be either a hydroxyl ligand or a halide anion (such as F^- or Cl^-, depending on the synthesis conditions), needed to compensate the negative default charge per inorganic cluster of the framework. The μ_3-O-centered trinuclear clusters are then linked through the organic moieties to form hybrid super tetrahedra, which further assemble into a 3D porous framework having the zeolite **MTN** topology. This MOF topology possesses two different types of mesoporous cages of 25 Å and 29 Å (MIL-100) and 29 Å and 34 Å (MIL-101), delimited by microporous pentagonal and hexagonal windows of 5 Å and 8.6 Å (MIL-100) and 12 Å and 14.7 Å (MIL-101). Depending on the metal and the activation procedure, MIL-100 and MIL-101 have been reported to possess BET areas up to 2300 and 4100 $m^2\ g^{-1}$, respectively, exceptional hydrothermal stability and a relatively high thermal stability. This set of properties, together with the presence of coordinatively unsaturated metal

 This journal is © The Royal Society of Chemistry 2020

Open Access Article. Published on 20 August 2020. Downloaded on 2/16/2026 6:59:12 AM.
This article is licensed under a Creative Commons Attribution 3.0 Unported Licence.

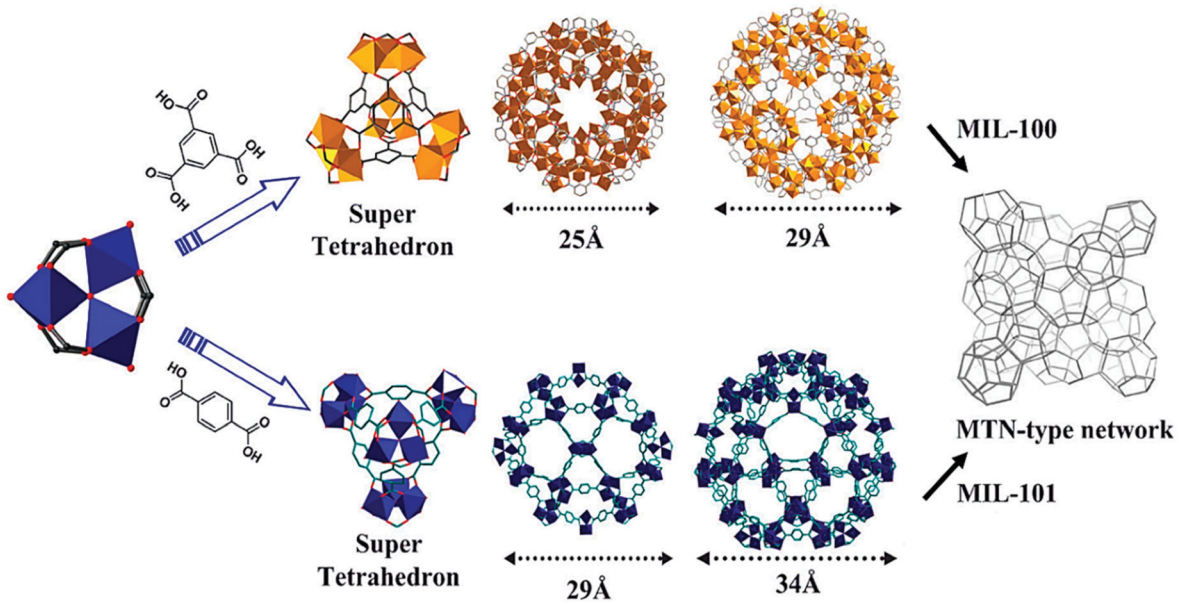

Fig. 1 Structure of MIL-100 and 101 formed by μ_3-O-centered trinuclear metallic clusters linked through the organic linker into a supertetrahedron, which further assembles into a porous framework having the MTN topology. Reproduced from ref. 84. Copyright©2012 Royal Society of Chemistry.

sites (CUS) in the inorganic secondary building units (SBU) upon activation and the presence of mesoporous cages, makes these frameworks one of the topologies of choice for study in different fields.[67]

2.1.1 Formation mechanism of MIL-100 and MIL-101. During the last decade several studies have been reported in order to gain understanding into the MOF formation mechanism.[68–75] This understanding is of utmost importance, given the level of unpredictability in MOF synthesis where, often, subtle changes in the synthesis conditions results in a completely different reaction product, leaving minimal room for a rational design.[76–78] A comprehensive overview on the different *in situ* studies on the crystallization of MOFs and on the different techniques available to study the formation of crystalline materials can be found in the book recently published by Kaskel[93] and in the reviews by Attfield *et al.*,[68] and Pienack *et al.*[86] This understanding is even more important for those cases in which several MOFs can be obtained from the same precursors under similar synthesis conditions, as it is the case for MIL-53, MOF-235 and MIL-101; or MIL-96, MIL-110 and MIL-100.[76] One interesting approach to achieve a higher degree of control over MOF synthesis is the use of pre-defined SBUs so that under certain conditions a specific inorganic cluster can be obtained, allowing for the rationalization, to some extent, of the MOF synthesis. Thus, different studies have been devoted to examining the stability of some known SBUs under hydro-/solvothermal synthesis conditions. One of the most studied SBUs has been the μ_3-O-centered trinuclear unit observed in different MOFs,[79] such as MIL-100[57] and MIL-101[58] or the flexible MOFs MIL-88 (or MOF-235) and MIL-89,[80] as well as extended and functionalized isoreticular analogues thereof.[81,82] Surblé *et al.* provided spectroscopic evidence of the stability of this trinuclear inorganic unit during MIL-89(Fe) crystallization for the first time.[83]

In particular, the authors used Fe K-edge EXAFS and observed the presence of trimeric iron oxide SBUs at the different stages of the MIL-89 synthesis. XAS is indeed a very powerful technique to study the MOF formation mechanism at early stages of crystallization, providing information concerning the type, number and distance of neighbouring atoms for a specific element.[86] Further insight into the stability of the trimeric iron oxide units upon MIL synthesis was obtained by Birsa Čelič *et al.*[87] The authors studied the synthesis of MIL-45(Fe) and MIL-100(Fe) from the same precursors using different solvent compositions (water or water/acetone) by XAS and Mößbauer spectroscopy at several reaction times. Interestingly, upon acetone addition a change in the iron oxidation state from Fe^{3+} to Fe^{2+} was observed upon heating, leading to the dissolution of the previously formed amorphous iron complexes. The instability of this SBU in certain solvent compositions has a pronounced effect: acetone cannot stabilize the trimeric cluster and leads to the formation of MIL-45(Fe), containing undulating chains of $Fe^{II}O_6$ octahedra. In water, MIL-100(Fe) is obtained where the Fe^{3+} based trimeric units remain unaltered throughout the crystallization process.

These examples clearly illustrate the significance of understanding the local environment of the different species present at different stages of the synthesis. However, in addition to this, it is also important to examine crystal growth over length scales of several orders of magnitude in order to build up a complete picture of crystallization. Moreover, although *ex situ* and pseudo *in situ* experiments, as those describe above, provide critical information, the interpretation of the results must be done carefully, since the delicate balance of species in solution might be altered prior to the data acquisition. In this sense, *in situ* SAXS/WAXS are a powerful tool, with SAXS providing information regarding the size, shape and surface of the

Open Access Article. Published on 20 August 2020. Downloaded on 2/16/2026 6:59:12 AM.
This article is licensed under a Creative Commons Attribution 3.0 Unported Licence.

particles and WAXS about their crystalline properties, both in a time-resolved fashion.

Further, the use of synchrotron radiation allows the study of the synthesis under harsh conditions, what facilitates the study of reactions *in situ*. Stavitski *et al.* and Goesten *et al.*[85,88] combined *in situ* SAXS and WAXS to gain insight into the NH_2-MIL-53(Al) and NH_2-MIL-101(Al) crystallization process. In line with previous observations by Millange *et al.* by energy-dispersive XRD,[75,89] the authors observed the formation of the NH_2-MOF-235(Al) intermediate (Bragg peak observed at $Q = 6.3\ nm^{-1}$, Fig. 2) prior to the appearance of NH_2-MIL-53(Al) and NH_2-MIL-101(Al). Moreover, the study of the influence of different synthesis parameters, *i.e.* solvent composition (H_2O/DMF ratio), temperature and concentration of precursors, on the MOF crystallization enabled the evaluation of the different factors governing the NH_2-MIL-53(Al) and NH_2-MIL-101(Al) formation. Specifically, the solvent composition was proven to play a key role, not only on the kinetics, but also on the sequence of events taking place during MOF synthesis. On the one hand, DMF increases the linker solubility compared to water, being the dissolution of the organic linker a rate-limiting step of the crystallization process at high H_2O/DMF ratios. On the other hand, DMF seems to stabilize the intermediate phase NH_2-MOF-235(Al), and the use of pure DMF is required in order to obtain NH_2-MIL-101(Al).

So as to gain further understanding into the role DMF plays, Goesten *et al.*[90] applied *in situ* ^1H and ^{27}Al NMR[91] to the NH_2-MIL-101(Al) synthesis and supported their observations by DFT calculations. While DFT modelling shows that DMF stabilizes the μ_3-O-centered inorganic cluster present in MOF-235 and MIL-101,[90,92] in line with previous observations by X-ray scattering (*vide supra*), *in situ* NMR indicates a more complex role of the solvent. In particular, the results pointed to the formation of a stable H–Cl–DMF complex that molecularly promotes the NH_2-MOF-235(Al) to NH_2-MIL-101(Al) transformation. The authors proposed that this complex supplies the required hydroxido ligands, which are not present in the NH_2-MOF-235(Al) inorganic cluster, but that are present in that of NH_2-MIL-101(Al), through a water dissociative mechanism (Fig. 3).

Furthermore, with this information at hand, the authors refuted their previous assumption of a dissolution–recrystallization mechanism for the NH_2-MOF-235(Al) to NH_2-MIL-101(Al) transformation and proposed that the transition occurs in the solid state instead. This conclusion is further supported by the previously obtained SAXS data, from which a constant scatterer volume, morphology and intensity were observed. The data points to the formation of amorphous 25 nm scattering entities prior to the measurements, whose long-range order continue to evolve at constant volume so that Bragg peaks corresponding to

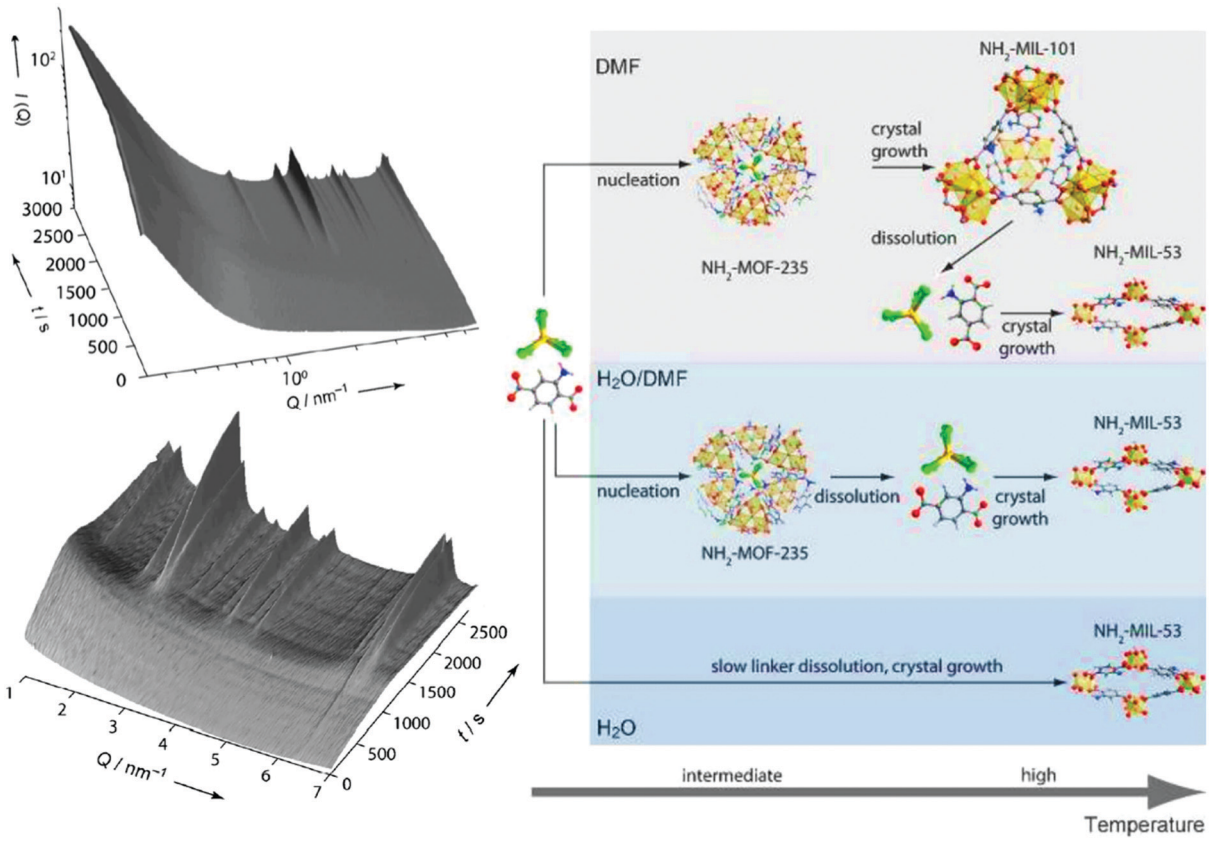

Fig. 2 Left: *In situ* 3D Small Angle X-ray Scattering obtained during the crystallization of NH_2-MIL-101(Al) at 403 K using DMF as solvent. Right: Sequence of events taking place during the NH_2-MIL-53(Al) and NH_2-MIL-101(Al) crystallization processes under different synthesis conditions. C: grey, H: white, N: blue, O: red, Al: yellow, Cl: green. Reprinted with permission from ref. 85. Copyright©2011 John Wiley & Sons, Inc.

Open Access Article. Published on 20 August 2020. Downloaded on 2/16/2026 6:59:12 AM.
This article is licensed under a Creative Commons Attribution 3.0 Unported Licence.

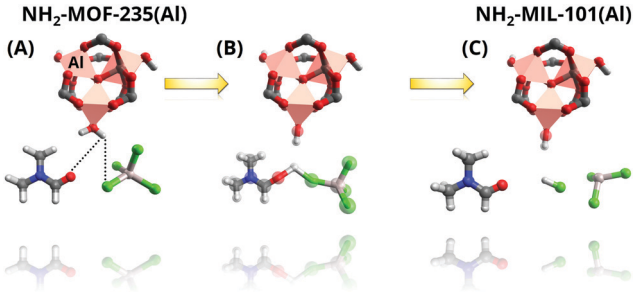

Fig. 3 Representation of the NH_2-MOF-235 to NH_2-MIL-101 transformation mechanism promoted by the complexation of axial H_2O coordinated to octahedral Al, DMF with Cl^- anions as proposed by Goesten *et al.* (A) Interaction of O in DMF and Cl^- in $AlCl_4^-$ abstract a proton from H_2O in axial position (B), leading to the formation of (C) OH hydroxy species as ligand. Colour code: pink, octahedra, Al; grey, C; red, O; white, H; blue, N; green, Cl. Adapted from ref. 90. Copyright©2014 American Chemical Society.

NH_2-MIL-235(Al) and NH_2-MIL-101(Al) started appearing at 500 and 1500 s, respectively.

Although this section is not intended as a survey of all the different *in situ* methods available to study the formation of crystalline materials, nor as an exhaustive overview on the current insight into the formation of MOFs (for those we refer the reader to the works authored by Pienack,[86] Walton[93,94] and Attfield *et al.*),[68] the examples above demonstrate that combining various synchrotron and non-synchrotron-based techniques is essential if a complete picture of the MOF crystallization is desired. Indeed, given the challenge of fully understanding the different chemical and physical events taking place during the synthesis, at all relevant length-scales.[95,96] The combination of simultaneously operating, complementary techniques would allow to study the formation mechanism in one single experiment, avoiding possible reproducibility issues and facilitating the correlation of the different data. These types of systems have been already successfully used to study the synthesis of traditional porous materials,[96] but they remain largely unexplored in the case of MOFs.[97]

2.1.2 Generation of coordinatively unsaturated sites upon MOF activation in MIL-100: Lewis and Brønsted acidity. One remarkable feature of MOFs is the ability of some structures to possess coordinatively unsaturated metal sites (CUS), which can act as Lewis acid sites. For instance, MIL-100 and MIL-101 have been reported to exhibit CUS upon removal of the terminal ligands present at the apical positions of the metallic octahedra forming the inorganic μ_3-O-centered clusters (*vide supra*). It is well established that the formation of CUS can strongly influence the catalytic and adsorptive properties of MOFs, and thus may be highly desirable for different applications. It is then obvious that gaining insight into the coordination and nature of their metallic species, their interaction with different guest molecules, and how these correlate with MOF properties; is essential to optimize MOF performance.[98] In this respect, Vimont *et al.*[99] studied the nature of the terminal ligands coordinating the chromium atoms in MIL-100(Cr) (Scheme 1), with chemical composition $(Cr^{III}_3OF_{0.85}(OH)_{0.15}(H_2O)_2)_2{\cdot}nH_2O$, as a function of the MOF outgassing temperature by *in situ* infrared spectroscopy. Upon degassing at 573 K, only two bands were observed in the 3700–3000 cm^{-1} range: the stretching modes of Cr–OH species and the aromatic C–H of the terephthalate moieties (at 3585 cm^{-1} and 3090 cm^{-1}, respectively), with no ν(OH) bands ascribed to water. The absence of bands in the 5400–5000 cm^{-1} range, in which the $\nu + \delta(H_2O)$ combination mode of water is present, point to the generation of open metal sites at this activation temperature. When the degassing temperature was decreased to 423 K and 373 K, new bands appeared in the 5300–5200 cm^{-1} and 3800–3500 cm^{-1} ranges, attributed to the formation of two different water species coordinated to the unsaturated metal sites (species 1 and 1′ in Table 1 and Scheme 1). The formation of two different species was related to the metal centres heterogeneity, ascribed by the authors to a heterogeneous distribution of the anionic terminal ligands (in this case fluoride anions), being 0, 1 or 2 per trinuclear inorganic cluster.[58] When the outgassing temperature was further decreased, new bands were observed, which corresponded to the appearance of new Cr–H_2O/H_2O water species, not directly bound to the metal, but H-bonded to the previously adsorbed Cr–H_2O water species instead.

In contrast to MIL-100(Cr), for which CUS with one single oxidation state were observed, *i.e.* Cr^{3+}, the IR spectra acquired for MIL-100(Fe) showed two different bands at 618 and 597 cm^{-1}, corresponding to the $\nu_{as}(Fe^{3+}{}_3O)$ and $\nu_{as}(Fe^{2+}{}_3O)$ vibrations modes, respectively.[100] This partial reduction of iron at higher outgassing temperatures was further confirmed by ^{57}Fe Mössbauer spectroscopy and it was related to the partial removal of terminal anionic ligands at 523 K (Scheme 1). In the case of MIL-100(Al), IR spectroscopy and solid-state NMR studies pointed to a different scenario, in which only one of the two terminal aqua ligands per trinuclear cluster can be removed.[101,102] This different behaviour was related to the presence of different impurities, in particular NO_3^- from the metal salt used for the MOF synthesis and H_3BTC, probably coordinated to the aluminium open metal sites.

In a further step, several research groups evaluated the Brønsted and Lewis acid sites (BAS and LAS, respectively) of different MIL-100 analogues by infrared spectroscopy using different basic probe molecules. To this end, carbon monoxide (CO) is one the most widely used probe molecules to evaluate protonic acidity. When probing BAS, the lone pair of CO interacts *via* σ-donation with OH groups, leading to shifts in both ν(OH) and ν(CO) IR bands, so that the larger the shift, the stronger the acidity. M–OH species (only observed for Al and Cr-based analogues, but not in the case of MIL-100(Fe) and MIL-100(V)) gave rise to $\Delta\nu$(OH) = 90 and 86 cm^{-1} for MIL-100(Cr) and MIL-100(Al), respectively, showing a fairly weak acidity, close to that of silanol groups in silicalite ($\Delta\nu$(OH) = 100 cm^{-1}), regardless of the metal used. Among the different hydroxyl groups (either hydroxyl groups belonging to the framework, *i.e.* M–OH, or to water molecules, *i.e.* M–H_2O or M–H_2O/H_2O species), the highest Brønsted acidity was observed for the M–H_2O species, where the water molecules were located in the cation coordination sphere.[103] In this case, the $\Delta\nu$(OH) value was

Open Access Article. Published on 20 August 2020. Downloaded on 2/16/2026 6:59:12 AM.
This article is licensed under a Creative Commons Attribution 3.0 Unported Licence.

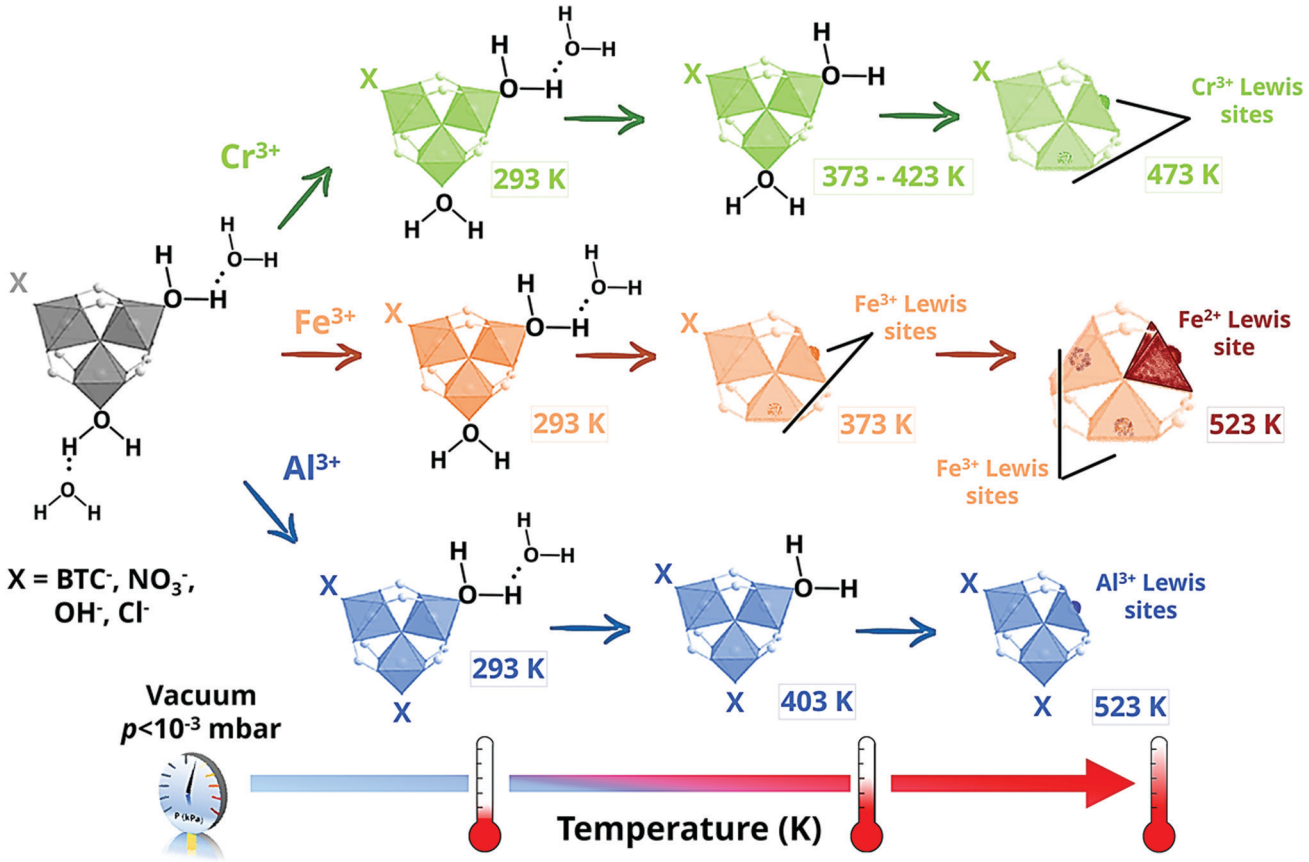

Scheme 1 Location and interaction of water molecules and formation of the open metal sites present in the metal–oxo trimers of MIL-100(M); where M = Cr (top, green), Fe (middle, orange) and Al (bottom, blue), as a function of the MOF outgassing temperature for different for different MIL-100 analogues.

Table 1 IR bands assigned in literature to different water species of MIL-100(Cr) upon dehydration. Reprinted with permission from ref. 99. Copyright©2006 American Chemical Society

Water species	$\nu_3(\nu_{as})$ [cm^{-1}]	$\nu_1(\nu_s)$ [cm^{-1}]	$\nu_2 + \nu_3$ [cm^{-1}]	$\nu_2(\delta_{H_2O})$ [cm^{-1}]
$H_2O \rightarrow Cr^{3+}$ (species 1)	3700	3608	5274	1596
$H_2O \rightarrow Cr^{3+}$ (species 1′)	3683	3595	5265	1604
$H_2O\cdots H_2O \rightarrow Cr$ (species 2)	3680	3588	5252	1603
$H_2O\cdots H_2O \rightarrow Cr$	3670	2950	5320	1650

Table 2 Quantification of coordinatively unsaturated sites reported by Vimont *et al.*,[99] Leclerc *et al.*[100] and Volkringer *et al.*[102] for different MIL-100 analogues together with the wavenumbers of several coordinated probe molecules on the different frameworks

MIL-100 analogue	M^{2+} CUS [μmol g^{-1}]	M^{3+} CUS [μmol g^{-1}]	Total M CUS [μmol g^{-1}]
$MIL\text{-}100(Cr)_{523K}$	—	3500	3500
$MIL\text{-}100(Fe)_{423K}$	45	1895	1940
$MIL\text{-}100(Fe)_{523K}$	850	2810	3660
$MIL\text{-}100(Al)_{523K}$	—	1800	1800

M^{3+} cation in MIL-100	ν(CO) [cm^{-1}]	CD_3CN ν(CN) [cm^{-1}]	C_5H_5N ν_{18} [cm^{-1}]
Cr	2207, 2200, 2196	2305	1015
Fe	2192–2173	2304	1014
Al	2195–2184	2326–2321	1018

160 cm^{-1}, close to that of alkali-exchanged faujasite ($\Delta\nu$(OH) = 160 cm^{-1}) or P–OH groups of phosphated silica ($\Delta\nu$(OH) = 180 cm^{-1}). Interestingly, as demonstrated by Vimont and co-workers, this Brønsted acidity can be modified by substituting the coordinated water by different OH-containing organic molecules, paving the way to the fine tuning of the acidic properties of MOFs.[104] Furthermore, BAS can be converted into LAS upon framework dehydration, which can be also probed with different probe molecules (Table 2). A thorough study has been recently published by Hall and Bollini, in which they demonstrated that $M^{3+}\cdots OH$ Brønsted sites should be more carefully studied.[105] They used pyridine (Py) and 2,6-di-*tert*-butylpyridine (DBTPy) sequentially to distinguish between how Lewis or Brønsted sites play a role in acetalization reactions. This type of studies should be used as a model for other MOFs, such as Zr_6 containing topologies, in which acidity is also a recurrent topic.[106–111]

In the case of MIL-100(Fe) two different ν(CO) bands were observed in the 2170–2166 cm^{-1} and 2192–2173 cm^{-1} ranges, which characterized CO adsorbed on Fe^{2+} and Fe^{3+} CUS, respectively.[112] Moreover, for MIL-100(Al) half of the CUS calculated for MIL-100(Cr) and MIL-100(Fe) were obtained, in

Open Access Article. Published on 20 August 2020. Downloaded on 2/16/2026 6:59:12 AM.
This article is licensed under a Creative Commons Attribution 3.0 Unported Licence.

line with the presence of different impurities previously observed by infrared and NMR spectroscopy (see above).[102]

In another study, Gómez-Pozuelo *et al.* quantified the number of Lewis sites of the isoreticular materials MIL-100 by means of CD_3CN.[113] The number was lower than those reported in Table 2 although similar activation procedures were used, the reason for this discrepancy remaining unknown. This series of works highlight the importance of a thorough characterization of MOFs' open metal sites since the different activation conditions, coordinated molecules or chemical composition influence the nature, concentration and strength of the framework acid sites. IR spectroscopy is a widely available experimental tool that, upon adsorption of different probe molecules, has been intensively used to evaluate the strength and quantify the amount of acid sites in different traditional porous materials.[114] As described above, this approach has also been successfully applied to MOFs, yet some differences should be borne in mind. Although some strong bases have been commonly used to assess the acidity of many solid materials, its use to study MOF acidity can be problematic. For instance, in the case of pyridine, vibration modes sensitive to interaction with acid sites often overlap with those of the framework.[102,103] Moreover, the preparation of self-supporting discs often needed to perform the experimental measurements might not be trivial for some of the aforementioned materials, given the pressure-induced amorphization reported for different MOFs.[115] Although this issue is commonly overlooked, and the preparation of self-supported discs is often found in literature, the deposition of the sample by drop casting on silicon wafers is recommended for those cases in which the stability of the MOF may be a problem.

In addition to its use for evaluating the acidity of MOFs, infrared spectroscopy has also been proven as a powerful tool to study the interaction of CUS with different adsorbates. For instance, Leclerc *et al.*[100] examined the influence of the different open metal sites present in MIL-100(Fe), *i.e.* Fe^{2+} and Fe^{3+}, on the adsorption of several probe molecules, particularly CO, propene and propyne, able to interact through π-backdonation, and CO_2, pyridine and propane, not able to provide such interaction. IR spectroscopy pointed to a more important role of Fe^{2+} CUS, despite their weaker acidity, due to their ability to strongly interact with CO, propene and propyne *via* π-backdonation, as indicated by the redshifts observed in the ν(C–O), ν(C=C), ν(C≡C) and ν(≡CH) bands. Indeed, the additional electron in Fe^{2+} d-orbitals enables the formation of more stable metal–adsorbate complexes by the transfer of electron density from the d orbitals of the Fe^{2+} metal centres to the π* antibonding orbitals of certain molecules. Yoon *et al.*[116] and Wuttke *et al.*[112] took advantage of the stronger interaction of Fe^{2+} CUS with unsaturated gas molecules, and studied the separation of propene from propane through breakthrough experiments using equimolar propene:propane mixtures. Specifically, Wuttke *et al.* applied *in situ* IR spectroscopy and studied the propene:propane separation performance with and without selectively poisoning the Fe^{2+} CUS. In line with previous studies, the adsorption capacity of C_3H_6 is markedly higher without blocking the Fe^{2+} CUS, leading to separation factors over 100, which drop to 5.3 upon Fe^{2+} NO poisoning.

Further insight into the adsorption of different molecules can be obtained through variable-temperature infrared (VTIR) spectroscopy, which, as shown by Palomino *et al.*[117] for H_2 adsorption on MIL-100(Cr) and MIL-101(Cr), allows for the determination of the corresponding values of standard adsorption enthalpy (ΔH_0) and entropy (ΔS_0).

Two special cases for understanding formation of CUS and binding properties in the MIL-100 series are the Sc and the Al analogue, in which solid-state NMR was particularly useful. Resonance-Echo Double-Resonance (REDOR) NMR techniques allow to calculate internuclear distances and dipolar coupling of different nuclei based on the difference in dephasing radio-frequency of a given pair of nuclei, *e.g.* ^{13}C–^{15}N or ^{29}Si–^{27}Al. It allowed Giovine *et al.*[118] to calculate the effect a number of parameters affected on both H and C when degassing the Sc^{3+} centres in MIL-100(Sc) and prove the formation of penta-coordinated sites upon dehydration. A comparison with Sc_3BTB_2 (BTB = 1,3,5-tris(4-carboxyphenyl)benzene), which shows similar Sc sites, was established, and combining DFT calculations and multinuclear techniques (namely, Resonance-Echo Saturation-Pulse Double-Resonance (RESPDOR ^{13}C–{^{45}Sc}), 2- and 3-dimensional Multi-Quantum Magic Angle Spinning (2-3D MQ-MAS ^{45}Sc–{^{1}H}) and Cross-Polarization (CP MAS)), they were able to quantify the number of Sc^{3+} CUS based on their coordination numbers and the asymmetric polarization of the $Sc_3(\mu_3\text{-O})$ clusters. In some cases, additional techniques such as EPR have been combined with NMR for characterizing CUS in MIL-100 materials, allowing the authors to reach conclusions that could not be drawn from vibrational techniques. For instance, Barth, Hartman and others[119] studied the adsorption of NO in MIL-100(Al) by means of DRIFTS, multinuclear NMR and EPR spectroscopies. In a fist instance, they observed NO interacting weakly with the π-electrons of the aromatic linkers (band at 1861 cm^{-1}); and physisorbed and gaseous NO (1854 and 1874 cm^{-1}, respectively). However, while no evident bands pointing to [$Al^{3+}\cdots$NO] adducts were observed in the DRIFTS spectra, EPR showed that electrophilic Al^{3+} can polarize NO and transform it into NO^+. Moreover, evolution of adsorbed species could be studied as a function of temperature to corroborate that hypothesis. Such type of weak ionic interactions cannot be detected efficiently by FT-IR, but coupling EPR and DFT calculations allowed for an accurate description of this issue.[120] In order to avoid any confusion with different Al adsorption sites, ^{27}Al{^{1}H} heteronuclear correlation (HETCOR) upon dehydration of the MOF was used in another work,[121] showing the presence of $Al(OH)_3$ deposits that play a minor role in NO adsorption. In brief, even for a complex case of weak, ionic interactions, the authors were able to obtain an accurate description by adding magnetic spectroscopy to vibrational techniques. Further, not only bonding but also the dynamics of the adsorbed probe can be studied by means of 2D NMR, *e.g.* rotational motions of pyridine on Al^{3+} or Al–OH sites or the effects of adsorbates on the backbone.[122,123] This has been also successfully employed in different frameworks,[124–126] sometimes being able to discriminate between competing adsorbing molecules of very similar nature.[127]

Open Access Article. Published on 20 August 2020. Downloaded on 2/16/2026 6:59:12 AM.
This article is licensed under a Creative Commons Attribution 3.0 Unported Licence.

Thus, beyond the use of well-known basic probe molecules to study MOF acidity (*e.g.* pyridine, CO, CH_3CN), the use of other types sensitive to redox or ionic sites (*e.g.* NO, TEMPO) as well as the implementation of more sophisticated approaches, such as *operando* studies, provides mechanistic insight into catalytic, adsorption or separation processes, allow for the identification active species and even enable the evaluation of their thermodynamics. The development of cells that can combine different techniques, *e.g. in situ* XAS, XRD and FT-IR is currently under investigation by a number of groups and will certainly become more important in the coming years.[128] Rivera-Torrente *et al.* and others have shown the importance of studying CUS formation and the fate of the network upon activation for catalytic purposes *in situ* spectroscopy tools.[129,130] This approach will increasingly become important as MOFs are used as platforms and precursors of active catalysts.

2.2 Chemistry and characterization of MAF-4 or ZIF-8

Zeolitic imidazolate frameworks (ZIFs) are a subfamily of MOFs characterized by the use of imidazolate linkers as organic ligands so that the M–Im–M (M stands for the metal, such as Zn or Co, and Im for the imidazolate linker) angle is close to 145°, similar to the Si–O–Si angle commonly found in zeolites. This feature leads to the formation of MOFs with zeolite-like topologies, including not only those observed in zeolites, but also predicted structures not yet experimentally realized.[131–138] Among the different ZIFs, ZIF-8[139] (also known as metal azolate framework 4, or MAF-4)[134] consists of Zn^{2+} (Co^{2+} in the case of its analogue ZIF-67) and 2-methylimidazole (MeIm), where the metallic centres are tetrahedrally coordinated to four imidazolate N atoms, giving rise to an open framework with an augmented sodalite zeolite-like topology. As shown in Fig. 4, this topology possesses sodalite-like β-cages of 11.6 Å interconnected by hexagonal pore apertures of 3.4 Å, in principle able to screen between different molecules.[139–141] This feature, together with the easy synthesis of ZIF-8, its good adsorption properties and its remarkable chemical and thermal stabilities, has drawn the attention of the scientific community, being ZIF-8 one of the most studied MOFs.

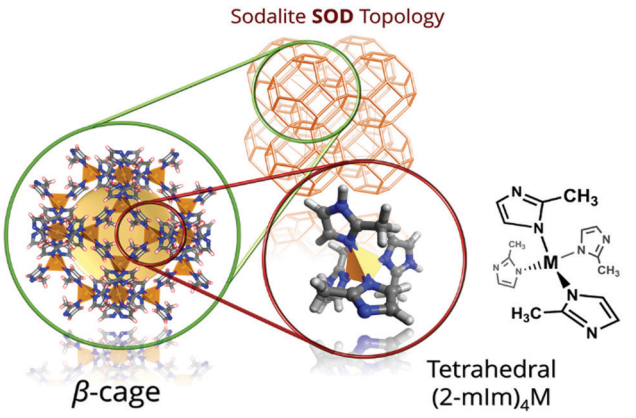

Fig. 4 Structure of ZIF-8 sodalite (SOD) net. On the left, the sodalite-like β-cage (11.6 Å) with the yellow sphere representing the van der Waals surface within the pore, and with the ZnN_4 tetrahedra highlighted on the right.

2.2.1 Formation mechanism of MAF-4 or ZIF-8. The interest ZIF-8 has risen has prompted the development of a plethora of synthetic routes mainly driven by the principles of "Green Chemistry"[142] and the attractive concept of crystal engineering.[143–145] For instance, ZIF-8 has been synthesized from RT up to 413 K, in few minutes or during several weeks, in different solvents and using different additives, and the particle size has been varied from 10 nm to single crystals of several hundred microns in size.[146–148] Hence, given the easy and flexible synthesis of ZIF-8, this system has often been chosen as a model system so as to gain understanding into the MOF crystallization mechanism and kinetics, as well as to identify the main parameters affecting the synthesis and MOF properties. In this sense, different studies have been carried out in which different *in situ* techniques, such as time-resolved static light scattering (TR-SLS),[141,146] SAXS and WAXS[149] and energy-dispersive XRD[148,150–154] as well as *ex situ* techniques like SEM, TEM and XRD have been used to unveil the ZIF-8 synthesis mechanism. Moreover, electrospray ionization mass spectrometry (ESI-MS) has also been used so as to analyse the species present in solution at different stages during the MOF formation, allowing for the correlation of these species with the crystals growth and nucleation.[155] These techniques have provided a wealth of information regarding the ZIF-8 synthesis mechanism, the nucleation and growth kinetics, the possible crystallization pathways (Fig. 5) as well as the role that different synthesis parameters play, such as the ligand to metal ratio or the use of additives, on the particle size and morphology and MOF synthesis.

Several prominent examples have been already discussed within this review (MIL-100 and MIL-101 section) to illustrate the need of combining different techniques to unveil the MOF formation mechanism at all relevant length scales as well as the important role of *in situ* methods to avoid quenching, which may result in changes to the system. In this section, we aim to highlight the use of different microscopy techniques as powerful complementary analytical tools for studying MOF crystallization. Next to the use of TEM for *ex situ* measurements, Patterson *et al.*[156] used liquid cell transmission electron microscopy (LCTEM) for the real-time monitoring of MOF synthesis for the first time. In particular, the authors studied the synthesis of ZIF-8, proving LCTEM is a suitable technique to gain insight into the MOF synthesis kinetics, the underlying MOF formation mechanism and the influence of the synthesis conditions on the particle size and morphology. From the LCTEM ZIF-8 synthesis direct observation (Fig. 6), it became evident that particle growth does not take place through particle coalescence, in line with previous SAXS/WAXS results by Cravillon *et al.*[157]

Furthermore, the growth exponents, calculated from the evolution of the particle size with time, point to the attachment of monomeric species or small cluster as the rate determining step and not the diffusion of both nutrients to the crystal nucleus. Similar conclusions were already drawn by *in situ* EDXRD

 This journal is © The Royal Society of Chemistry 2020

Open Access Article. Published on 20 August 2020. Downloaded on 2/16/2026 6:59:12 AM.
This article is licensed under a Creative Commons Attribution 3.0 Unported Licence.

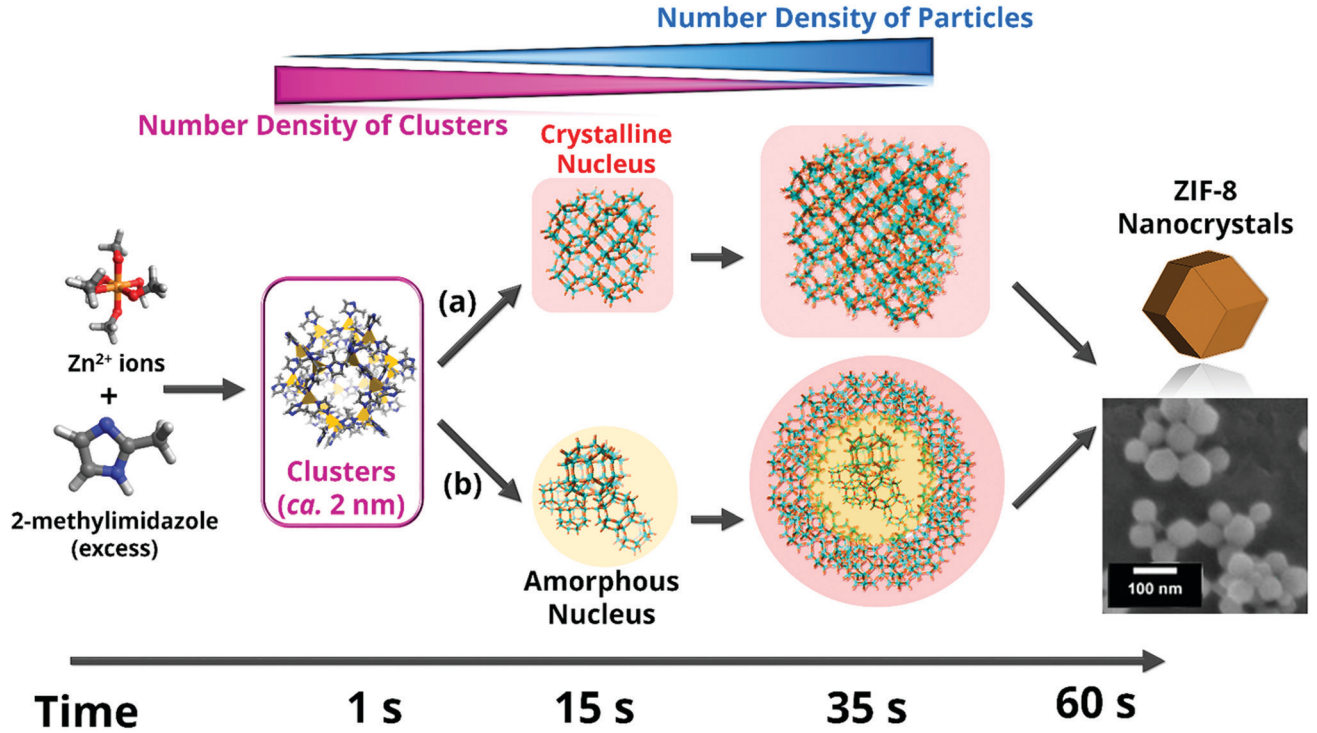

Fig. 5 Different species formed during ZIF-8 nucleation and growth. Results point to the initial formation of very small clusters prior to the ZIF-8 nanoparticle formation, as well as to a continuous slow nucleation, which takes place simultaneously to the fast crystal growth over a period of time. Crystallinity of the first nuclei cannot be assessed given the lower sensitive of wide-angle X-ray scattering compared to small-angle X-ray scattering. Thus, two possible alternative crystallization pathways (a) and (b) are considered. Reprinted with permission from ref. 157. Copyright©2011 John Wiley & Sons, Inc.

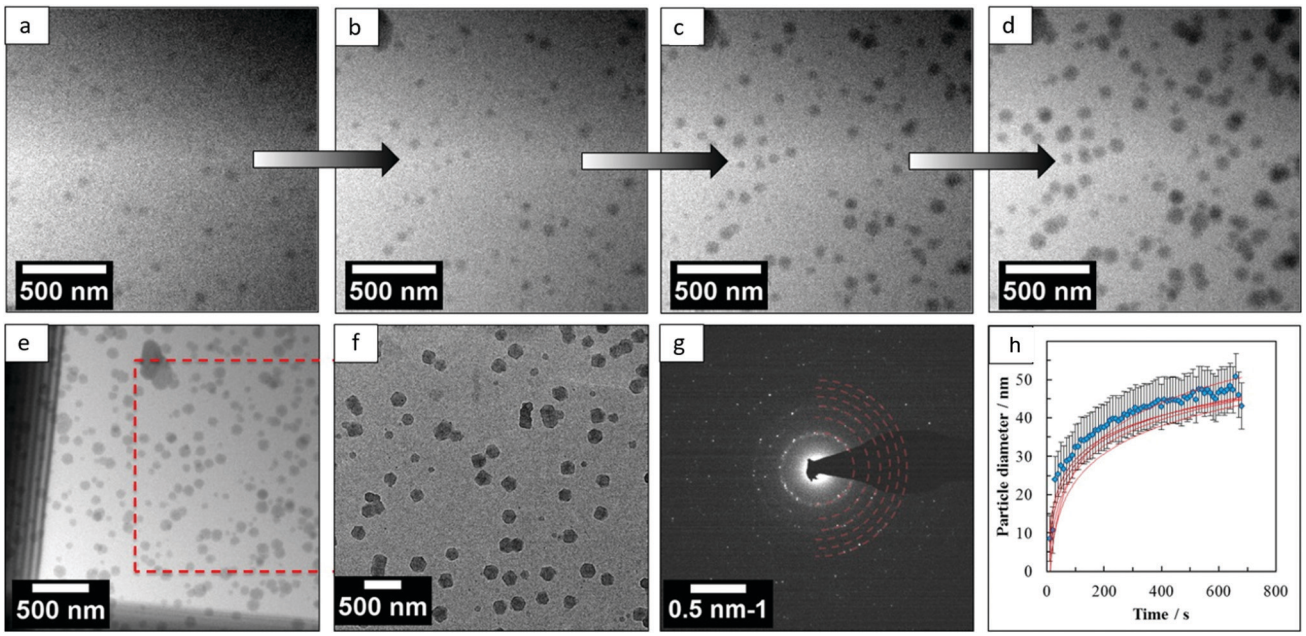

Fig. 6 (a–d) Micrographs acquired by liquid cell TEM at different synthesis times during the real-time monitoring of ZIF-8 formation, (e) image acquired after ZIF-8 growth, (f) micrograph of the same area after the cell was dried, (g) diffraction pattern obtained from the particles grown in the cell after drying and (h) mean growth kinetics of individual particles. Reprinted with permission from ref. 156. Copyright©2015 American Chemical Society.

studies,[148] in which the calculated Avrami exponent n was close to 1, indicating the crystallization process is rate-limited by surface reaction. The similar results obtained by spectroscopic techniques and this LCTEM study proved the suitability of this

Open Access Article. Published on 20 August 2020. Downloaded on 2/16/2026 6:59:12 AM.
This article is licensed under a Creative Commons Attribution 3.0 Unported Licence.

technique for the direct observation of MOF synthesis, the electron beam having a negligible effect on the particle assembly and growth under the studied conditions.

At the molecular level, *in situ* atomic force microscopy (AFM) has been applied by Attfield *et al.*[158] to study the surface crystal growth of ZIF-8 from essentially methanolic solutions. Fig. 7a shows the *in situ* AFM deflection images acquired for the (110) face of ZIF-8, which demonstrate that crystal growth takes place by both, spiral growth and "birth and spread" mechanisms simultaneously.[158–160] Moreover, from cross-sectional analysis it was observed that most of the stable growth steps have heights of 1.2 ± 0.1 nm, indicating a strongly preferred surface termination. Even more interestingly, the real-time monitoring of a growing 2D surface nucleus (Fig. 19c) allowed for the identification of different metastable sub-steps with heights of 0.4, 0.6, 0.8, 0.9, 1.1 and 1.2 nm after 0, 2.9, 4.9, 12.8, 15.6 and 40 min, respectively.

The authors related these metastable substeps to the ZIF-8 crystal structure (Fig. 7b) obtaining further insight into the growth process. Specifically, the results point to crystal growth by addition of monomeric $MeIm^-$ and Zn^{2+} ion species, and not larger clusters or SBUs, until stable growth steps of 1.2 nm were formed. Similar AFM studies (both *ex situ* and *in situ*) have also been performed for other intensively studied MOFs, such as HKUST-1[161–163] and MOF-5,[164–166] proving the applicability of AFM to different MOF systems as well as its potential to study MOF crystal growth.

2.2.2 Generation of binding sites in ZIF-8: diffusion of guests and interactions with the pore surfaces. One key feature for gas sorption and catalysis is the mass transport limitations imposed by the pore system of the MOF. Thus, as in the case of MIL-100, understanding where the gas molecules (or reactants) are preferentially adsorbed on the MOFs' pores with fully coordinated metal sites that show high working capacities or activity has been the target of much research. For an extensive overview on different experimental methods to unveil host–guest interactions in MOFs, we strongly recommend the very recent review by Easun *et al.*[167] Here, we highlight some recent

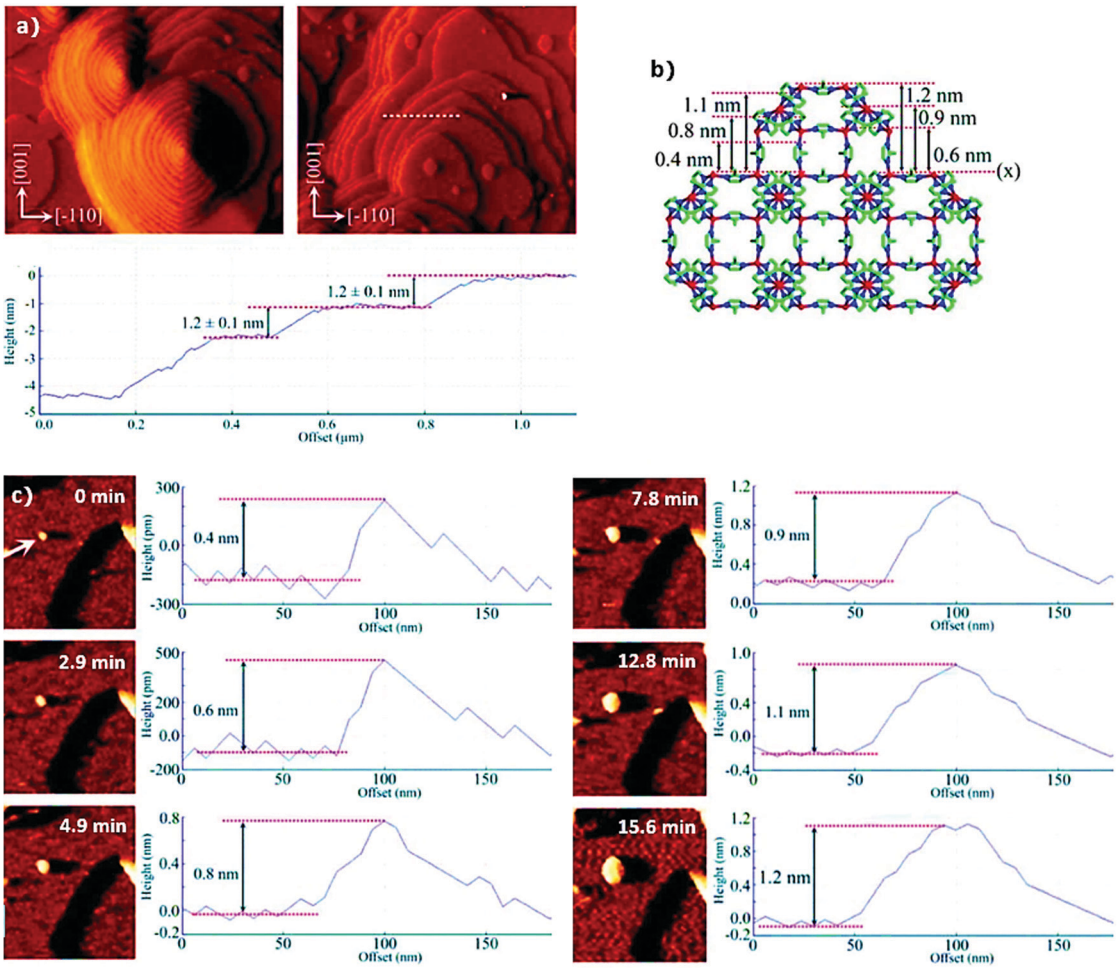

Fig. 7 (a) *In situ* atomic force microscopy deflection images of the (110) face of ZIF-8 showing growth steps formed by spiral growth mechanism (left) and "birth and spread" mechanism (right) together with the cross-sectional analysis of some growth steps (dashed white line) revealing the step heights corresponding to the d_{110} crystal spacing of the material, (b) ZIF-8 structure viewed along the [100] direction and (c) real time AFM deflection images and cross-sectional analyses of developing growth step at 0, 2.9, 4.9, 7.8, 12.8 and 15.6 min after first observation of the MOF nucleus (highlighted with the white arrow). Reprinted with permission from ref. 158. Copyright©2011 American Chemical Society.

Open Access Article. Published on 20 August 2020. Downloaded on 2/16/2026 6:59:12 AM.
This article is licensed under a Creative Commons Attribution 3.0 Unported Licence.

examples of diffraction and spectroscopic studies on ZIF-8, providing a brief overview of some of the most used techniques.

Neutron and X-ray diffraction can provide very valuable information regarding the location of the guests, yielding insight into the MOF preferential adsorption sites, one of the most important features when considering the interaction between guest molecules and MOFs.[167] A recent, ground-breaking study by Hobday *et al.*[168] showed that the arrangement of gases, such as CH_4, O_2, N_2 or Ar, at very high pressures (up to 1.5–3 GPa) and their interactions with ZIF-8 can be studied by high-pressure crystallography combined with DFT and Grand-Canonical Monte-Carlo (GCMC) calculations. The interest of this study lies in the possibility of studying changes in the framework both from the structural and the energetic point of view. Nonetheless, in the case of molecules containing light elements, such as H, neutron diffraction is especially attractive and well-established in the community. The reason is the generally large neutron scattering cross-scattering of light elements, in contrast to the X-ray scattering cross-section which increases as a function of Z^2 (where Z is the atomic number).

Many examples can be found in the field of MOFs where the adsorption of different guest molecules, such as CO_2, CH_4, H_2 or NH_3 have been studied by neutron powder diffraction (NPD).[169–174] Newly developed techniques based on dielectric constant values have been recently used to study the interaction of sorbates with the framework.[175] However, NPD has been the technique of choice for studying the location of gas molecules. In the particular case of ZIF-8, Wu *et al.*[176] performed NPD studies for D_2-loaded ZIF-8 and observed that the primary adsorption site for D_2 was on top of the imidazolate moieties, specifically close to the C═C bond (Fig. 8). Likewise, a later work by the same authors point to a similar behaviour for CD_4, which was preferentially adsorbed on top of the linker with one D atom oriented towards the C═C double bond.[177] These results are in contrast with those commonly encountered for other MOFs, for which a preferentially adsorption on the metal nodes has often been reported. The preferential adsorption close to the organic linker further guides the possible optimization of ZIF-8 as sorbents for gas storage, where the modification of the imidazolate moieties rather than the metal sites might lead to an improved sorbent performance.

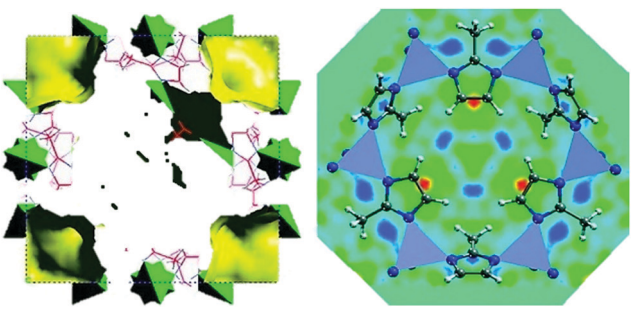

Fig. 8 Left: (001) view of the refined crystal structure of ZIF-8 from neutron powder diffraction together with the available free space for H_2 occupation. Right: (111) view of the real-space Fourier-difference scattering-length density superimposed with six-ring pore aperture of ZIF-8, indicating the location of the most favourable adsorption sites (red-yellow regions). Reprinted with permission of ref. 176. Copyright © American Chemical Society 2007.

Interestingly, next to the location of preferential D_2 and CD_4 adsorption sites, Wu *et al.* observed a CD_4-induced fully reversible ZIF-8 structural transition at 60 K triggered by the rearrangement of CD_4 molecules at high adsorbate loadings. All in all, these works by Wu *et al.*[170,176] illustrate the wealth of information that can be obtained by NPD, especially well-suited for hydrogen and other light elements. Monitoring the changes taking place in the atomic and molecular motions upon adsorption provides crucial insight into the nature and strength of the framework–guest interactions as well. Several spectroscopic techniques, such as infrared spectroscopy, have therefore been used to this end. Easun *et al.*[167] recently highlighted in their review the suitability of inelastic neutron scattering (INS) to perform such a type of studies. INS provides valuable information about molecular and atomic motion modes, especially for light elements (*vide supra*). In the case of ZIF-8, however INS has been used to study the linker rotation upon N_2 adsorption, rather than gaining insights into the adsorption sites.[178] In particular, the free rotation of the methyl groups of the 2-methylimidazolate linker of ZIF-8 was observed to be hindered upon N_2 adsorption. This was attributed to a change in the chemical environment of methyl groups upon swinging of the linkers, leading to a larger steric hindrance of their rotation. Furthermore, besides the location of the preferential adsorption sites and the determination of the nature and strength of the host–guest interactions, the diffusion rate should also be borne in mind when considering different applications of porous materials. Indeed, in many cases the performance of nanoporous compounds is controlled by their transport properties, playing a critical role when considering them as, for instance, catalysts or adsorbents. Hence, different techniques, a summary of which can be found in a review by Kärger *et al.*,[179,180] have been used to study guest diffusivities as well as possible molecular transport resistances in porous materials. Among them, in this review we highlight quasi-elastic neutron scattering (QENS),[181–198] pulsed field gradient (PFG)-NMR[179,199–207] as well as interference[208] and IR microscopy.[179,208–221]

QENS allows to determine the diffusion of guest molecules under equilibrium conditions on a timescale for which the guest molecules remain inside the MOF crystals, providing the intracrystalline self- and/or transport diffusivities[190,222] for the incoherent and coherent neutron scattering signals, respectively. Pantatosaki *et al.*[191] performed QENS experiments to calculate the self-diffusivity of H_2 adsorbed on deuterated ZIF-8. The authors compared the experimentally obtained H_2 self-diffusivities with those calculated with molecular dynamics computer simulations and observed a reasonable agreement between the experimental and simulation studies for ZIF-8, being the calculated self-diffusivity values very sensitive to the framework dynamics. In another study, Jobic *et al.*[192] further studied the self-diffusion of CH_4 by QENS in the same MOF, *i.e.* ZIF-8, and compared their results with those previously reported for different experimental techniques, namely PFG

Open Access Article. Published on 20 August 2020. Downloaded on 2/16/2026 6:59:12 AM.
This article is licensed under a Creative Commons Attribution 3.0 Unported Licence.

NMR[203,206] and IR microscopy,[206,211] and computational methods.[223–225] Interestingly, the self-diffusivities obtained from QENS by Jobic *et al.*[192] are in agreement, especially at low CH_4 loadings, with those previously determined by PFG NMR and with the corrected diffusivities from IR microscopy. This contrasts with what has been often reported for other traditional porous materials, for which differences in the diffusivities measured with different techniques have often been encountered. These differences have been commonly attributed to the different diffusion lengths probed by the different experimental techniques together with the presence of structural defects. In this way, for example, the diffusivity values measured by QENS, for which the diffusion path covered is typically of tens of nanometres, are less affected by the possible presence of defects than in the case of PFG NMR, whose effective length scale is of several micrometres. The results reported by Jobic *et al.*[192] point therefore to the presence of only few defects in the crystalline framework and/or to their negligible influence on CH_4 diffusion. QENS and NMR have been combined in a series of recent studies in benzene motion within UiO-66(Zr) as well.[226] Furthermore, a unique advantage of QENS compared to PFG NMR and interference and IR microscopy is that it also provides information of the geometry of the diffusional process by analysing the elastic component of the incoherent scattering function with different proposed models. In the particular case of the work reported by Jobic *et al.*,[192] the spectra obtained suggest a restricted mobility of CH_4 through the ZIF-8 hexagonal windows, with shorter residence times within the sodalite cages than the characteristic time for intercage hopping. Thus, despite the framework flexibility, which leads to an enlargement of the pore aperture allowing for the adsorption of CH_4, the CH_4 mobility is still restricted at the pore windows, being the CH_4 diffusion in ZIF-8 smaller than those commonly reported for other porous materials. This ability of QENS to provide understanding into the diffusion mechanism and rate has been further exploited to shed light into the proton conductivity mechanism and proton diffusion coefficients. This is the case of the works recently reported by Pili *et al.*[227] and Damasceno Borges *et al.*[228] who used XRD together with QENS and molecular dynamics simulations to shed light into proton conduction on MOF.

PFG NMR provides the self-diffusivity of guest molecules adsorbed on porous materials, *i.e.* under equilibrium conditions, as it is the case for the incoherent contribution in QENS experiments. For PFG NMR, however, the measurement time scale allows for different diffusion path scenarios (within and outside the crystals, see review by Chmelik *et al.*),[179] and only for sufficient large crystals, together with short observation times and low diffusivities, intracrystalline self-diffusivities can be obtained. PFG NMR has been used to determine the intracrystalline self-diffusivities of different guest molecules in several well-known MOFs,[199,201,202,205,229] and in the particular case of ZIF-8, self-diffusivities of different hydrocarbons,[204] small alcohols,[200] CO_2[207] and CH_4[203,206] have been reported. A recent study combining XRD, Raman, FT-IR and diffuse reflectance UV-vis spectroscopies revealed that SH_2 partially modified ZIF-8, although they were unable to describe the exact effect on the pores and surface.[230] Very recently, Dutta *et al.* showed by means of PFG NMR that SH_2 creates surface defects, but does not affect transport properties within the pores.[231] This is in line with previous studies describing surface defects that do not alter significantly ZIF-8's internal structure.[232–234] Moreover, PFG NMR, being nucleus specific, has the potential to simultaneously determine different self-diffusivities. In this sense, Chmelik *et al.*[204] studied the diffusion of 1 : 1 ethane and ethane mixtures in ZIF-8 by ^{1}H PFG MAS NMR, obtaining a diffusion selectivity towards ethene of *ca.* 6 at 283 K for ZIF-8 loaded with 4 or 8 molecules per cavity. Diffusion of the same mixture but including methane, and at a $T = 273$ K, was recently studied by a different group,[235] showing again 6 molecules per cavity and a ethene:ethane diffusion selectivity of 5.8. This also proves the reliability and reproducibility of PFG NMR as a tool for studying gas diffusion within MOFs.

Finally, besides QENS and PFG-NMR, interference and IR microscopy have also been applied in the field of MOFs to study the mobility of adsorbed molecules. A recent study used time-resolved FT-IR spectroscopy upon dosing aromatic hydrocarbons *i.e.* benzene, toluene and xylene (BTX), in other frameworks to calculate Fick diffusion coefficients, although little information on pore location was obtained.[236] For a comprehensive overview on the application of interference microscopy and IR micro-imaging to study the molecular diffusion on porous materials we refer the reader to the reviews by Kärger *et al.*[179,216] In short, these techniques provide the transport diffusivity (*i.e.* under non-equilibrium conditions) calculated from the monitored evolution of the concentration profiles within the crystals, as well as the sticking probability[219] and the surface permeability,[208,210,218,220,221,237] the latter being inaccessible by the aforementioned experimental techniques (*i.e.* QENS and PFG NMR).[216–218,220] While interference microscopy possesses a better spatial resolution, IR microscopy allows for the simultaneous monitoring of different species, being suitable for the study of individual transport diffusivities in multicomponent mixtures. Furthermore, this ability to track different species allows for the simultaneous study of labelled molecules (isotopes) and their respective self-diffusivity coefficients. Thus, IR microscopy provides both the transport diffusivity and the self-diffusivity depending on the conditions (non-equilibrium and equilibrium, respectively) under which the experiment is performed.[215,218]

2.3 Chemistry and characterization of HKUST-1 or Cu_2BTC_3

The topology known as HKUST-1 (Hong-Kong University of Science and Technology-1)[238] or MOF-199[239] has been one of the most studied MOF structures in the past 20 years. HKUST-1 is constructed of well-defined paddle-wheel secondary building units (SBU), which exhibit CUS for sorption and catalysis upon solvent removal. The framework contains four carboxylate-terminated linkers connected to dinuclear cationic clusters (Fig. 9) with either counter anions (X^- or NO_3^-) or solvent molecules (H_2O) on the axial position. The crystallographic structure relies on the ***tbo*** topology in space group $Fm\bar{3}m$.

 This journal is © The Royal Society of Chemistry 2020

Open Access Article. Published on 20 August 2020. Downloaded on 2/16/2026 6:59:12 AM.
This article is licensed under a Creative Commons Attribution 3.0 Unported Licence.

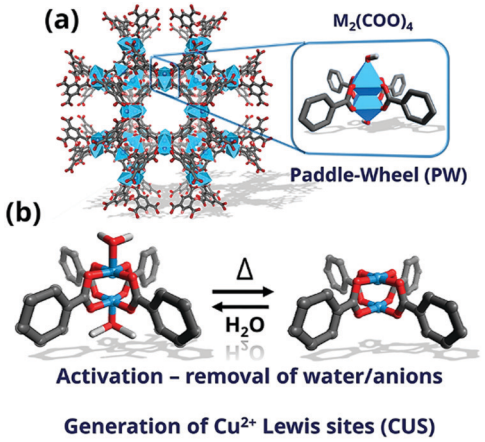

Fig. 9 (a) Square-shaped pores of 0.9 nm × 0.9 nm dimensions of HKUST-1 formed viewed along the [100] axis; inset, highlight of the paddle-wheel unit (PW) with the metal atoms coordinated in octahedral geometry and; (b) scheme of the formation of coordinatively unsaturated sites (CUS) by desolvation by release of solvent molecules (C, grey; O, red; blue, metal).

Other properties that promoted the study of HKUST-1 are their relative robustness (stable in air for several days or weeks)[240] and the myriad of metals that can be introduced into the HKUST-1 nodes, including Zn,[241] Mo,[242] Ru,[243] Ni,[244] Cr[245] or Fe.[246] In addition, mixed oxidation states[247] and radicals[248] have been observed under specific conditions, rendering this MOF very interesting for applications involving redox chemistry. Recently, several groups have reported the on-purpose introduction of defective, non-coordinating linkers into the HKUST-1 structure.[249] The metal sites exhibiting increased undercoordination show increased Lewis acidity,[250] enhancing their potential for adsorptive and catalytic applications. As described below, spectroscopic tools have proven crucial for unravelling the physicochemical properties of these material and their potential applications.

2.3.1 Generation of coordinatively unsaturated sites upon MOF activation in HKUST-1: selective binding. The CUS of HKUST-1 prompted the use of advanced techniques to study desolvation and gas sorption. Interestingly, Peterson *et al.* first reported neutron diffraction measurements on D_2-loaded Cu_3BTC_2 which suggest that adsorbate molecules are bound to metal sites.[169] However, to add more chemical information, a wide range of complementary characterization tools such as XRD, EPR, XAS, UV-vis-NIR, Raman and FT-IR spectroscopy with probe molecules (*e.g.* with CO, CO_2, NO and H_2), have aided in understanding the framework metal–adsorbate interaction. Excellent reviews on this topic are available.[16,17,19,251–254] Other gas molecules, including energy carriers[255] such as H_2 or industrially relevant O_2[256] and SH_2,[230] in combination with spectroscopic/scattering tools have been used to study the adsorptive properties of HKUST-1 and their Cr/Zn/Ru analogues at various temperatures (Table 3). A notable example of the multi-spectroscopic investigation of adsorptive properties of Cu^{2+} sites in HKUST-1 is the sorption of gas phase, dry and wet ammonia. Particularly, understanding their molecular adsorption mechanisms has proven crucial to predict the effect on distortion and/or degradation of the paddlewheel SBU and long-range order of the HKUST-1 framework. In a thorough study, Borfecchia *et al.* showed by XRD that phase changes are induced in the HKUST-1 framework only when NH_3 (1 : 1 mol Cu : NH_3, room temperature) is adsorbed after water sorption on Cu sites.[257] In the case of dry ammonia, however, the crystallinity is preserved, allowing the introduction of water even after evacuation of NH_3 without amorphization or phase change. This suggests an important role of water in the degradation mechanism of the framework. DR UV-vis spectra of the dry samples (Fig. 10) with and without NH_3 adsorbed showed a slight red shift of the Cu^{2+} d–d transition peak from 585 nm (activated) to 745 nm (+NH_3), which is similar to the peak of the hydrated sample at 725 nm, as expected for these two σ-donors (H_2O and NH_3). Far-IR spectroscopy (Fig. 10) showed that dehydration blue-shifted all the bands corresponding to Cu–O and Cu–Cu, due to the increased donation of the carboxylate ligands. Introduction of NH_3 restored the IR spectrum to that of the hydrated one. These spectral features indicate that NH_3 is bonded to the open Cu^{2+} sites *via* the lone pair in a similar fashion to H_2O molecules, thus, decreasing the Cu–O bond strength with the carboxylates due to increased electron density around the Cu centre. This was further corroborated by XANES which indicates an effective interaction of Cu centres with NH_3 molecules derived from two pre-edge features that change when a 50 mbar equilibrium pressure of NH_3 is introduced. Surprisingly, EXAFS fitting indicated a Cu–O carboxylate bond stretch of 0.025 Å and 0.065 Å for water and ammonia, respectively, compared to activated HKUST-1. This difference likely originates from a higher Lewis basicity of ammonia (pK_a = 9.24) compared to water, decreasing the Cu–O bond strength as well as a degradation-free framework (XRD). It was thus possible to obtain a chemical and electronic description of the metal centres and the framework by this array of techniques (Fig. 10c). In general, no structural changes are observed upon adsorption and desorption of NH_3 under dry conditions, while only hydrated HKUST-1 degrades upon NH_3 dosing. Such structural disintegration of the MOF framework is likely initiated by metal-linker defect formation. In the case of HKUST-1, degradation is suggested to initiate by Cu–O carboxylate bond scission, which might result in Cu^{2+} to Cu^{+} reduction. In contrast to the work by Borfecchia *et al.* where no Cu^{2+} reduction was observed, Nijem *et al.*[258] estimated that *ca.* 3.5 at% of the total Cu is Cu^{+} (which increased to *ca.* 10 at% with higher H_2O pressure), being the reduction attributed to missing-linker defects. In their report, the degradation mechanism was investigated in more detail by studying a HKUST-1 thin-film by ambient pressure XPS and XANES under dry and humid NH_3 adsorption conditions.

It is worth mentioning, different spots of the sample were measured to avoid beam-induced reduction of the sample. They observed the presence of the L_3 Cu^{+} peak at *ca.* 935.3 eV in the XANES spectra (see Fig. 11a), indicating Cu^{+} in the material. Besides the mixed Cu oxidation states, experiments revealed a complex interplay between water and ammonia molecules in their coordination to Cu^{2+} clusters. Introduction of 0.26 Torr H_2O to open Cu^{2+} sites results in a shoulder in the AP-XPS O 1s

Open Access Article. Published on 20 August 2020. Downloaded on 2/16/2026 6:59:12 AM.
This article is licensed under a Creative Commons Attribution 3.0 Unported Licence.

Table 3 Summary of the different spectroscopic/scattering tools used for the study of HKUST-1–gas interactions

Metal cation	Spectroscopic tools used for the study of: Crystal lattice	Metal sites	Linker/gas molecules	Conditions (T and gas)	Ref.
Cu	XRD	EXAFS, XANES, UV-vis-NIR	Raman, IR	Thermal activation (CO and H_2 probed IR at 77 K)	254
	XRD, Raman, UV-vis-NIR, NMR	Raman	Raman	Chemical activation	259
	—	—	INS	CD_4 (at 77 K)	172
		—	INS	CO_2 (at 20 K)	260
	ND	—	INS	H_2 (at 4–5 K)	189 and 261
	ND	—	—	D_2 (at 4–5 K)	169
	—	Low-temperature TDS	—	H_2/D_2	262
	μ-XRF, synchrotron-based XRD, PDF	PDF	IR	I_2 and H_2O (at 348 K)	263
	—	*In situ* IR	*In situ* IR	CO, CO_2, NO, N_2, H_2 (20–77 K)	264
	XRD	XANES, UV-vis-NIR	IR	SH_2 (298 K)	230
	—	XPS, NEXAFS	—	H_2O, NO (at 298 K)	265
	XRD	XANES, EXAFS, UV-vis-NIR	cw EPR, HYSCORE EPR, IR	H_2O, NH_3 (298 K)	257
	—	Synchrotron XPS, NEXAFS, APS	—	H_2O, NH_3 (298 K)	258
	—	—	Solid-state NMR, IR	NO (298 K)	266 and 267
	—	—	ENDOR, HYSCORE, cw EPR	HD, D_2, H_2 and $^{13}CO_2/^{13}CO$	268 and 269
	—	—	Solid-state NMR	^{13}CO, CO_2 (213–353 K)	270
	XRD	—	cw EPR and DFT	Ethene, 1-butene, ethane, and butane	271 and 272
	XRD	XPS, XANES	—	C_3H_6	273
Cr	XRD, NPD	UV-vis-NIR, XANES	*In situ* IR	Thermal activation and O_2 sorption (variable temperature)	256
	NPD	—	INS, *in situ* IR	H_2, D_2 (30–80 K)	194
Ru	XRD	XPS	$C^{16}O/C^{18}O$-probed FT-IR	Activation	274
	XRD	DRIFTS, XPS	DRIFTS	Activation and H_2 (forms carbonyls and hydrides)	275
	XRD	UV/vis-, XPS	NMR, IR, Raman	—	276

Inelastic neutron scattering (INS), neutron diffraction (ND), thermal desorption spectroscopy (TDS), micro X-ray fluorescence (μ-XRF), pair distribution function (PDF), continuous wave electron paramagnetic resonance (cw-EPR), hyperfine sub-level correlation (HYSCORE), X-ray photoelectron spectroscopy (XPS), near-edge X-ray absorption fine structure (NEXAFS), ambient photoelectron spectroscopy (APS), neutron powder diffraction (NPD).

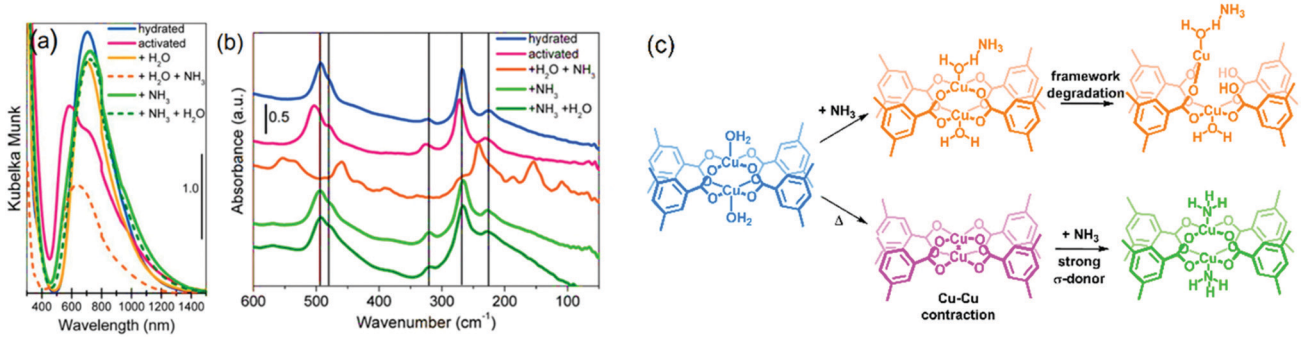

Fig. 10 Spectroscopic analysis of HKUST-1 in hydrated and activated form, as well as upon introduction of ammonia of the hydrated and activated states. (a) Diffuse reflectance UV-vis spectroscopy and (b) far-IR spectroscopy under different conditions. (c) Different states of the Cu paddlewheel units under the different conditions reported. Adapted and modified from ref. 257. Copyright©American Chemical Society 2012.

signal at 533.7 eV, indicating adsorbed $Cu^{2+}\cdots OH_2$. Adding 0.03 Torr NH_3 induces a shift of +0.6 eV, which is related to the formation of $[O_2H\cdots H_3N\cdots Cu^{2+}]$. Therefore, NH_3 replaces H_2O at the Cu^{2+} centre due to its higher basicity.

However, hydrogen bonding between water and ammonia strengthens metal–ammonia interactions due to cooperativity, resulting in a reduction of the metal oxidation state. Such Cu^{2+} reduction facilitates linker replacement by gas-phase (NH_3–H_2O) species, explaining the origin of structural degradation. The shoulder around 401.8 eV in the AP-XPS N 1s signal further corroborated the existence of such cooperative interactions, as described in the model in the inset of Fig. 10c.

 This journal is © The Royal Society of Chemistry 2020

Open Access Article. Published on 20 August 2020. Downloaded on 2/16/2026 6:59:12 AM.
This article is licensed under a Creative Commons Attribution 3.0 Unported Licence.

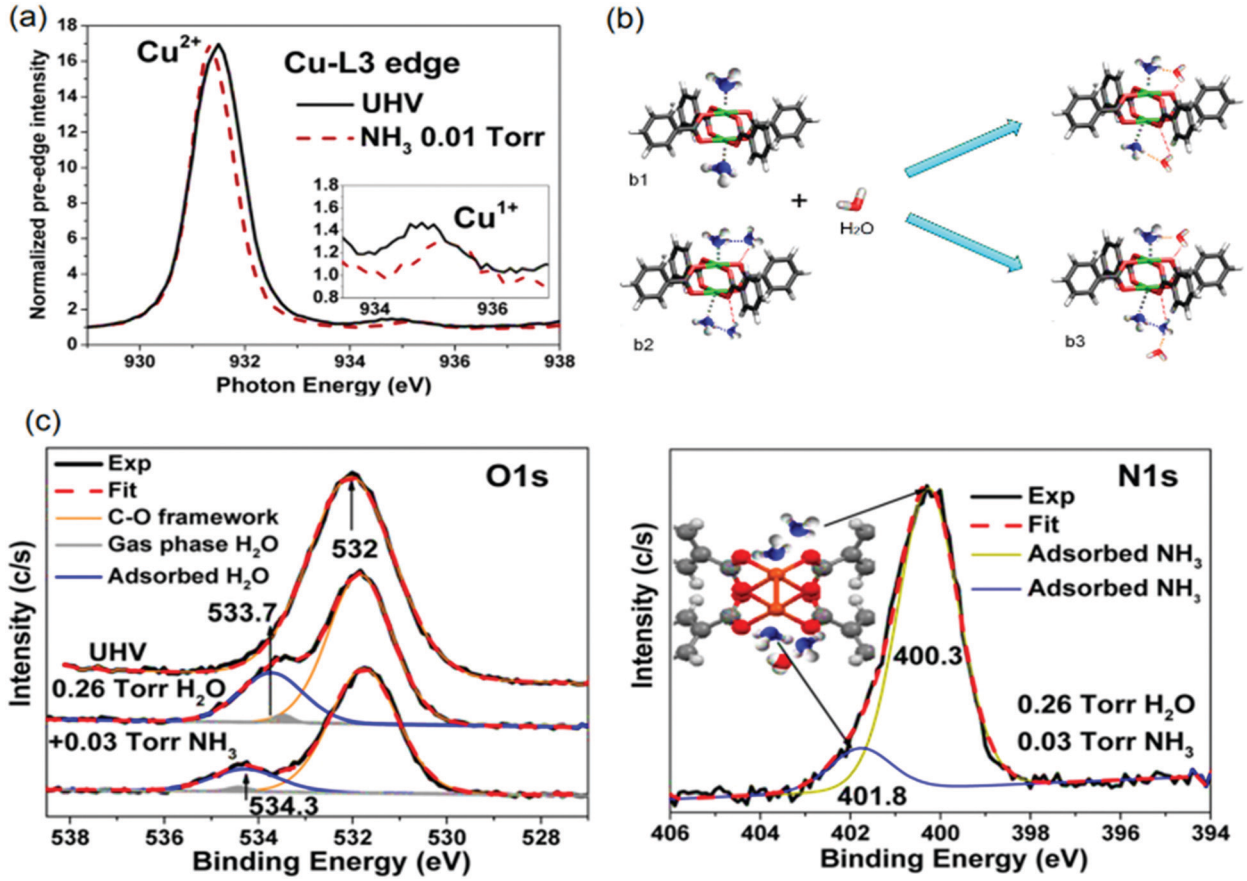

Fig. 11 (a) X-ray absorption bands at the L_3 Cu^{2+} edge (inset shows L_3 Cu^{+}) of the HKUST-1 film without and with 0.01 Torr of NH_3 adsorbed. (b) Possible cooperative interactions between adsorbed water and ammonia molecules (C, grey; O, red; H, white; N, blue; and Cu, green). (c) O 1s and N 1s ambient pressure XPS peaks of the humid NH_3 sorption experiments of HKUST-1 film. Adapted and reprinted from ref. 258. Copyright©American Chemical Society 2015.

The structural configuration of $[O_2H\cdots H_3N(\cdots H_3N)\cdots Cu^{2+}]$ species (Fig. 11b3) involved in the degradation mechanism are displayed in Fig. 11b, established by H_2O addition to NH_3-preadsorbed paddlewheels at NH_3 : Cu 1 : 1 (Fig. 11b1) and 2 : 1 (Fig. 11b2) ratios. These *in situ* studies, and the characterization palette explored therein, showcase how complementary spectroscopic tools can reveal detailed molecular insight in metal–host interactions. Also, the influence of experimental conditions, such as pressure, the nature of gas phase species, to even the order of gas phase exposure, can be interrogated under *in situ* conditions.

2.3.2 Generation of coordinatively unsaturated sites upon MOF activation in HKUST-1: mixed oxidation states and redox-active paddlewheels. The desolvation process affects the metal centre in two ways: (i) the geometry and symmetry changes and (ii) the partial positive charge (δ^+). This prompted the study of the redox properties of M_3BTC_2. For example, Xie *et al.* used Mössbauer spectroscopy to determine the Fe oxidation states in the node of HKUST-1(Fe), *i.e.* $[Fe_2(H_2O)_2(BTC)_{4/3}]Cl{\cdot}4.5(DMF)$.[246] The Mössbauer spectrum consisted of two quadrupole-split doublets: one with a double isomer shift of δ = 0.41 mm s^{-1} and quadrupole-splitting value ΔE = 0.78 mm s^{-1}; and one with a double isomer shift of δ = 1.08 mm s^{-1} and quadrupole-splitting value ΔE = 1.66 mm s^{-1}, corresponding to Fe^{2+} and Fe^{3+} species, respectively.

In addition, the integral under the curves yielded a 49 : 51 ratio, indicating 1 : 1 ratio of each oxidation state. Based on these results, we expect possible fascinating chemistry to unveil for Fe-containing paddlewheels in MOFs. By careful design, Fe–Fe distances and coordination environments can be similar to those in enzymes, as shown for other topologies.[277] More effort are being made to develop Fe containing HKUST-1 materials, mainly using the mentioned Mössbauer,[278] as well as XAS and XRD tools for the purpose of studying these metal sites.[279] Ru^{3+}/Ru^{2+} mixed-valence states have been also observed in the HKUST-1(Ru) analogue, reported by Fischer *et al.* by XPS (Fig. 12a).[243] Two different Ru species were identified in the mentioned study: Ru^{3+} and Ru^{2+}, as confirmed by XANES analysis of both the precursors and the obtained materials.[280] Similar materials were further investigated by CO-probe molecule FT-IR spectroscopy and the experimental data compared to DFT calculations.[274]

CO-probe FT-IR spectroscopy points to both Ru^{2+} and Ru^{3+} oxidation states since two features are observed both for labelled $C^{16}O$ (2171 and 2137 cm^{-1}) and $C^{18}O$ (2120 and 2085 cm^{-1}). However, DFT calculations cleared out that the presence of Cl^- anions can lead to more complex scenarios in the interpretation of IR spectroscopy, for example, formation of chloroformyl and

Open Access Article. Published on 20 August 2020. Downloaded on 2/16/2026 6:59:12 AM.
This article is licensed under a Creative Commons Attribution 3.0 Unported Licence.

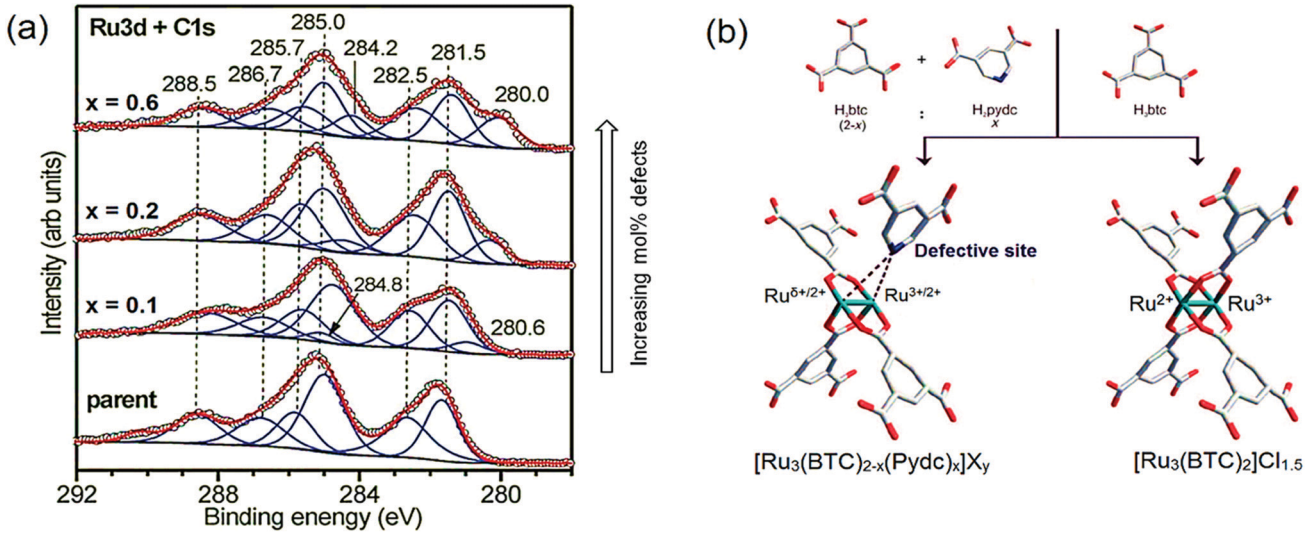

Fig. 12 (a) X-ray photoelectron spectra of defect-engineered Ru_3BTC_2 with increasing defect molar content (*x* indicates the targeted fraction of Pydc, where Pydc = 3,5-pyrdinedicarboxylate) showing the peaks of $Ru^{\delta+}$ at 280.0 and 284.2 eV, Ru^{2+} at 281.5 and 285.7 eV and Ru^{3+} at 282.5 and 286.7 eV. (b) Model of parent and defective clusters including mixed-valence $Ru^{3+/2+/\delta+}$ species. Adapted and reprinted with permission from ref. 247 and 404. Copyright©2014, John Wiley & Sons, Inc.

CO–Cl species, rather than purely CO on mixed-valence nodes. Partially reduced Ru paddlewheels were also observed in linker defect-engineered HKUST-1(Ru) prepared by Baiker's mixed-linker method (Fig. 12b).[247,280,281] XPS of HKUST-1(Ru) with increasing amounts of low-coordinating defect linker Pydc (3,5-pyridinedicarboxylic acid) show an emerging peak doublet at 280.0 and 284.2 eV. These peaks are characteristic for the formation of $Ru^{\delta+}$ besides Ru^{2+} (281.5 and 285.7 eV) and Ru^{3+} (282.5 and 286.7 eV). This peak appearance is accompanied by a decrease in the intensity of the Cl 2p peak (not shown), reinforcing their hypothesis given the proposed structural formulas in Fig. 12b. This report shows that, even in clusters containing metals with multiple oxidation states, the introduction of defect ligands can further reduce the oxidation state of the metal cations in the paddlewheel. Similar to Ru, partially reduced Cu^+/Cu^{2+} has been observed in defective HKUST-1 by XPS and CO-probed FTIR.[249] But in the last case, ambiguities exist on the cause of Cu^{2+} reduction being thermal activation or the inherent presence of cluster defects. A broader discussion has been established during the past years on the exact nature of Cu^+ species in HKUST-1 in general, *i.e.* not only considering defective HKUST-1. Two possibilities are proposed: Cu^+ originates from (1) extra-framework cations leading to Cu_2O impurities from synthesis, (2) mixed valence Cu^+/Cu^{2+} dimeric paddlewheels originating from (2a) defective clusters, or (2b) reversibly reducible/oxidizable Cu^{2+} atoms in perfectly coordinated paddlewheels. The presence of Cu^+ was first reported by de Vos *et al.*[282] by assigning the IR band at 2123 cm^{-1} to Cu^+–CO, situated *ca.* 50 cm^{-1} below the typical Cu^{2+}–CO band of low CO coverage at 2179 cm^{-1}. Quantification of the Cu^+/Cu^{2+} ratio was not possible, since the extinction coefficients for Cu^+–CO is much higher compared to Cu^{2+}–CO due to enhanced $Cu^+(\sigma) \rightarrow C{\equiv}O(\pi^*)$ back-bonding. Cu^+ was presumed to originate from Cu_2O agglomerates invisible to electron microscopy and/or CO-induced Cu^{2+} reduction into Cu^+.

In a later study, Bordiga *et al.* observed similar CO-probed IR spectra, but rejected the CO-induced $Cu^{2+} \rightarrow Cu^+$ reduction mechanism proposed by de Vos *et al.* Instead, they ascribe the 2127 cm^{-1} band to minor fractions ($\ll$1%) of Cu_2O, possibly amorphous in nature as suggested by broadness of the Cu^+–CO peak and its absence in XRD.[264] This Cu_2O phase is proposed to form during activation/heating, resulting in the desorption of solvent molecules (*i.e.* the aim of the treatment) which is accompanied by Cu^{2+} reduction into Cu^+, as in Cu-exchanged zeolites. Wöll and co-workers[283] later stated that they can rule out the hypothesis proposed by Bordiga *et al.* since their Cu_3BTC_2 film, grown at room temperature, is not heated yet it still showed the Cu_2O peak of the $2p_{3/2}$ line in XPS (Fig. 13a) experiments and the band corresponding to Cu^+–CO (Fig. 13b) adducts was present in the IR spectrum. Therefore, Wöll *et al.* propose Cu_2O impurities are either: (i) contained in the Cu-acetate solution prior to synthesis, or (ii) formed by oxidation when exposing the MOF thin film to ambient air. Also, they confirm that the Cu_2O fraction increases to as high as *ca.* 42 at% of all the Cu in the MOF (Fig. 13c) upon heating to 420 K. In short, XPS data showed increasing amounts of Cu_2O upon heating the film. However, a fraction of Cu^+ is already present in pristine Cu_3BTC_2, due to synthesis impurities or exposure to ambient air.

The studies by de Vos,[282] Bordiga[264] and Wöll *et al.*[283] assumed the Cu^+ signal contributions in XPS and IR mainly originate from Cu_2O impurities. However, Szanyi, Daturi and co-workers[284] claimed that the Cu^+–CO band in their IR spectra cannot be attributed to Cu_2O impurities alone, given its high relative intensity compared to the Cu^{2+}–CO peak. Instead, they claimed to observe reversible redox properties of Basolite® C300 as a whole and, alternatively, the $(Cu^+/Cu^{2+})_2(BTC)_4$ paddlewheel as representative redox unit. St. Petkov *et al.*[285] confirmed the existence of mixed valence Cu^+/Cu^{2+} dimeric paddlewheels. They elegantly combine XPS, XRD and IRRAS on model HKUST-1

Open Access Article. Published on 20 August 2020. Downloaded on 2/16/2026 6:59:12 AM.
This article is licensed under a Creative Commons Attribution 3.0 Unported Licence.

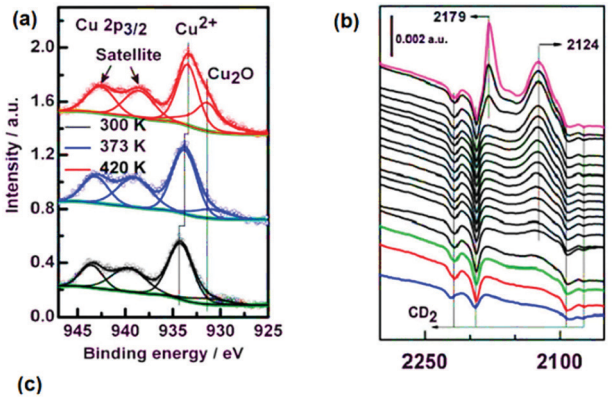

(c)

	Binding energy/eV		Intensity/a.u		Ratio
T/K	Cu^{2+}	Cu_2O	Cu^{2+}	Cu_2O	$\frac{Cu^+}{Cu^+ + Cu^{2+}}$
300	934.2	931.4	1.433	0.213	12.9%
373	933.8	931.0	1.556	0.3	16.2%
420	933.4	931.4	1.424	1.027	41.9%

Fig. 13 (a) XPS spectra of a HKUST-1/SAM thin film activated at different temperatures, (b) CO-probed FT-IR and (c) Cu^{2+}/Cu^+ ratios calculated from the XPS data. Adapted and reprinted from ref. 283. Copyright©Royal Society of Chemistry 2011.

surface mounted (SUR)MOFs with limited Cu_2O impurities and high crystallinity on the one hand and DFT calculations on the other hand. St. Petkov *et al.* prove that defective $(Cu^+/Cu^{2+})_3(BTC)_2$ units can cause the 2122 cm^{-1} CO-IR peak, the latter being observed even in model Cu_3BTC_2 SURMOFs were a relatively high concentration (*ca.* 5%) of the paddlewheels has missing linkers. Importantly, they show that the adsorption strength of CO on defective paddlewheels is much higher, showing their distinct chemical interaction and nature relative to non-defective paddlewheels.[265] The concept of defective Cu-MOF thin films has been further extended to HKUST-1-type SURMOFs[286] or paddlewheel Cu-MOFs.[287] Not only synthesis conditions, thermal treatments, but also e^- beams, X-rays and (long-term) exposure to ambient conditions can reduce Cu^{2+} to Cu^+ in HKUST-1, for example by creating Cu-linker bond scission.[288] Todaro *et al.* monitored the evolution of Cu paddlewheels over ambient exposure time by XRD, SEM, Raman and EPR.[289,290] Exposure for more than 20 days results in hydrolysis of Cu–O bonds by destructive interactions with H_2O that generate EPR-silent Cu^+ sites and a decrease in the Raman Cu–O bond peak. This has been further corroborated by XAS,[291] and surface studies combining infrared reflection absorption spectroscopy (IRRAS) and XPS.[292] This dynamic character of the $Cu^{+/2+}$ sites is still the subject of research and seems to strongly depend on many parameters.[293,294] The presence of guest molecules, solvent, thermal treatment, presence of defects, incident beam and others, have an impact on the redox properties of PWs. This also holds true for other analogues, *e.g.* Ru, and strengthens the message that this material still deserves the attention is given.[275]

In brief, there is a long history of research on the underlying causes and nature of mixed valence metal nodes in HKUST-1, and MOFs in general, for which full agreement is not yet reached. However, opportunities lie ahead for tuning the oxidation states of these metal centres by targeted treatments which tailor their chemical properties, thus, gas sorption and catalysis abilities. As exemplified in this section, *in situ* spectroscopies are valuable tools to unveil the nature of redox-active clusters and can an undoubtedly will contribute to the development of more complex materials including mixed-valence metals.

3. Characterization of metalated nodes and grafted coordination complexes

One of the predicted key advantages of MOFs is the tunability of their function by hosting adsorptive or catalytic centres on their organic backbone and metal nodes.[3] Among the different approaches reported to alter MOF properties, their post-synthetic modification is a very powerful method to tailor their functionality beyond the restrictions imposed by direct synthesis.[295,296] This approach enables the introduction of functional groups that are unstable under the conditions for *de novo* synthesis, or the modification of specific sites in the framework that are otherwise impossible to be carefully tuned.

In general, post-synthetic modification (PSM) has been developed in order to modify the structure in four different ways: (1) exchange of the metal cations from the framework, (2) introduction of organic functionalities into the organic ligand backbone, (3) metalation of the oxide-like cluster structure to yield supported single-metal atoms,[238,297] (4) reacting metal salts with the added functionalities to create coordination complexes grafted to the organic struts.[298] Given the importance of these metal sites in catalysis, gas sorption and sensing, and the outstanding examples that have been reported, a detailed analysis of the latter two approaches will be presented below. For a detailed insight on the former two, excellent literature is available on those topics.[43,44,295,299–302]

3.1 Metalation of the nodes

Some MOFs contain metal oxide nodes which exhibit OH groups after solvent removal. In 2009, Meilikhov *et al.*[303] reported the first functionalization of metal oxide nodes, by reacting the μ_2-OH bridging groups of two AlO_6 octahedra in MIL-53(Al) with silylated ferrocene derivatives using gas phase loading, as confirmed by ^{29}Si, ^{13}C and ^2H MAS NMR spectroscopy. Larabi *et al.*[304] later used a similar approach to graft $AuMe(PMe_3)$ onto the nodes of UiO-67(Zr) and performed characterization using ^{31}P, ^{13}C, ^1H MAS NMR and DRIFTS. More recently, studies reporting the introduction of metals bound to the O atoms of Zr_6 clusters either *via* Solvothermal Deposition in a MOF (SIM) or Atomic Layer Deposition In MOFs (AIM) are listed in Table 4 for different topologies (UiO-66, UiO-67, NU-1000). Besides the techniques mentioned in this paragraph, Farha, Hupp and others have introduced XAS, EDX as well as more advanced spectroscopies to characterize the coordination geometry, oxidation state and distribution of metalated nodes. An interesting approach to understand the nature of metalated nodes was to use X-ray

Open Access Article. Published on 20 August 2020. Downloaded on 2/16/2026 6:59:12 AM.
This article is licensed under a Creative Commons Attribution 3.0 Unported Licence.

Table 4 Different metals or metal complexes supported on Zr_6 nodes of UiO-66, UiO-67 or NU-1000. A glossary of the techniques can be found below the table

Metal or metal complex	Topology	Spectroscopic characterization of PSM	Ref.
In^{3+} atoms	NU-1000(Zr)	XPDF, IR	305 and 311
Al^{3+}, Zn^{2+} atoms		SEM-EDX, DRIFTS	312 and 313
Co^{2+}, Cu^{2+}, Ni^{2+} atoms			314
Nb^{5+} atoms		DED	315
CoS_x		XPS, DRIFTS	316
ZnO_x species		Synchrotron XRD	317
NiS_2-like species		UV-vis, Raman, XPS	318
Co^{2+}–Al^{3+} sites		STEM-EDX, DED, DRIFTS	319
$Ir(CO)_2$	UiO-66(Zr) and NU-1000(Zr)	$^{12}CO/^{13}CO$-probe IR, EXAFS	320 and 321
Ni^{2+} atoms	NU-1000(Zr)	XANES, EXAFS, DRIFTS, SEM-EDX, XPS	322
V^{4+} and VO_x species	UiO-66(Zr)	XPS, Raman, DRIFTS	323
Zr^0-Benzyl sites	NU-1000(Hf)	XANES, DRIFTS, solid-state NMR, SEM-EDX	324 and 325
$Ni^{2+}(bpy)Cl_2$	NU-1000(Zr)	SEM, DRIFTS, UV-vis	326
$Ir^{3+}(P^tBu)Cl(res)$ pincer		Solid-state NMR, SEM-EDX	327
Co^{2+} atoms/CoO_x clusters		XANES, EXAFS, XPS, SEM-EDX, DRIFTS, DED	328
γ-Al_4 and γ-Al_8 clusters		XANES, EXAFS, DED, synchrotron XRD, SEM-EDX, solid-state NMR	329
Co–Cl, Fe–Br and Co–H	UiO-66/UiO-67(Zr) and UiO-type MOF	TEM-EDX, EXAFS, XANES, IR	330 and 331
Ir(COD)(phen)	UiO-67(Zr)	XRD, XPDF, DED, DRIFTS, XPS, XANES, EXAFS	332
$Rh(C_2H_4)_2(acac)$		DRIFTS, EXAFS	333
Al_2O_3 and $Ir(C_2H_4)_2(acac)$	NU-1000(Zr)	FT-IR	334
Pt atoms/clusters		IR, DED, XRD, XPDF, XANES, EXAFS	335 and 336
Cu–Oxo		XRD, XPS, DED	337
Ni(acac)/Ni(Facac)		XANES, EXAFS, XPS, SEM-EDX	338
Rh–Ga		STEM-EDX, DED, XANES, EXAFS	339
$Cr^{2+/3+}$ atoms		SEM-EDX, XPS, single-crystal XRD	340
$Ce^{4+/3+}{}_xO_yH_z$		XPDF, DED, DRIFTS, XPS	341
TiO_x/NbO_x		XRD, XPS, DRIFTS	342
Organometallic complexes		Various	309
Cu NPs	NU-901(Zr) and NU-907(Zr)	Synchrotron XRD, XPDF, DFT calculations	343

X-ray pair distribution function (XPDF), scanning electron microscopy energy dispersive X-ray spectroscopy (SEM-EDX), X-ray photoelectron spectroscopy (XPS), diffuse reflectance infrared Fourier transform spectroscopy (DRIFTS), difference envelope density (DED), scanning transmission electron microscopy (STEM), extended X-ray absorption fine structure (EXAFS), X-ray absorption near edge spectroscopy (XANES).

PDF, as reported by Kim *et al.*,[305] after functionalizing the NU-1000 nodes with In^{3+} atoms by AIM. Differential PDF revealed two peaks at 2.12 and 3.33 Å corresponding to In–O nearest and In···Zr next-nearest neighbour distances, respectively. A broader feature at ~4 Å reflects long range In···Zr neighbours within the Zr-node, exhibiting a higher degree of structural disorder. No In···In features were observed, suggesting that In atoms do not order relative to each other. However, the absence of In···In bonds could – for example – also imply that not all node sites available for metalation are occupied by In. Therefore, the application of complementary characterization methods to corroborate such finding is important to properly assess all aspects of metalation. For example, Li *et al.*[306] deposited Co atoms on the nodes of NU-1000 both by SIM and AIM and provided a full description of the metal species with a combination of X-ray and vibrational spectroscopy. DRIFTS of the functionalized material revealed lower intensity of the OH vibrations (*ca.* 3800–3600 cm^{-1}) after compared to before loading, suggesting Co^{2+} binding to the node-O atoms. A XANES pre-edge feature at 7709.2 eV ($1s \rightarrow 3d$) on Co-metalated NU-1000 short after deposition indicated Co^{2+} species, further corroborated by XPS *via* a satellite $2p_{3/2}$ peak of CoO at 786 eV. Activation in O_2 yielded Co^{3+} species as indicated by a small increase in the pre-edge feature together with a decrease in the white-line intensity, implying a mixture of Co^{2+} and Co^{3+} oxides is obtained (Fig. 14). A spinel structure was suggested from EXAFS analysis of the oxidized material which showed tetrahedral Co centres after loss of the OH groups and reduced coordination numbers of 0.8 for Co-SIM, 0.7 for Co-AIM and a decrease in Co–O neighbour distance to ~1.96 Å. Two new peaks at *ca.* 2.4 and 3.1 Å matching with the Co_3O_4 structure, strengthened the hypothesis of such structure on the nodes. However, it should be clearly noted that drawing the latter conclusion based on the Fourier transformed EXAFS signal peaks may imply a certain risk given that signal interference in *k*-space can induce significant *R*-space artefacts which are not directly related to the physical presence of neighbours, thus leading to inconsistent interpretations.

Besides DRIFTS, XAS and XPS, a recently developed technique termed difference envelope density (DED), which can be derived from XRD data, was used.[307,308] Subtraction of the electron density corresponding to the crystalline sections, *i.e.* the framework itself, from the electron density measured after introduction of Co generates 3D coarse maps such as the ones in Fig. 14e and f. Therein, the Co is found at *ca.* 8 Å along the *c*-axis. Computational support was given by calculating density functionals for different Co species and correlating them to the experimental data. This article provides an excellent example of the complexes approach necessary for describing this type of materials in a consistent

 This journal is © The Royal Society of Chemistry 2020

Open Access Article. Published on 20 August 2020. Downloaded on 2/16/2026 6:59:12 AM.
This article is licensed under a Creative Commons Attribution 3.0 Unported Licence.

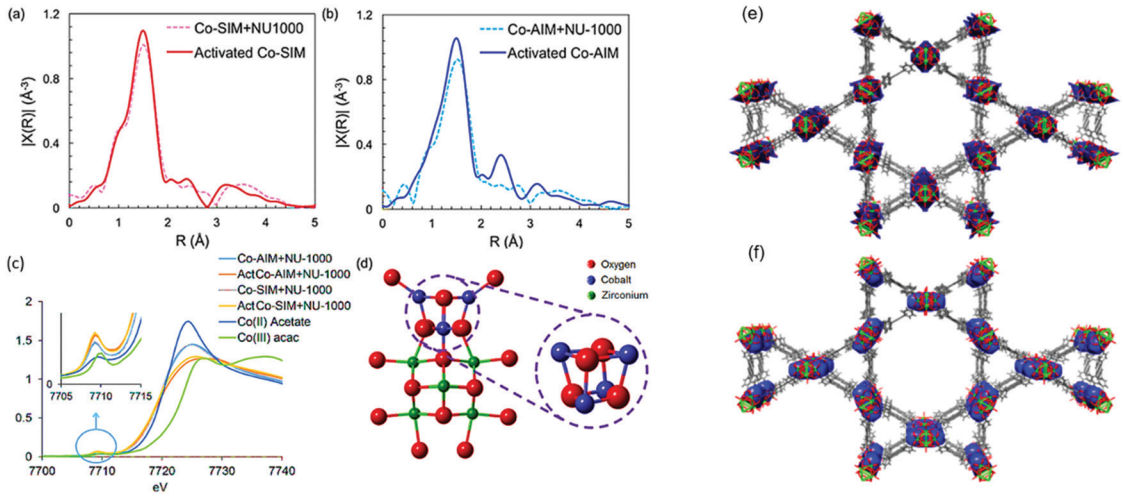

Fig. 14 k^2-Weighted magnitude of the Fourier Transform of the X-ray absorption spectra of Co atoms metalated to Zr_6 nodes of NU-1000 from the (a) liquid (SIM) and (b) gas (AIM) phase deposition, before and after activation in a O_2 at 503 K for 4 h. (c) X-ray absorption spectra at the Co K_α edge of the different Co-NU-1000 as-synthesized and oxidized (inset shows pre-edge). (d) A proposed structural change of Co-AIM + NU-1000 upon activation. This tetranuclear cobalt cluster can be related to local structural features in spinel Co_3O_4. Difference envelope density of Co introduced *via* (e) liquid-phase and (f) gas-phase Co clusters deposited within the pores, in close vicinity of the nodes. Adapted and reprinted from ref. 306. Copyright©American Chemical Society 2017.

manner, even more so when metal atoms have multiple stable oxidic structures. They have continued to extend the library of precursors and complexes that can be deposited from the gas-phase, truly making a widely applicable methodology out of this protocol.[309]

3.2 Grafted coordination complexes

As very recently highlighted by Drake *et al.*,[310] MOFs offer a particularly suited scaffold for preparing homogeneous catalytic complex replicates anchored to their ligands. Several ligand-containing linkers have been used (*e.g.* phosphines, bipyridyl, β-diketimine, salicylaldehyde) along with different metals, for different applications. However, the most studied system has been the partially substituted UiO-67-bpy, where the 4,4′-bpdc (4,4′-biphenyl dicarboxylate) linker is partially replaced 5–10% bpydc (2,2′-bipyridine-5,5′-di-carboxylate). Platero-Prats *et al.* first reported a XAS-XRD study on the one-pot synthesis of homogeneous-like UiO-67-anchored Pd, Ir and Rh complexes.[344,345] Øien *et al.* used (*in situ*) XANES and EXAFS to monitor the oxidation state and ligand exchange reactions in UiO-67-bpydc$Pt^{2+}Cl_2$, respectively, during (i) high-temperature H_2 reduction of Pt^{2+} to Pt^0, (ii) oxidation to Pt^{4+} with liquid Br_2 and (iii) ligand exchange with thiol-containing molecules (Fig. 15).[346] Analysis of the coordination geometry and oxidation state of the ligated metal provided real-time insight in the nature of the resulting complexes. In addition, resonant-inelastic X-ray scattering (RIXS) on both UiO-67-bpydc$Pt^{2+}Cl_2$ and the complex $PtCl_2(H_2bpydc)$ allowed to probe the difference in electronic states when Pt is incorporated in the framework or not. Besides X-ray based characterization, CO-probe molecule IR was used to monitor the strong undercoordination of Pt^0 sites *via* the detection of bpydc$Pt^0(CO)_2$ dicarbonyl complexes as well as to exclude the formation of Pt–H hydride-type species. This study shows the potential of *operando* and *in situ* XAS for studying single-site metal-loaded (4,4′-bpy)UiO-67 or other MOFs and has been further extended for other processes: reduction of Pt^{2+} sites in either H_2 or He to form Pt NPs,[347] CO_2 hydrogenation with Pt NPs,[348] *operando* hydrogenation of olefins with Pd[349] and incorporation of $CuCl_2$ and its redox-chemistry.[350,351] Yet another example was reported by Van Velthoven *et al.* have reported this approach to graft S,O-containing ligands to the Zr_6 nodes of MOF-808 then treated with Pd salts. Again, combining NMR to prove the successful grafting of the organic ligands, and HAADF-STEM together with XAS, they ruled out the formation of Pd NPs before and after catalysis. We can only stress how important is to use all these tools to rule out any extraneous species resulting in catalytic acivity.[352]

Other complementary techniques such as UV-vis, as in the case of Cu, or XPS are useful tools for collecting corroborating evidence. Indeed, incorporation of $CuBr_2$ in the same UiO-67 scaffold has been studied by Toyao *et al.*[353] and the nature of the bonded (4,4′-bpy)UiO-67-$CuBr_2$ species has been studied by UV-vis in addition to XAS. In the case of metal ripening that leads to the formation of NP@MOF composites, it is necessary to note the importance of *in situ* XAS for studying the evolution of metals under relevant conditions as well as TEM to disclose the formation of clusters.[354] In summary, the use of complementary techniques is necessary to fully understand the nature and functioning of the post-synthetically introduced species on/in MOFs. On the one hand, when adding metals to the material, X-ray based (XAS, XRF, XPS, EM-EDX), electronic (UV-vis-NIR) and magnetic (EPR, Mößbauer) techniques are invaluable for assessing their properties. On the other hand, in the case of organic functionalities, solid state and liquid NMR, as well as FT-IR and Raman spectroscopy are more suitable for characterization. The possible non-periodicity of

Open Access Article. Published on 20 August 2020. Downloaded on 2/16/2026 6:59:12 AM.
This article is licensed under a Creative Commons Attribution 3.0 Unported Licence.

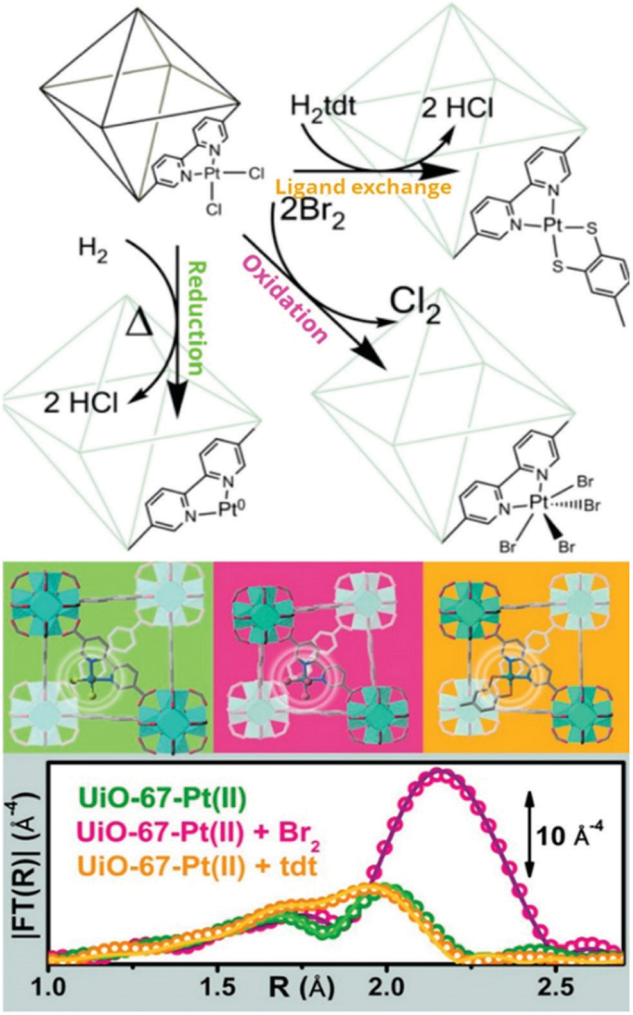

Fig. 15 (4,4′-bpy)UiO-67 functionalized with Pt and the different treatments that were followed by X-ray absorption spectroscopy, as well as their observed reaction mechanism. Adapted and reprinted from ref. 346. Copyright® American Chemical Society 2015.

the post-synthesis modified functionality (see example of the non-ordered In^{3+} atoms in Kim *et al.*[305] above), limits the power of the much more used single-crystal XRD. This suggests great opportunities for sensitive characterization tools that do not require long-range order, and potentially, micro-spectroscopic techniques too.

4. Metal–organic framework thin-films

So far, we have described spectroscopy and microscopy case studies using MOF powders and/or MOF single crystals. However, MOFs grown as films onto various substrates are increasingly relevant for applications such as sensors, opto-electronic devices or even catalytic membranes.[283,355–361] As an added benefit, MOF thin films are highly interesting model systems for understand physicochemical processes in *e.g.* synthesis or catalysis. As opposed to MOF powders, thin films can be challenging to routinely characterize with conventional spectroscopic techniques, such as transmission IR spectroscopy or XRD, due to the low amount of material and high spatial resolution needed for thin film features. Therefore, other less commonly used and/or novel methods, such as IRRAS, AFM-IR or AFM combined with Tip-Enhanced Raman Spectroscopy (TERS) (*vide supra*), respectively, have been used.

In the following paragraphs, we will present the use of these techniques through different examples published over the last few years. In particular, we will focus the discussion on surface-mounted metal–organic frameworks (SURMOFs), a subclass of thin films first described in 2007 by Shekhah *et al.*[362] The authors showed the now widely used technique of SURMOF fabrication through liquid-phase epitaxy (LPE).[264,363] This technique allows not only for a certain degree of control of the crystal growth orientation, but also for the deposition of metastable MOFs unable to form through conventional solvothermal synthesis, such as MOFs with larger pores without the presence of an additional interpenetrating lattice.[364,365] Within this context, the selected examples showcase the relevance of novel tools to study SURMOFs as a system to understand physicochemical processes in MOF optimization.

4.1 Liquid-phase epitaxy synthesis

Several extensive reviews on layer-by-layer (LbL) synthesis of SURMOFs have been published.[363,366–368] However, with the main focus on synthesis, an overall view on the use of spectroscopy to characterize SURMOFs is still missing, and will be precisely the focus of the following sub-sections. Using Cu_2BTC_3 SURMOF, Shekhah *et al.* showed the LbL synthesis of highly crystalline, homogeneous thin films, as well as the directing effect of self-assembled monolayers (SAMs).[369,370] When using carboxylic acid terminated thiols, mimicking the functionality of the BTC linkers, the XRD diffractogram merely showed reflections for the [100] direction. Alternatively, a pure [111] orientation was achieved by using hydroxyl terminated SAMs, resembling the axial position in the Cu paddlewheel. In both cases, a smooth (crystalline) structure was confirmed by electron microscopy.

However, in contrast to the seemingly defect-free crystal structure of Cu_3BTC_2 SURMOF showed by electron microscopy, several reports point towards the presence of defects with spectroscopy. Gu *et al.* synthesized HKUST-1 on quartz sheets using a LbL with and without ultrasonication step. They showed that the ultrasonication step lead to lower surface roughness and used UV-vis spectroscopy to point out that these SURMOFs have lower amounts of defects, together with their more transparent colour. The IR spectroscopy results published by St. Petkov *et al.*[285] also highlight the presence of defects. The authors found a second absorption band in CO-adsorbed IR spectra, next to the typical band of CO adsorbed in the apical positions of the paddlewheel (2179 cm^{-1}). This smaller second band at 2121 cm^{-1} points to the presence of CO adsorbed on a minority of Cu^+ species of non-coordinated metal ions.[285] This result was further confirmed by XPS, which corroborated the presence of up to 8% of Cu-coordination defects. CO adsorption

Open Access Article. Published on 20 August 2020. Downloaded on 2/16/2026 6:59:12 AM.
This article is licensed under a Creative Commons Attribution 3.0 Unported Licence.

on thin films was also studied by Mandemaker *et al.* using IR spectroscopy to directly compare thin films, made using the LbL synthesis, to bulk HKUST-1 crystals.[371] To this means, calcium fluoride windows were functionalized with the proper SAM, which turned out to be trifluoromethyl-terminated benzene carboxylic acid or alcohol, after an essential UV-ozone treatment of the CaF_2 surface. Both wafers of bulk HKUST-1 and the CaF_2-mounted SURMOF were measured using FT-IR while CO or NO were dosed. Resulting from this, it was concluded that the MOF film contained 1.9 times less Cu^+ species than the commercially available powder. Furthermore, the low amount of Cu^+ species present was in paddlewheel conformation. To gain further insight into the nature and origin of these defects formed in the LbL synthesis, Delen *et al.*[372] used both far-field (IRRAS) and near-field infrared spectroscopy (AFM-IR). Specifically, the authors measured IRRAS spectra during-, and post-synthesis, using commonly used Cu_3BTC_2 SURMOF synthesis protocols. An IR band at 1675 cm^{-1} was found to belong to the copper(II) acetate precursor, rather than the previously assumed fully coordinated MOF material. Nano-spectroscopic AFM-IR, combining the high spatial resolution and sensitivity of an AFM-tip as a detector while the underlying sample surface is irradiated using IR-lasers, was then further able to pinpoint individual vibrations corresponding to varying degrees of Cu-paddlewheel substitution.

This insight into the HKUST-1 synthesized allowed the authors for a larger control on the SURMOF synthesis. Particularly, the authors found that by tuning certain synthesis parameters, they could largely influence crystallinity and defect concentrations. The relevance of nano-spectroscopy techniques study these defects, such as AFM-IR, was also highlighted by Mandemaker *et al.*[373] Using the high-spatial resolution of AFM-IR (Fig. 16a), the authors observed the desorption of the self-assembled monolayer (SAM) layer upon HKUST-1 synthesis at elevated temperatures (Fig. 16a). The strong band at 1700–1800 cm^{-1}, attributed to the SAM carboxylates C=O stretching vibration, was non-present for the areas indicated in blue (Fig. 16b, blue regions and blue spectra). This explained a quenching of nucleation observed by using *in situ* liquid-phase AFM during this synthesis at 323 K. Furthermore, the authors showed that a layer was formed as a 'carpet' surrounding the bigger crystals, debatably not as crystalline but as defect-rich Cu_3BTC_2.

In another recent instance, micro-spectroscopy was utilized to understand the topology-defect relation in SURZIF-8(Zn) thin films. Combining AFM, Raman, post-processing of the data using PCA and DFT to further identify chemical fingerprints, Weckhuysen *et al.* pinpointed the inter-grown nature of the SURZIFs (Fig. 16c). Through different spectral regions they were able to quantify the defect-richness: a sharp band at 284 cm^{-1},

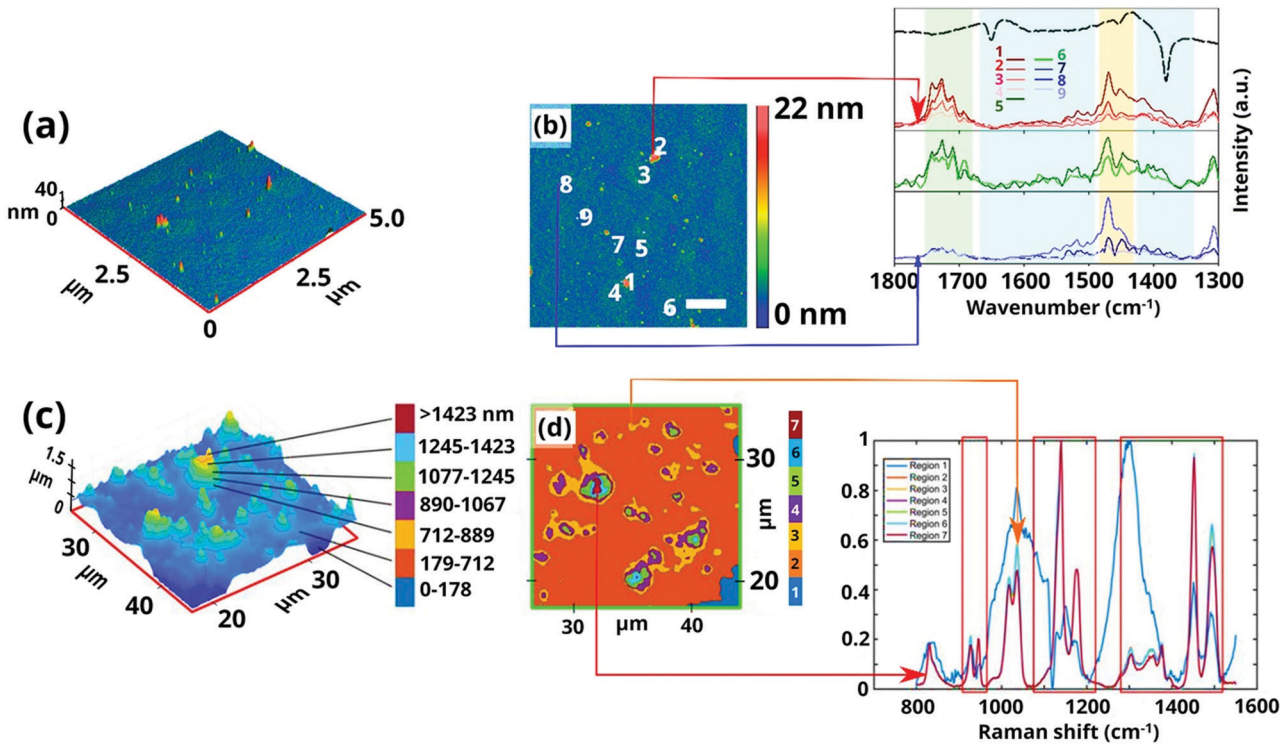

Fig. 16 (a) 3D representation of an (b) atom force microscopy micrograph and the corresponding infrared spectra (right), labelled by numbers and sorted on morphological feature (red = grain, green = circle/patch, blue = in-between patches), highlighting the removal of self-assembled monolayer (C=O stretch) in the blue areas. Scale bar in (b) represents 1 µm. Reproduced from ref. 373 with permission from John Wiley & Sons, copyright 2017. Note that the 3D representation was originally not published in the work, but directly obtained from the data represented in (b). (c) 3D representation of an AFM micrograph showing height segmentation, which are used as (d) regions to average Raman spectra over the given region to give chemical information using spectroscopic fingerprints correlated to topography. Colour code of the Raman relates to the colour code of each region of the map on the left. Reproduced from ref. 374 with permission from John Wiley & Sons, copyright 2019.

Open Access Article. Published on 20 August 2020. Downloaded on 2/16/2026 6:59:12 AM.
This article is licensed under a Creative Commons Attribution 3.0 Unported Licence.

high 675/686 cm^{-1} ratio, low intensity for the 1180 cm^{-1} band (representing Zn^{2+} with a single linker), a low 1135/1144 cm^{-1} band ratio and a low 1458/1498 cm^{-1} band ratio (quantifying the amount of free linkers) is representative for a defect-poor material.

Using these fingerprints, the work revealed the existence of phase boundaries within 20-cycles thin-films, while applying more layers (50-cycles) yielded more (chemically) homogeneous films.[374] Not only for the case in which the MOF grows directly on the substrate, but also for mixed nucleation and growth processes AFM can be used to determine film morphology. For instance, Öztürk *et al.* studied the influence of different parameters, such as reagent ratio or temperature, on the crystallization of ZIF-8 and ZIF-67 deposited on Au substrates.[375] Moreover, film quality (*i.e.* density and packing onto the substrate), can be carefully tuned by choosing the appropriate number of deposition steps (Fig. 17). This has been taken to the next level by Mandemaker *et al.*, who was able to tune the morphology showing a direct impact on the catalytic properties of Cu-BTC nanowebs.[376] By tuning the deposition rate by spin-coating, the aspect-ratio and crystalline phase of the so-called nanowebs was modified, and thus, the amount of Cu^{+} and Brønsted sites on surface. This work further corroborated the necessity of using nanoscale tools to study film morphology, coupled with vibrational spectroscopy that provides chemical information on the materials. This, in term, allows for an extremely detailed characterization of the films.

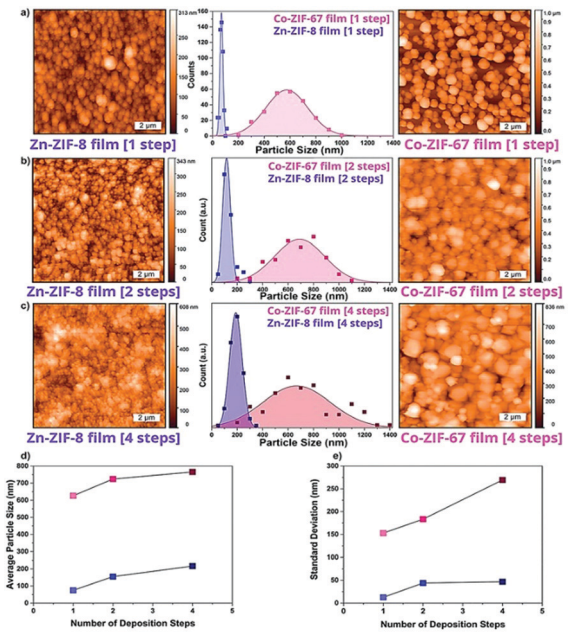

Fig. 17 AFM topographical maps and particle size distributions of ZIF-8(Zn) (purple) and ZIF-67(Co) (pink) films prepared by direct synthesis of (a) 1 step, (b) 2 steps and (c) 4 steps. All the scalebars represent 2 μm. The variation of number of particles per mm^2 and average particle size through multiple deposition steps (d), and (e) standard deviation of the given particle size distributions (metal/linker: 1 : 6.6, 20 °C, each deposition step with a time of 10 min). Adapted and reprinted with permission from ref. 375. Copyright 2017 John Wiley & Sons, Inc.

4.2 Heteroepitaxial SURMOF hybrids

The fabrication of core–shell type MOFs opens the gateway to more advanced functional materials for different applications, such as selective adsorption of gaseous compounds or tandem catalysis, in the electrochemical reduction of CO_2, for example.[377–380] To develop such heterogeneous systems, SURMOFs provide an ideal model system, as the vertical composition can be easily altered during synthesis. The successful creation of a hetero-MOF crucially depends on the lattice matching of the stacking compounds. Studies on isoreticular SURMOF hybrids with varying degrees of strain have been published. Examples are top-layers with different metal ions, additional linker functionalization (*e.g.* amine groups), and varied linker length.[378,380–382] For all SURMOFs it was shown with grazing incidence (GI-)XRD that the orienting effects exerted by the SAMs traverse to the shell layer(s). More specifically, Wang *et al.* highlighted the versatility of this approach in a trilayer SURMOF-2 thin film.[382] In a hierarchal fashion, they grew a SURMOF with linkers of 1.12, 1.34, and 1.55 nm. Out-of-plane XRD showed that despite the large lattice mismatches of up to 20%, highly crystalline and oriented Cu-BPDC/Cu-NDC/Cu-BDC (where BPDC = 4,4′-biphenyl dicarboxylate and; NDC = 1,4-naphthalene dicarboxylate) SURMOF was made. The stratified arrangement was corroborated by SEM of the films stained with an Eu contrast agent, fitted only to the larger pores. Quantum chemical calculations on this system explained this unusual phenomenon in which the lattice strained is distributed onto the whole multi-linker film. The energy cost for this effect is lower than that of creating a defect site (*i.e.* dangling bond). In summary, through a combination of GI-XRD, SEM and theory, the authors could explain the complexity of defect formation in films. Compared to zeolites, MOFs are often reported to possess low (hydro-)thermal stability, making them a less obvious choice for industrial catalysis. However, apart from a number of XRD studies on bulk MOF at ambient temperature and pressure,[383] few details on the stability of SURMOFs under elevated temperature and pressure are known. To this end, Brand *et al.* developed an *in situ* AFM utilizing a high temperature/pressure autoclave cell and combined it with *ex situ* IRRAS analysis.[384] They used SURMOF substrates with individual grains of HKUST-1 and reported a limited thermal stability of HKUST-1 (up to 333 K), but a high mechanical stability against high pressures (up to at least 20 bar). This was concluded from both the disappearance of grains in the AFM micrographs and a decrease in HKUST-1 band intensities in the IR spectra when the sample was put at 333 K. Furthermore, they showed the morphological changes to be mostly reversible.

Although not specifically mentioned in this work yet, as the focus is on spectroscopic, microscopic and diffraction-based techniques, it should be noted that for the characterization of SURMOFs the application of the quartz-crystal microbalance (QCM) has shown to be a strong toolbox. Given examples are found in the work from Stavila *et al.*, that applied QCM to study growth kinetics, Heinke *et al.*, which used QCM to measure diffusion coefficients and Wannapaiboon *et al.* which studied the loading of a SURMOF with guests.

 This journal is © The Royal Society of Chemistry 2020

Open Access Article. Published on 20 August 2020. Downloaded on 2/16/2026 6:59:12 AM.
This article is licensed under a Creative Commons Attribution 3.0 Unported Licence.

5. Characterization of catalytic processes

Owing to the compositional flexibility of MOFs, meticulously selected metal and linker types can yield tailored functionalities and pore space topologies after their *de novo* synthesis. In addition, MOFs can be employed as scaffold (or equivalently catalyst support) for anchoring catalytically active sites by post-synthesis modification.[53,385] These active sites range from (i) metal atoms or NPs on MOF nodes, mimicking metal atoms or NP on metal oxide supports, to (ii) metals bound to functionalized linkers, resembling anchored homogeneous catalyst complexes, and (iii) node-linker units functioning as repetitively arrayed synthetic enzyme biocatalysts. In this respect, MOFs can expose a broader class of functionalities to anchor groups and their pores more easily tuned than in the case of zeolites. Therefore, MOFs are endowed with great potential to provide a diverse platform for catalytic model studies.

5.1 *In situ* and *operando* spectroscopy of metal–organic frameworks

Diffraction techniques, and obviously, single-crystal diffraction, are well suited when large crystals of a specific topology can be grown. Since MOFs offer the advantage of having repetitively ordered unit cells with well-defined, isolated sites, its structural periodicity allows for real space reconstruction of the lattice with high precision.[52,385,386] MOFs can thus serve as model systems for real catalysts, such as single-site or single-atom heterogeneous catalysts or homogeneous catalyst complexes, by synthetically anchoring them in these periodic structures. As an example, Burgun *et al.* have reported the possibility of studying rhodium catalysed acetaldehyde synthesis with single-crystal XRD.[387] A Mn(II)-based MOF with pyrazolyl moieties embedded in the linker was post-metalated with $[Rh(CO)_2][Rh(CO)_2Cl_2]$ to create the environment of classical hydroformylation catalysts. After installing this complex, the MOF crystals were treated with methyl bromide and were subsequently CO infused (Fig. 18). Single-crystal XRD of the material was obtained for each step, allowing the authors to obtain a definitive snapshot of each step. Although the mechanism of this reaction is long known, the interest lies in locating every atom during the catalytic cycle, which may be of interest for other reactions (*e.g.* chiral catalysts). This work shows the power of single-crystal XRD, in a quasi *in situ* approach, to unravel the catalytic reaction cycle in MOF model systems. This has been exploited in the past years, the potential of this strategy being huge as reviewed by Doonan and Sumby.[388–390] However, whilst diffraction is heavily used for MOF characterization and spectroscopies become more popular, MOFs in the form of nanocrystalline powders or with heterogeneous compositions are typically used for real application studies. This question has been raised by some, and in fact some structures are not available yet as single-crystals, *e.g.* MIL-53(Cr) or MIL-100(Cr), and are extremely difficult, if possible, at all, to be obtained as single-crystals.[391] This limits the use of single-crystal XRD for model studies, indicating the need of other bulk techniques.

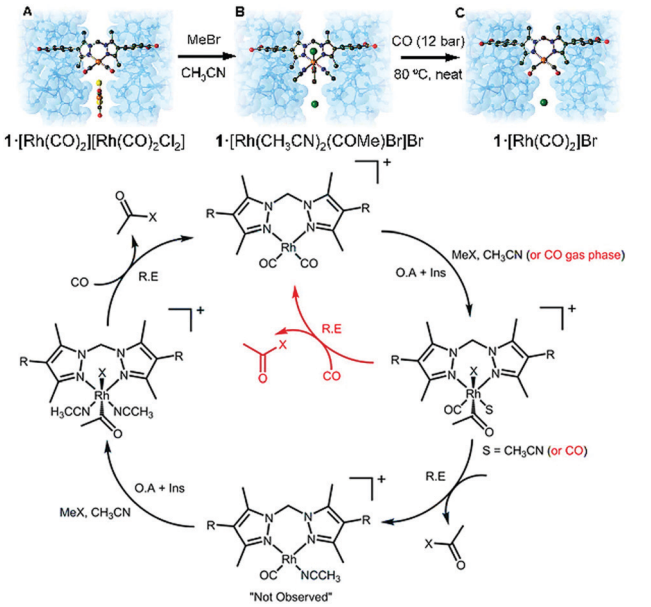

Fig. 18 Single-crystal XRD representations of MOF **1**, after (A) installing the Rh complex, (B) treatment with methyl bromide and (C) carbonylation of the methyl group releasing Br^- anions. The MOF backbone is shown in blue with a transparent van der Waals surface; C black; N dark blue; O red; Rh orange, Cl yellow; Br green. The catalytic cycle shown below the crystal structures corresponds to the different steps observed by SCXRD. Adapted and reprinted with permission from ref. 387. Copyright © John Wiley & Sons, Inc. 2017.

Thus, besides, techniques under operation conditions, *i.e.* *in situ* or *operando*, need to be used for the study of catalytic or gas sorption processes.[392] X-ray spectroscopies, such as XAS, XES, XPS, EDX, electronic spectroscopies, such as UV-vis, and magnetic techniques, such as EPR, Mößbauer are highly sensitive to most metals with which MOFs are formed. Additionally, Raman and (probe-molecule) IR spectroscopy can provide insight into the nature of the metal phase. Notable examples of this strategy for the separation of propylene and propane with MIL-100(Fe) have been detailed in Section 2.2.2, and more recently, the speculative formation of high spin Fe^{IV}=O species upon oxidation of MIL-100(Fe) sites with N_2O, as suggested by Simons *et al.* by means of extensive *in situ* XAS, Mössbauer spectroscopy and DFT simulations.[393] On the other hand, NMR, Raman and IR spectroscopy can characterize the linker properties and how they evolved during operation. It is then necessary for the MOF community to stir their studies towards the use of this set of techniques in *operando* mode.

Concerning the use of MOFs as model systems (or performance materials), the weakness is still their stability under relevant conditions, namely high-temperature, pressure or extreme pH. Thus, as recently highlighted by Gates *et al.*,[53] MOF catalysts should be directed to appropriate reactions that require mild conditions. These cases will require (already do) very advanced and sensitive techniques, owing to the fact that they may appear only under dynamic conditions and/or in very small detectable concentrations.[39,394] Moreover, apparently simple processes, such as pore degassing, may reveal much

Open Access Article. Published on 20 August 2020. Downloaded on 2/16/2026 6:59:12 AM.
This article is licensed under a Creative Commons Attribution 3.0 Unported Licence.

more complex scenarios than initially hypothesized, as recently demonstrated by Dodson *et al.*[395] Another possible pitfall resides in the sensitivity of spectroscopic techniques to the detection of reaction intermediates within catalytic reaction cycles. More particularly, the strong spectroscopic fingerprint of the MOF framework itself could dominate the spectroscopic contribution of the investigated reaction intermediate of catalytic MOFs. Finally, stability under the measuring beam, being electrons, neutrons, X-rays or even light, could potentially perturb or degrade the framework structure and measured properties. To prevent artefacts and false conclusions, degradation testing should be performed prior to experimentation. Despite these potential drawbacks, we foresee that MOFs will be used as model catalysts in the upcoming years. Researchers in the field need to approach most of aspects with a wide range of characterization techniques (holistic approach) to obtain a good understanding of MOF materials. Several other species that may appear during synthesis, activation or operation (*e.g.* lattice interpenetration, unreacted bonded molecules, defect linkers, amorphous regions or changes in the structure) must be considered.

6. Challenges and opportunities in spectroscopy of metal–organic frameworks

Besides the physicochemical phenomena discussed above, a vast number of other features (*e.g.* photon absorption and non-linear optics,[396,397] drug release,[398] photocatalytic processes,[399] heat absorption/release,[400] electro-conductivity[401–403] or chemical sensing[23,404]) that lay beyond the scope of our review article may become grand challenges for characterization, let it be spectroscopy, scattering or diffraction. All these will require the use of *ad hoc* developed techniques, both bulk and spatially resolved.

6.1 Chemical imaging and spatially resolved studies of bulk MOFs

Spatially resolved characterization of different features, *e.g.* chemical composition, at the nanoscale is and will be one of the major challenges in MOF chemistry. Given the heterogeneous composition in terms of elements, oxidation states, geometric configurations, *etc.* present in such complex materials, very advanced techniques are necessary to tackle the lack of insight.

For instance, the problem of metallic spatial has not been yet thoroughly studied. Some works that make use of bulk (*e.g.* powder diffraction) techniques show indirect proof of metal mixing in some topologies other than MOF-5.[405–411] For example, very recently, solid-solutions in the $x = 0$ to 1 compositional range of $Zn_{1-x}Cd_x$ in ZIF-8 were studied by high-temperature XRD,[412] with the subsequent structure refinement, together with non-negative matrix factorisation (NMF) analysis of the IR spectrum. The authors were able to correlate the thermal expansion coefficient α to the arrangement of cations in the lattice. Although some degree of detail can be obtained by widely available SEM/TEM-EDX as a routine tool,[413] fundamental studies in direct imaging with atomic resolution are still lacking. In spite of all these advances and other impressive reports in which high-resolution (HR)-TEM (which is limited by beam damage) has been used,[414–416] there is still a lack of spatially resolved studies on metal distribution in MTV-MOFs.

Besides multi-metallic MOFs, linker-distribution in multivariate (MTV)-MOFs, which are becoming an important area of research.[417] Although indirect using NMR certainly represented a step forward in the characterization of MTV-MOFs,[418] they do not provide imaging, direct evidence of the spatial linker distribution. Seminal works of this type have been previously published,[234,250] but the field remains far from explored. In this sense, Katzenmeyer *et al.*[419] applied photothermal induced resonance (PTIR) to study the chemical complexity of MTV-MIL-68(In) crystals. This technique combines the lateral resolution of AFM with the chemical specificity of IR, obtaining chemical information with nanoscale resolution (100 nm). MTV-MIL-68(In) was prepared from an equimolar mixture of NH_2- and non-functionalized terephthalic acid and the resulting crystals were characterized by PTIR at different locations. In line with previous results (see above), the similar spectra obtained pointed to a homogeneous linker distribution down to *ca.* 100 nm (Fig. 5).

This work showcases the suitability of PTIR to characterize MOFs and nicely proves the MTV-MIL-68(In) linker homogeneity and the heterogeneous domains of crystals prepared by sequential growth (Fig. 19). In this respect, different techniques have been developed to chemically image solid materials with nanoscale resolution and may be of great use in such cases.[420] An overview of the different methods available for chemical imaging can be found in the review authored by Buurmans and Weckhuysen,[56,421] but due to their suitability, we would like to highlight AFM coupled with Tip-Enhanced Raman Spectroscopy (TERS) and element specific X-ray nanotomography. These techniques have been successfully applied to different heterogeneous catalysts in order to obtain chemical maps with 20 nm and sub-30 nm resolution, respectively.[422–424] Further, our group has recently used atom probe tomography (ATP) to examine the atomic-scale distribution of Si, O and Al in zeolite crystals. Although extremely challenging, this technique could provide crucial information on atomic distribution in MTV-MOF materials.[425]

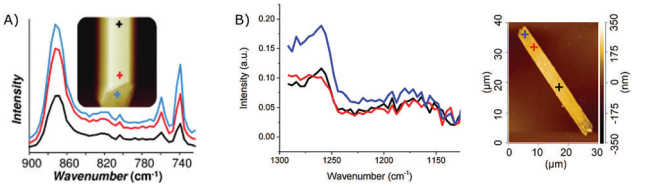

Fig. 19 Photothermal induced resonance (PTIR) spectra acquired at different spots of (A) MTV-MIL-68(In) crystals (bands at 742 cm^{-1} and 762 cm^{-1} correspond to the C–H out-of-plane bending vibration mode for MIL-68(In) and NH_2-MIL-68(In), respectively); and (B) crystals prepared by sequential growth (band at 1260 cm^{-1} corresponds to the C–N stretch vibration) showing a higher intensity on the blue spot (edge). Reprinted from ref. 419 Copyright©2014 John Wiley & Sons, Inc.

Open Access Article. Published on 20 August 2020. Downloaded on 2/16/2026 6:59:12 AM.
This article is licensed under a Creative Commons Attribution 3.0 Unported Licence.

Especially with respect to the most recent developments such as scanning near-field optical nanoscopic techniques and X-ray free electron lasers, micro- and nanoscopic tools have been developed with high speed during the past years to deliver unparalleled spatio-temporal resolution.[54,55] Recently, a fist-of-its-kind study was published by Jayachandrababu *et al.*,[426] wherein confocal fluorescence microscopy (CFM) and ^{1}H NMR CRAMPS showed core–shell structures for post-synthetically linker exchanged ZIFs by exciting with different laser wavelengths. More recently, Schrimpf *et al.*[427] have made use of Förster resonance energy transfer (FRET) and Fluorescence Lifetime Imaging (FLIM) to study the distribution and the presence of nanoscopic defects. These techniques are based on the energy transfer from one fluorophore donor to an acceptor, depending the efficiency of the transfer on the distance between molecules or groups. Thus, the emission can be correlated to the space between one dye linker and the other. In their study, they grafted fluorescein isothiocyanate (FITC) or rhodamine B isothiocyanate (RITC) with different concentrations to several 2-NH_2-BPDC (BPDC) groups in UiO-67(Zr) crystals. In Fig. 20a, a phasor plot shows that fluorescence decay depends on the crystal size, and the exchange time with FITC. Different spatial distributions of FTIC (Fig. 20b–d) are obtained for different crystals, indicating the heterogeneity of the process at the single-particle level as well. In our opinion, this study represents a breakthrough in studying spatial distribution of mixed-linker MOFs and the presence of defects. Another example of a spatially resolved study was authored by Ghosh *et al.*,[428] who observed local differences in solvent concentration within the pores of a HKUST-1 material as revealed by IR micro-spectroscopy in combination with NMF analysis. This shows that traditional synthesis protocols, even for archetypal MOFs, lead to heterogeneous materials at the molecular, nano- and microscale (both in composition and presence of residual molecules). Beyond chemical information, structural information may be obtained by other types of microscopy, *e.g.* SEM and TEM. MOFs may exhibit relatively limited stability under the electron beam, as we have previously discussed. Nevertheless, a number of high-resolution studies in which pore structures or polymorph transformations were visualized by means of aberration-corrected (AC)-TEM, have

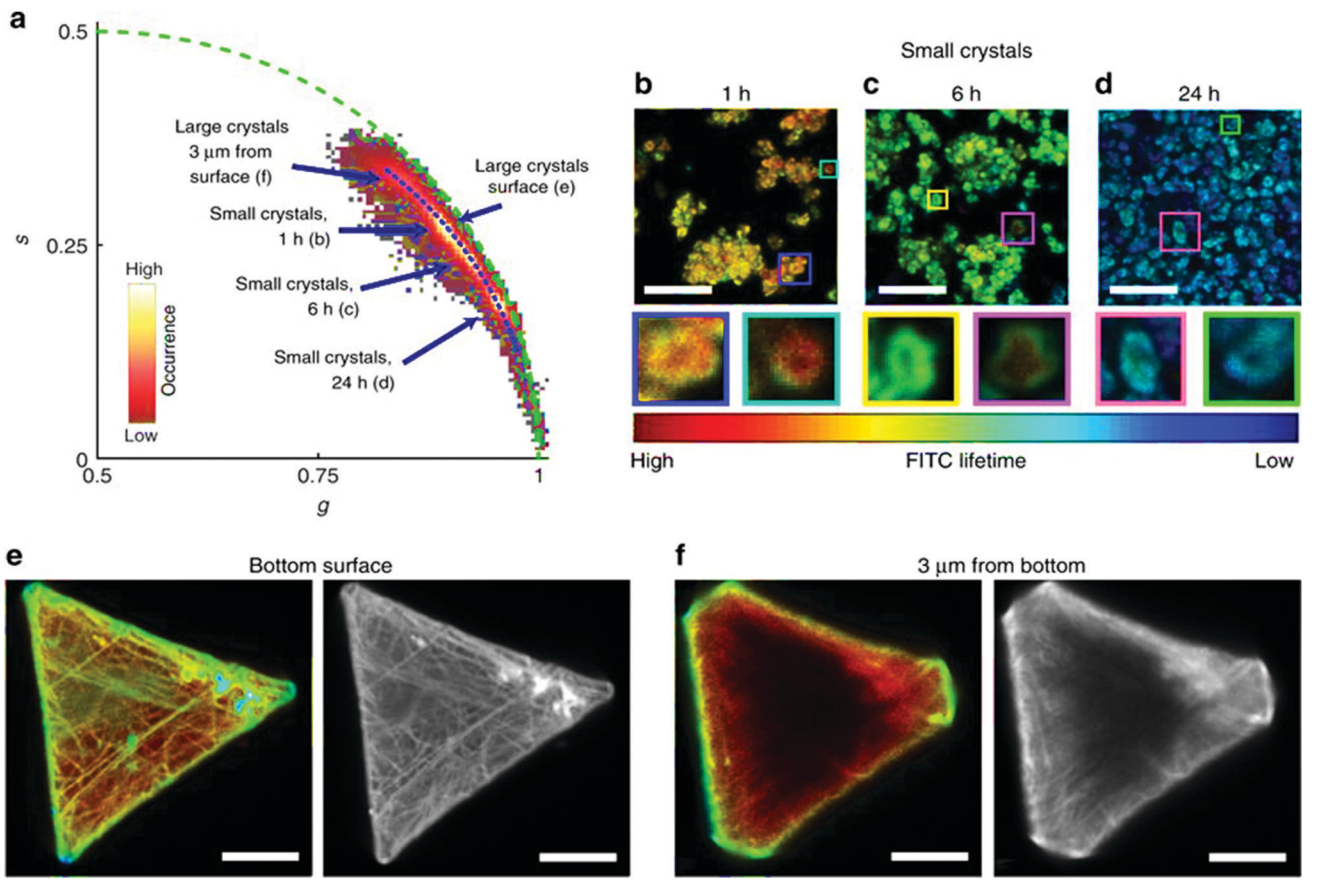

Fig. 20 Fluorescence Lifetime Imaging (FLIM) phasor data of UiO-67 samples functionalized with fluorescein isothiocyanate (FITC) using linker exchange. (a) A phasor plot of the images shown in (b–f). The blue arrows point at the average phasor positions of the different samples. (b–d) FLIM images of small crystal UiO-67 samples subjected to linker exchange with FITC-modified linkers at 338 K for 1 h (b), 6 h (b), and 24 h (c). The inserts below are magnifications of the coloured squares. (e and f) FLIM (in colour) and fluorescence intensity (in grey scale) images of large crystal UiO-67 samples subjected to linker exchange with FITC-modified linkers for 24 h. (e) An image recorded at the bottom surface of a crystal. (f) An image recorded inside the crystal, 3 μm up from the bottom surface. The colour coding of the images is based on the blue dotted line in panel a using the colour table shown in b. The scale bar of all images is 10 μm. Adapted and reprinted from ref. 427. Copyright © 2018 Nature Publishing Group.

Open Access Article. Published on 20 August 2020. Downloaded on 2/16/2026 6:59:12 AM.
This article is licensed under a Creative Commons Attribution 3.0 Unported Licence.

been published.[429–433] Besides spatially resolved characterization, MOFs may be used as platforms for developing other advanced spectroscopic techniques.

6.2 Use of metal@MOF composites as spectroscopic tools

Although metal@MOF composites lay beyond the scope of this review, the combination of MOFs with the enhancement of Raman effects on metal surfaces has been of particular interest.[434] For instance, embedded Au,[435–438] Ag[439–441] and even Au@Ag[442] nanostructures (*e.g.* rods, cubes, spherical crystals, stars) have been used to as SERS substrates to study different phenomena. For instance, Zhao *et al.* used plasmonic Ag octahedral nanocrystals coated with a layer of Al-porphyrin MOF, to study the metalation process of the porphyrin centres by means of enhanced Raman spectroscopy. This allowed them to map the enhancement effect for individual Ag ⊂ MOF particles.[443] In another example, Sim *et al.*[444] embedded Ag nanocrystals with which they could follow the carboxylation of aniline by enhanced Raman spectroscopy. It is interesting to highlight that a number of authors have reported SERS effect in the surfaces of MOFs without the use of metal nanostructures, purely by charge-transfer resonance effects with the MOF backbone, as demonstrated by theoretical calculations.[445,446] This opens the opportunity to directly study the formation of intermediates in catalysis or the interactions with liquid or gas adsorbates, on the MOF surface during sensing or gas sorption without the side effects of metal nanostructures. Not only for SERS, but also for catalysis and gas sorption charge transfer can be of high relevance. In fact, in their latest report, Olsbye and others offered a full picture of the interaction between Pt NPs and the framework during CO_2 hydrogenation is given.[447]

The key in this study is combining DFT simulations with *operando* IR and TEM tools to study reaction intermediates, to define what kind of products are formed and the role that the MOF plays as a support. Alternatively to IR or Raman, other techniques, such as hard XPS and NEXAFS have been used for studying orbital overlapping between Pd nanocubes and the HKUST-1(Cu) matrix and why this has impact in enhanced H_2 storage, showing the necessity of using very particular techniques in certain cases.[448]

6.3 Latest trends for *in situ* and spatially resolved studies

Apart from sensing, new techniques for studying *in situ* the crystallization of MOFs are being developed. As described in the previous sections, much research has been devoted to the *in situ* study of MOF formation. In this line, Stock and co-workers have developed the SynRAC cell for crystallization studies, which provides low signal-to-noise ratios and improved time-resolution to previous set-ups.[373] In showcase studies of a selected Bi-based coordination polymer, the presence of short-lived (previously undetectable) intermediates was observed.[449,450] Just as shown in Sections 2.1.2 and 5.1, this kind of mechanistic studies will become more important in the future if one wants to control the different phases present during crystallization. An example beyond synchrotron technique was reported by Van Cleuvenbergen *et al.*[451] The crystallization of ZIF-8 was followed by dynamic Angle-Resolved second harmonic scattering (dAR-SHS) shows an alternative way of obtaining relevant information about size, shape and concentration of MOFs during their formation. This summary show that MOFs are fostering progress in the development of techniques that could be used for many other types of materials. On the side of spatially resolved tools, the group of Kitagawa recently reported a study in which AFM under dynamic conditions showed layer restructuring in $[(Zn_2(1,4\text{-ndc})_2(\text{dabco}))_n]$ as a response to interactions with solvent molecules.[452] As seen here, already known and newly developed micro- and nanoscopic (X-ray, IR and Raman based) techniques will play a big role in the coming few years. For instance, chemical imaging by AFM-IR spectroscopy would probe dangling bonds or different linkers with resolution down to *ca.* 10 nm (Fig. 21a).

Another example would be the use of fluorescent probes and single-molecule fluorescence (the former already pioneered by Ameloot *et al.*[250] in 2009 for MOF materials) for imaging pore cavities,[453–457] or single-reaction (catalytic) events,[458,459]

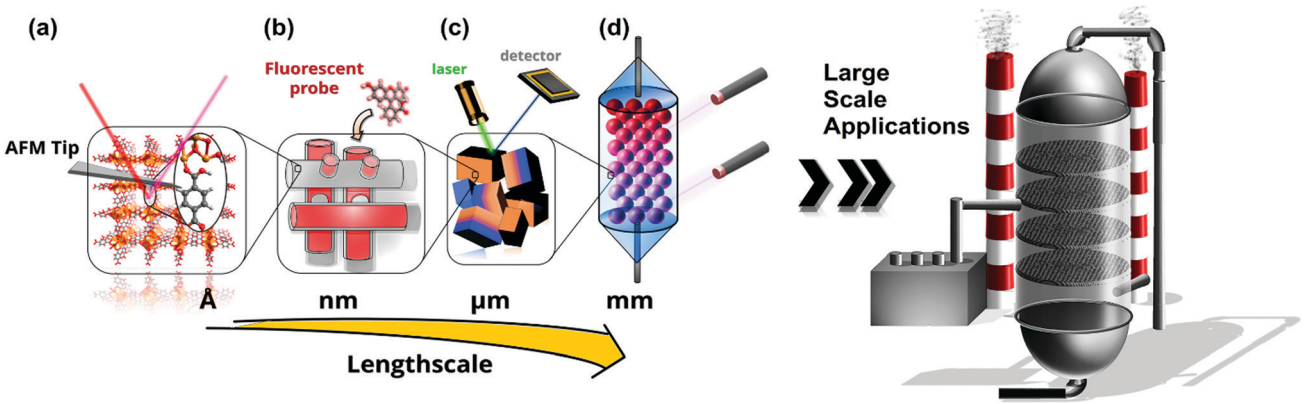

Fig. 21 Outlook of the challenges to be addressed in the future of metal–organic frameworks characterization at different lengthscales. (a) Microscopy at the (sub)nanometer scale by spatially resolved tools (*e.g.* AFM-IR spectroscopy); (b) diffusion and mass transport phenomena, tomographic reconstruction of pore networks by fluorescence and contrast-based techniques; (c) intra- and inter-particle hetereogeneities (orange and blue indicate distinct chemical compositions) studied by chemical mapping and (d) *in situ*/*operando* studies at the lab- and pilot-plant scale. A holistic approach will result in advanced understanding, thus, improved design of MOFs' properties, leading to optimized materials for large scale applications.

 This journal is © The Royal Society of Chemistry 2020

Open Access Article. Published on 20 August 2020. Downloaded on 2/16/2026 6:59:12 AM.
This article is licensed under a Creative Commons Attribution 3.0 Unported Licence.

respectively; polarized Raman microscopy with probe molecules[460] or tomography based on X-ray contrast[423,461] are a wide-open playground for the study of issues such as pore connectivity, gas and liquid diffusion barriers or separation properties in MOF crystals (Fig. 21b and c), which are crucial for regulating their performance in catalysis or gas sorption or separation.[25] Examples of such strategies, such as the one reported by the group of Caro, are starting to be reported.[462] These techniques have the potential to unravel physico-chemical phenomena to an unprecedented level of detail and will become more and more important. The importance of using microscopy has been recently highlighted by Rivera-Torrente *et al.* in the HKUST-1 system for two different applications. First, defect distribution was proven to be unequal at the inter-crystal level when 5-cyano-1,3-benzenedicarboxylic acid and 1,3,5-benzenetricarboxylic acid were mixed in the hydrothermal solution.[432] In this case, the use of Raman microscopy was invaluable due to its high spatial resolution and chemical specificity for each linker. Further, in another study, a combination of Raman microscopy with advanced data analysis shed light on the distribution of a guest molecule (7,7,8,8-tetracyanoquinodimethane) at the intracrystal level.[433] These two studies show the importance of using spatially resolved tools as a routine when complex composites are built as reported in the latest strategies. Eventually, the use of these, together with more traditional bulk techniques in *operando* modes will result in an improved design of MOFs, rendering them suitable for large-scale or commercial applications (Fig. 21). We refer the reader to recent literature on this type of techniques to understand the potential of microscopy for understanding crystallization of MOFs.[420,463–465]

7. Conclusions and outlook

This review article provides an overview of the use of different advanced characterization tools in the field of metal–organic frameworks (MOFs) with their potential being illustrated by using well-known, robust topologies. Characteristic traits or phenomena related to MIL-100, MAF-4/ZIF-8 and HKUST-1 were highlighted with the main (nano/micro)-spectroscopy, diffraction and scattering techniques used to uncover their nature, emphasizing potential pitfalls and constraints. Although very different in their chemical and compositional nature, the MOF field could benefit from the tools used in the past for other functional porous materials, such as zeolites or porous metal oxides.

From our bibliometric analysis, it is clear that there is still plenty of room for advanced techniques, such as X-ray reflectivity (XRR), grazing incidence X-ray absorption spectroscopy (GIXAS) or electrical scanning probe microscopy techniques such as Kelvin probe force microscopy (KPFM) could provide critically relevant information on surface morphology, electronic structure or magnetic properties, respectively, of MOF surfaces. In addition, more spatially resolved studies are needed to uncover the underlying effects of atomic compositional heterogeneities, inter/intraparticle gradients and their effect on the chemistry of MOFs. They are inherently complex materials, with multiple components that can be present in different forms (*i.e.*, geometry, configurations and oxidation state). Several fundamental questions involving crystal heterogeneities (*e.g.* direct imaging of atomic scale mixing, chemical nature of defects, generality of metal exchange mechanisms, pore network permeability, surface energies) are still open. These issues remain a challenge for the characterization community, in which only a few selected electron microscopy studies and the use of AFM (mainly related to the synthesis of MOF thin-films) for specific SURMOFS, have been able to provide some insight. The advent of non-diffraction limited techniques, such as AFM-IR microspectroscopy, together with a more widespread use of *operando* studies (let it be catalysis, gas sorption or molecular separations), will take understanding of MOFs to the next step.

The ultimate level of fundamental understanding will be achieved by the combination of all these features, *i.e.* the development of characterization tools that can provide chemical information of these materials under dynamic conditions (*in situ* or *operando)* at the nano- (and eventually atomic) scale. As a result, we foresee that MOFs will be an excellent field for the development and adaptation of (new) micro- and nano-spectroscopic methods. The use and application of these techniques have the potential to benefit the MOF community greatly in the long term, and we expect they will play a pivotal role as they already do in *e.g.* the fields of biology and optoelectronics.

Conflicts of interest

There are no conflicts to declare.

Acknowledgements

This project has received funding from the European Union Horizon 2020 research and innovation program under the Marie Sklodowska-Curie grant agreement 641887 (DEFNET). B. S. gratefully acknowledges the Dutch National Science Foundation (NWO), The Netherlands, for her personal VENI grant 722.015.007. M. F. acknowledges the European Union's Horizon 2020 research and innovation program under the Marie Sklodowska-Curie grant agreement (No. 748563). This work is supported by a Netherlands Organization of Scientific Research (NWO) Gravitation program (Netherlands Center for Multiscale Catalytic Energy Conversion, MCEC).

References

1 Y.-S. Ho and H.-Z. Fu, *Inorg. Chem. Commun.*, 2016, **73**, 174–182.
2 C.-C. Wang and Y.-S. Ho, *Scientometrics*, 2016, **109**, 481–513.
3 B. F. Hoskins and R. Robson, *J. Am. Chem. Soc.*, 1990, **112**, 1546–1554.
4 S. R. Batten, B. F. Hoskins and R. Robson, *J. Am. Chem. Soc.*, 1995, **117**, 5385–5386.

Open Access Article. Published on 20 August 2020. Downloaded on 2/16/2026 6:59:12 AM.
This article is licensed under a Creative Commons Attribution 3.0 Unported Licence.

5 H. Li, M. Eddaoudi, M. O'Keeffe and O. M. Yaghi, *Nature*, 1999, **402**, 276–279.
6 C. Wiktor, M. Meledina, S. Turner, O. I. Lebedev and R. A. Fischer, *J. Mater. Chem. A*, 2017, **5**, 14969–14989.
7 C. Martineau-Corcos, *Curr. Opin. Colloid Interface Sci.*, 2018, **33**, 35–43.
8 B. E. G. Lucier, S. Chen and Y. Huang, *Acc. Chem. Res.*, 2018, **51**, 319–330.
9 P. He, B. E. G. Lucier, V. V. Terskikh, Q. Shi, J. Dong, Y. Chu, A. Zheng, A. Sutrisno and Y. Huang, *J. Phys. Chem. C*, 2014, **118**, 23728–23744.
10 Y. Huang, J. Xu, F. Gul-E-Noor and P. He, Metal–Organic Frameworks: NMR Studies of Quadrupolar Nuclei, in *Encyclopedia of Inorganic and Bioinorganic Chemistry*, ed. R. A. Scott, 2014, DOI: 10.1002/9781119951438.eibc2225.
11 A. Krajnc, T. Kos, N. Zabukovec Logar and G. Mali, *Angew. Chem., Int. Ed.*, 2015, **54**, 10535–10538.
12 M. Haouas, *Materials*, 2018, **11**(8), 1416.
13 M. A. Soldatov, A. Martini, A. L. Bugaev, I. Pankin, P. V. Medvedev, A. A. Guda, A. M. Aboraia, Y. S. Podkovyrina, A. P. Budnyk, A. A. Soldatov and C. Lamberti, *Polyhedron*, 2018, **155**, 232–253.
14 E. Borfecchia, L. Braglia, F. Bonino, S. Bordiga, S. Øien, U. Olsbye, K. P. Lillerud, J. A. van Bokhoven, K. A. Lomachenko, A. A. Guda, M. A. Soldatov and C. Lamberti, in *XAFS Techniques for Catalysts, Nanomaterials, and Surfaces*, ed. Y. Iwasawa, K. Asakura and M. Tada, Springer International Publishing, Cham, 2017, pp. 397–430, DOI: 10.1007/978-3-319-43866-5_26.
15 C. Garino, E. Borfecchia, R. Gobetto, J. A. van Bokhoven and C. Lamberti, *Coord. Chem. Rev.*, 2014, **277-278**, 130–186.
16 F. Bonino, C. Lamberti and S. Bordiga, *The Chemistry of Metal–Organic Frameworks: Synthesis, Characterization, and Applications*, Wiley-VCH Verlag GmbH & Co. KGaA, 2016, pp. 657–690, DOI: 10.1002/9783527693078.ch22.
17 F. Bonino, C. Lamberti, S. Chavan, J. G. Vitillo and S. Bordiga, *Metal Organic Frameworks as Heterogeneous Catalysts*, The Royal Society of Chemistry, 2013, pp. 76–142, DOI: 10.1039/9781849737586-00076.
18 A. J. Howarth, A. W. Peters, N. A. Vermeulen, T. C. Wang, J. T. Hupp and O. K. Farha, *Chem. Mater.*, 2017, **29**, 26–39.
19 S. Bordiga, F. Bonino, K. P. Lillerud and C. Lamberti, *Chem. Soc. Rev.*, 2010, **39**, 4885–4927.
20 H. C. Hoffmann, M. Debowski, P. Müller, S. Paasch, I. Senkovska, S. Kaskel and E. Brunner, *Materials*, 2012, **5**(12), 2537–2572.
21 A. Sutrisno, V. V. Terskikh, Q. Shi, Z. Song, J. Dong, S. Y. Ding, W. Wang, B. R. Provost, T. D. Daff, T. K. Woo and Y. Huang, *Chem. – Eur. J.*, 2012, **18**, 12251–12259.
22 A. J. Howarth, A. W. Peters, N. A. Vermeulen, T. C. Wang, J. T. Hupp and O. K. Farha, *Chem. Mater.*, 2017, **29**, 26–39.
23 T. L. Easun, F. Moreau, Y. Yan, S. Yang and M. Schroder, *Chem. Soc. Rev.*, 2017, **46**, 239–274.
24 M. J. Van Vleet, T. Weng, X. Li and J. R. Schmidt, *Chem. Rev.*, 2018, **118**, 3681–3721.
25 J.-R. Li, J. Sculley and H.-C. Zhou, *Chem. Rev.*, 2012, **112**, 869–932.
26 A. Schneemann, V. Bon, I. Schwedler, I. Senkovska, S. Kaskel and R. A. Fischer, *Chem. Soc. Rev.*, 2014, **43**, 6062–6096.
27 V. Kapko, C. Dawson, M. M. J. Treacy and M. F. Thorpe, *Phys. Chem. Chem. Phys.*, 2010, **12**, 8531–8541.
28 J. A. Mason, J. Oktawiec, M. K. Taylor, M. R. Hudson, J. Rodriguez, J. E. Bachman, M. I. Gonzalez, A. Cervellino, A. Guagliardi, C. M. Brown, P. L. Llewellyn, N. Masciocchi and J. R. Long, *Nature*, 2015, **527**, 357–361.
29 S. Horike, S. Shimomura and S. Kitagawa, *Nat. Chem.*, 2009, **1**, 695–704.
30 S. Kitagawa, R. Kitaura and S.-I. Noro, *Angew. Chem., Int. Ed.*, 2004, **43**, 2334–2375.
31 S. Bureekaew, S. Shimomura and S. Kitagawa, *Sci. Technol. Adv. Mater.*, 2008, **9**, 014108.
32 K. Uemura, R. Matsuda and S. Kitagawa, *J. Solid State Chem.*, 2005, **178**, 2420–2429.
33 S. Kitagawa and K. Uemura, *Chem. Soc. Rev.*, 2005, **34**, 109–119.
34 G. Ferey and C. Serre, *Chem. Soc. Rev.*, 2009, **38**, 1380–1399.
35 G. Férey, *Dalton Trans.*, 2009, 4400–4415, DOI: 10.1039/B817360P.
36 A. J. Fletcher, K. M. Thomas and M. J. Rosseinsky, *J. Solid State Chem.*, 2005, **178**, 2491–2510.
37 C. R. Murdock, B. C. Hughes, Z. Lu and D. M. Jenkins, *Coord. Chem. Rev.*, 2014, **258–259**, 119–136.
38 Z. Fang, B. Bueken, D. E. De Vos and R. A. Fischer, *Angew. Chem., Int. Ed.*, 2015, **54**, 7234–7254.
39 S. Dissegna, K. Epp, W. R. Heinz, G. Kieslich and R. A. Fischer, *Adv. Mater.*, 2018, **30**, 1704501.
40 M. Lalonde, W. Bury, O. Karagiaridi, Z. Brown, J. T. Hupp and O. K. Farha, *J. Mater. Chem. A*, 2013, **1**, 5453–5468.
41 P. Deria, J. E. Mondloch, O. Karagiaridi, W. Bury, J. T. Hupp and O. K. Farha, *Chem. Soc. Rev.*, 2014, **43**, 5896–5912.
42 J. D. Evans, C. J. Sumby and C. J. Doonan, *Chem. Soc. Rev.*, 2014, **43**, 5933–5951.
43 C. K. Brozek and M. Dinca, *Chem. Soc. Rev.*, 2014, **43**, 5456–5467.
44 S. Abednatanzi, P. Gohari Derakhshandeh, H. Depauw, F.-X. Coudert, H. Vrielinck, P. Van Der Voort and K. Leus, *Chem. Soc. Rev.*, 2019, **48**, 2535–2565.
45 T. D. Bennett, A. K. Cheetham, A. H. Fuchs and F.-X. Coudert, *Nat. Chem.*, 2017, **9**, 11–16.
46 T. D. Bennett, A. H. Fuchs, A. K. Cheetham and F.-X. Coudert, *Dalton Trans.*, 2016, **45**, 4058–4059.
47 T. D. Bennett and A. K. Cheetham, *Acc. Chem. Res.*, 2014, **47**, 1555–1562.
48 J. Hou, C. W. Ashling, S. M. Collins, A. Krajnc, C. Zhou, L. Longley, D. N. Johnstone, P. A. Chater, S. Li, M.-V. Coulet, P. L. Llewellyn, F.-X. Coudert, D. A. Keen, P. A. Midgley, G. Mali, V. Chen and T. D. Bennett, *Nat. Commun.*, 2019, **10**, 2580.
49 R. S. K. Madsen, A. Qiao, J. Sen, I. Hung, K. Chen, Z. Gan, S. Sen and Y. Yue, *Science*, 2020, **367**, 1473–1476.

This journal is © The Royal Society of Chemistry 2020

Open Access Article. Published on 20 August 2020. Downloaded on 2/16/2026 6:59:12 AM.
This article is licensed under a Creative Commons Attribution 3.0 Unported Licence.

50 J. Hou, M. L. Rios Gomez, A. Krajnc, A. McCaul, S. Li, A. M. Bumstead, A. F. Sapnik, Z. Deng, R. Lin, P. A. Chater, D. S. Keeble, D. A. Keen, D. Appadoo, B. Chan, V. Chen, G. Mali and T. D. Bennett, *J. Am. Chem. Soc.*, 2020, **142**, 3880–3890.
51 M. Rivera-Torrente, M. Filez, R. Hardian, E. Reynolds, B. Seoane, M.-V. Coulet, F. E. Oropeza Palacio, J. P. Hofmann, R. A. Fischer, A. L. Goodwin, P. L. Llewellyn and B. M. Weckhuysen, *Chem. – Eur. J.*, 2018, **24**, 7498–7506.
52 A. Corma, H. García and F. X. Llabrés i Xamena, *Chem. Rev.*, 2010, **110**, 4606–4655.
53 D. Yang and B. C. Gates, *ACS Catal.*, 2019, **9**, 1779–1798.
54 M. Filez, Z. Ristanović and B. M. Weckhuysen, in *Encyclopedia of Interfacial Chemistry*, ed. K. Wandelt, Elsevier, Oxford, 2018, pp. 304–320, DOI: 10.1016/b978-0-12-409547-2.13744-8.
55 F. Meirer and B. M. Weckhuysen, *Nat. Rev. Mater.*, 2018, **3**, 324–340.
56 A. M. Beale, S. D. M. Jacques and B. M. Weckhuysen, *Chem. Soc. Rev.*, 2010, **39**, 4656–4672.
57 G. Férey, C. Serre, C. Mellot-Draznieks, F. Millange, S. Surblé, J. Dutour and I. Margiolaki, *Angew. Chem., Int. Ed.*, 2004, **43**, 6296–6301.
58 G. Férey, C. Mellot-Draznieks, C. Serre, F. Millange, J. Dutour, S. Surblé and I. Margiolaki, *Science*, 2005, **309**, 2040–2042.
59 P. Horcajada, S. Surble, C. Serre, D.-Y. Hong, Y.-K. Seo, J.-S. Chang, J.-M. Greneche, I. Margiolaki and G. Ferey, *Chem. Commun.*, 2007, 2820–2822, DOI: 10.1039/B704325B.
60 C. Volkringer, D. Popov, T. Loiseau, G. R. Férey, M. Burghammer, C. Riekel, M. Haouas and F. Taulelle, *Chem. Mater.*, 2009, **21**, 5695–5697.
61 A. Lieb, H. Leclerc, T. Devic, C. Serre, I. Margiolaki, F. Mahjoubi, J. S. Lee, A. Vimont, M. Daturi and J.-S. Chang, *Microporous Mesoporous Mater.*, 2012, **157**, 18–23.
62 L. Mitchell, B. Gonzalez-Santiago, J. P. S. Mowat, M. E. Gunn, P. Williamson, N. Acerbi, M. L. Clarke and P. A. Wright, *Catal. Sci. Technol.*, 2013, **3**, 606–617.
63 J. A. Mason, L. E. Darago, W. W. Lukens and J. R. Long, *Inorg. Chem.*, 2015, **54**, 10096–10104.
64 J. Castells-Gil, N. M. Padial, N. Almora-Barrios, I. da Silva, D. Mateo, J. Albero, H. Garcia and C. Marti-Gastaldo, *Chem. Sci.*, 2019, **10**, 4313–4321.
65 H. Reinsch and N. Stock, *CrystEngComm*, 2013, **15**, 544–550.
66 F. Zhang, X. Zou, W. Feng, X. Zhao, X. Jing, F. Sun, H. Ren and G. Zhu, *J. Mater. Chem.*, 2012, **22**, 25019–25026.
67 S. Bhattacharjee, C. Chen and W.-S. Ahn, *RSC Adv.*, 2014, **4**, 52500–52525.
68 M. P. Attfield and P. Cubillas, *Dalton Trans.*, 2012, **41**, 3869–3878.
69 T. Ahnfeldt, J. Moellmer, V. Guillerm, R. Staudt, C. Serre and N. Stock, *Chem. – Eur. J.*, 2011, **17**, 6462–6468.
70 F. Millange, R. El Osta, M. E. Medina and R. I. Walton, *CrystEngComm*, 2011, **13**, 103–108.
71 F. Niekiel, M. Ackermann, P. Guerrier, A. Rothkirch and N. Stock, *Inorg. Chem.*, 2013, **52**, 8699–8705.
72 F. Ragon, H. Chevreau, T. Devic, C. Serre and P. Horcajada, *Chem. – Eur. J.*, 2015, **21**, 7135–7143.
73 Y. Wu, M. I. Breeze, G. J. Clarkson, F. Millange, D. O'Hare and R. I. Walton, *Angew. Chem., Int. Ed.*, 2016, **55**, 4992–4996.
74 F. Ragon, P. Horcajada, H. Chevreau, Y. K. Hwang, U. H. Lee, S. R. Miller, T. Devic, J.-S. Chang and C. Serre, *Inorg. Chem.*, 2014, **53**, 2491–2500.
75 F. Millange, M. I. Medina, N. Guillou, G. Férey, K. M. Golden and R. I. Walton, *Angew. Chem., Int. Ed.*, 2010, **49**, 763–766.
76 M. G. Goesten, F. Kapteijn and J. Gascon, *CrystEngComm*, 2013, **15**, 9249–9257.
77 M. Haouas, C. Volkringer, T. Loiseau, G. Férey and F. Taulelle, *Chem. Mater.*, 2012, **24**, 2462–2471.
78 G. Ferey, *Chem. Soc. Rev.*, 2008, **37**, 191–214.
79 T. Devic and C. Serre, *Chem. Soc. Rev.*, 2014, **43**, 6097–6115.
80 C. Serre, F. Millange, S. Surblé and G. Férey, *Angew. Chem., Int. Ed.*, 2004, **43**, 6285–6289.
81 P. Horcajada, H. Chevreau, D. Heurtaux, F. Benyettou, F. Salles, T. Devic, A. Garcia-Marquez, C. Yu, H. Lavrard, C. L. Dutson, E. Magnier, G. Maurin, E. Elkaim and C. Serre, *Chem. Commun.*, 2014, **50**, 6872–6874.
82 S. Surble, C. Serre, C. Mellot-Draznieks, F. Millange and G. Ferey, *Chem. Commun.*, 2006, 284–286, DOI: 10.1039/B512169H.
83 S. Surble, F. Millange, C. Serre, G. Ferey and R. I. Walton, *Chem. Commun.*, 2006, 1518–1520, DOI: 10.1039/B600709K.
84 W. Xuan, C. Zhu, Y. Liu and Y. Cui, *Chem. Soc. Rev.*, 2012, **41**, 1677–1695.
85 M. G. Goesten, E. Stavitski, J. Juan-Alcañiz, A. Martiñez-Joaristi, A. V. Petukhov, F. Kapteijn and J. Gascon, *Catal. Today*, 2013, **205**, 120–127.
86 N. Pienack and W. Bensch, *Angew. Chem., Int. Ed.*, 2011, **50**, 2014–2034.
87 T. Birsa Čelič, M. Rangus, K. Lázár, V. Kaučič and N. Zabukovec Logar, *Angew. Chem., Int. Ed.*, 2012, **51**, 12490–12494.
88 E. Stavitski, M. Goesten, J. Juan-Alcañiz, A. Martinez-Joaristi, P. Serra-Crespo, A. V. Petukhov, J. Gascon and F. Kapteijn, *Angew. Chem., Int. Ed.*, 2011, **50**, 9624–9628.
89 A. C. Sudik, A. P. Côté and O. M. Yaghi, *Inorg. Chem.*, 2005, **44**, 2998–3000.
90 M. G. Goesten, P. C. M. M. Magusin, E. A. Pidko, B. Mezari, E. J. M. Hensen, F. Kapteijn and J. Gascon, *Inorg. Chem.*, 2014, **53**, 882–887.
91 G. Férey, M. Haouas, T. Loiseau and F. Taulelle, *Chem. Mater.*, 2014, **26**, 299–309.
92 X. Yang and A. E. Clark, *Inorg. Chem.*, 2014, **53**, 8930–8940.
93 R. I. Walton and F. Millange, *The Chemistry of Metal–Organic Frameworks: Synthesis, Characterization, and Applications*, Wiley-VCH Verlag GmbH & Co. KGaA, 2016, pp. 729–764, DOI: 10.1002/9783527693078.ch24.
94 Y. Wu, M. I. Breeze, D. O'Hare and R. I. Walton, *Microporous Mesoporous Mater.*, 2017, **254**, 178–183.

Open Access Article. Published on 20 August 2020. Downloaded on 2/16/2026 6:59:12 AM.
This article is licensed under a Creative Commons Attribution 3.0 Unported Licence.

95 A. M. Beale, A. M. J. van der Eerden, S. D. M. Jacques, O. Leynaud, M. G. O'Brien, F. Meneau, S. Nikitenko, W. Bras and B. M. Weckhuysen, *J. Am. Chem. Soc.*, 2006, **128**, 12386–12387.
96 M. G. O'Brien, A. M. Beale and B. M. Weckhuysen, *Chem. Soc. Rev.*, 2010, **39**, 4767–4782.
97 D. Grandjean, A. M. Beale, A. V. Petukhov and B. M. Weckhuysen, *J. Am. Chem. Soc.*, 2005, **127**, 14454–14465.
98 P. L. Llewellyn, S. Bourrelly, C. Serre, A. Vimont, M. Daturi, L. Hamon, G. De Weireld, J.-S. Chang, D.-Y. Hong, Y. Kyu Hwang, S. Hwa Jhung and G. Férey, *Langmuir*, 2008, **24**, 7245–7250.
99 A. Vimont, J.-M. Goupil, J.-C. Lavalley, M. Daturi, S. Surblé, C. Serre, F. Millange, G. Férey and N. Audebrand, *J. Am. Chem. Soc.*, 2006, **128**, 3218–3227.
100 H. Leclerc, A. Vimont, J.-C. Lavalley, M. Daturi, A. D. Wiersum, P. L. Llwellyn, P. Horcajada, G. Ferey and C. Serre, *Phys. Chem. Chem. Phys.*, 2011, **13**, 11748–11756.
101 M. Haouas, C. Volkringer, T. Loiseau, G. Férey and F. Taulelle, *J. Phys. Chem. C*, 2011, **115**, 17934–17944.
102 C. Volkringer, H. Leclerc, J.-C. Lavalley, T. Loiseau, G. Férey, M. Daturi and A. Vimont, *J. Phys. Chem. C*, 2012, **116**, 5710–5719.
103 J. Jiang and O. M. Yaghi, *Chem. Rev.*, 2015, **115**, 6966–6997.
104 A. Vimont, H. Leclerc, F. Maugé, M. Daturi, J.-C. Lavalley, S. Surblé, C. Serre and G. Férey, *J. Phys. Chem. C*, 2007, **111**, 383–388.
105 J. N. Hall and P. Bollini, *ACS Catal.*, 2020, **10**, 3750–3763.
106 J. Hajek, C. Caratelli, R. Demuynck, K. De Wispelaere, L. Vanduyfhuys, M. Waroquier and V. Van Speybroeck, *Chem. Sci.*, 2018, **9**, 2723–2732.
107 H. Furukawa, K. E. Cordova, M. O'Keeffe and O. M. Yaghi, *Science*, 2013, **341**, 1230444.
108 R. Wei, C. A. Gaggioli, G. Li, T. Islamoglu, Z. Zhang, P. Yu, O. K. Farha, C. J. Cramer, L. Gagliardi, D. Yang and B. C. Gates, *Chem. Mater.*, 2019, **31**, 1655–1663.
109 X. Feng, J. Hajek, H. S. Jena, G. Wang, S. K. P. Veerapandian, R. Morent, N. De Geyter, K. Leyssens, A. E. J. Hoffman, V. Meynen, C. Marquez, D. E. De Vos, V. Van Speybroeck, K. Leus and P. Van Der Voort, *J. Am. Chem. Soc.*, 2020, **142**, 3174–3183.
110 C. Caratelli, J. Hajek, F. G. Cirujano, M. Waroquier, F. X. Llabrés i Xamena and V. Van Speybroeck, *J. Catal.*, 2017, **352**, 401–414.
111 M. Taddei, *Coord. Chem. Rev.*, 2017, **343**, 1–24.
112 S. Wuttke, P. Bazin, A. Vimont, C. Serre, Y.-K. Seo, Y. K. Hwang, J.-S. Chang, G. Férey and M. Daturi, *Chem. – Eur. J.*, 2012, **18**, 11959–11967.
113 G. Gómez-Pozuelo, C. P. Cabello, M. Opanasenko, M. Horáček and J. Čejka, *ChemPlusChem*, 2016, **82**, 152–159.
114 S. Mitchell, A. B. Pinar, J. Kenvin, P. Crivelli, J. Karger and J. Perez-Ramirez, *Nat. Commun.*, 2015, **6**, 8633.
115 K. W. Chapman, G. J. Halder and P. J. Chupas, *J. Am. Chem. Soc.*, 2009, **131**, 17546–17547.
116 J. W. Yoon, Y.-K. Seo, Y. K. Hwang, J.-S. Chang, H. Leclerc, S. Wuttke, P. Bazin, A. Vimont, M. Daturi, E. Bloch, P. L. Llewellyn, C. Serre, P. Horcajada, J.-M. Grenèche, A. E. Rodrigues and G. Férey, *Angew. Chem., Int. Ed.*, 2010, **49**, 5949–5952.
117 G. T. Palomino, C. P. Cabello and C. O. Areán, *Eur. J. Inorg. Chem.*, 2011, 1703–1708.
118 R. Giovine, C. Volkringer, S. E. Ashbrook, J. Trébosc, D. McKay, T. Loiseau, J.-P. Amoureux, O. Lafon and F. Pourpoint, *Chem. – Eur. J.*, 2017, **23**, 9525–9534.
119 B. Barth, M. Mendt, A. Pöppl and M. Hartmann, *Microporous Mesoporous Mater.*, 2015, **216**, 97–110.
120 M. Mendt, B. Barth, M. Hartmann and A. Pöppl, *J. Chem. Phys.*, 2017, **147**, 224701.
121 A. H. Khan, B. Barth, M. Hartmann, J. Haase and M. Bertmer, *J. Phys. Chem. C*, 2018, **122**, 12723–12730.
122 A. E. Khudozhitkov, A. V. Toktarev, S. S. Arzumanov, A. A. Gabrienko, D. I. Kolokolov and A. G. Stepanov, *Chem. – Eur. J.*, 2019, **25**, 10808–10812.
123 A. E. Khudozhitkov, S. S. Arzumanov, D. I. Kolokolov, O. A. Kholdeeva, D. Freude and A. G. Stepanov, *Chem.*, 2019, **25**, 5163–5168.
124 A. Nandy, A. C. Forse, V. J. Witherspoon and J. A. Reimer, *J. Phys. Chem. C*, 2018, **122**, 8295–8305.
125 C. Zhao, H. Meng, M. Nie, L. Jiang, C. Wang and T. Wang, *J. Phys. Chem. C*, 2018, **122**, 4635–4640.
126 A. M. Sheveleva, A. V. Anikeenko, A. S. Poryvaev, D. L. Kuzmina, I. K. Shundrina, D. I. Kolokolov, A. G. Stepanov and M. V. Fedin, *J. Phys. Chem. C*, 2017, **121**, 19880–19886.
127 T. Wittmann, A. Mondal, C. B. L. Tschense, J. J. Wittmann, O. Klimm, R. Siegel, B. Corzilius, B. Weber, M. Kaupp and J. Senker, *J. Am. Chem. Soc.*, 2018, **140**, 2135–2144.
128 S. Hinokuma, G. Wiker, T. Suganuma, A. Bansode, D. Stoian, S. C. Huertas, S. Molina, A. Shafir, M. Rønning, W. van Beek and A. Urakawa, *Eur. J. Inorg. Chem.*, 2018, 1847–1853.
129 M. Rivera-Torrente, C. Hernández Mejía, T. Hartman, K. P. de Jong and B. M. Weckhuysen, *Catal. Lett.*, 2019, **149**, 3279–3286.
130 M. Rivera-Torrente, P. D. Pletcher, M. K. Jongkind, N. Nikolopoulos and B. M. Weckhuysen, *ACS Catal.*, 2019, **9**, 3059–3069.
131 Y.-Q. Tian, C.-X. Cai, Y. Ji, X.-Z. You, S.-M. Peng and G.-H. Lee, *Angew. Chem., Int. Ed.*, 2002, **41**, 1384–1386.
132 X. Huang, J. Zhang and X. Chen, *Chin. Sci. Bull.*, 2013, **48**, 1531–1534.
133 N. Masciocchi, S. Bruni, E. Cariati, F. Cariati, S. Galli and A. Sironi, *Inorg. Chem.*, 2001, **40**, 5897–5905.
134 X.-C. Huang, Y.-Y. Lin, J.-P. Zhang and X.-M. Chen, *Angew. Chem., Int. Ed.*, 2006, **45**, 1557–1559.
135 Y.-Q. Tian, C.-X. Cai, X.-M. Ren, C.-Y. Duan, Y. Xu, S. Gao and X.-Z. You, *Chem. – Eur. J.*, 2003, **9**, 5673–5685.
136 Y.-Q. Tian, Z.-X. Chen, L.-H. Weng, H.-B. Guo, S. Gao and D. Y. Zhao, *Inorg. Chem.*, 2004, **43**, 4631–4635.
137 J.-P. Zhang, Y.-B. Zhang, J.-B. Lin and X.-M. Chen, *Chem. Rev.*, 2012, **112**, 1001–1033.
138 A. Phan, C. J. Doonan, F. J. Uribe-Romo, C. B. Knobler, M. O'Keeffe and O. M. Yaghi, *Acc. Chem. Res.*, 2010, **43**, 58–67.

 This journal is © The Royal Society of Chemistry 2020

Open Access Article. Published on 20 August 2020. Downloaded on 2/16/2026 6:59:12 AM. This article is licensed under a Creative Commons Attribution 3.0 Unported Licence.

139 K. S. Park, Z. Ni, A. P. Côté, J. Y. Choi, R. Huang, F. J. Uribe-Romo, H. K. Chae, M. O'Keeffe and O. M. Yaghi, *Proc. Natl. Acad. Sci. U. S. A.*, 2006, **103**, 10186–10191.
140 Y. Pan, Y. Liu, G. Zeng, L. Zhao and Z. Lai, *Chem. Commun.*, 2011, **47**, 2071–2073.
141 J. Cravillon, S. Münzer, S.-J. Lohmeier, A. Feldhoff, K. Huber and M. Wiebcke, *Chem. Mater.*, 2009, **21**, 1410–1412.
142 H. Reinsch, *Eur. J. Inorg. Chem.*, 2016, 4290–4299.
143 S. Bhattacharjee, M.-S. Jang, H.-J. Kwon and W.-S. Ahn, *Catal. Surv. Asia*, 2014, **18**, 101–127.
144 Y.-R. Lee, J. Kim and W.-S. Ahn, *Korean J. Chem. Eng.*, 2013, **30**, 1667–1680.
145 B. R. Pimentel, A. Parulkar, E.-K. Zhou, N. A. Brunelli and R. P. Lively, *ChemSusChem*, 2014, **7**, 3202–3240.
146 J. Cravillon, R. Nayuk, S. Springer, A. Feldhoff, K. Huber and M. Wiebcke, *Chem. Mater.*, 2011, **23**, 2130–2141.
147 S. Tanaka, K. Kida, M. Okita, Y. Ito and Y. Miyake, *Chem. Lett.*, 2012, **41**, 1337–1339.
148 J. Cravillon, C. A. Schröder, H. Bux, A. Rothkirch, J. Caro and M. Wiebcke, *CrystEngComm*, 2012, **14**, 492–498.
149 M. Goesten, E. Stavitski, E. A. Pidko, C. Gücüyener, B. Boshuizen, S. N. Ehrlich, E. J. M. Hensen, F. Kapteijn and J. Gascon, *Chem. – Eur. J.*, 2013, **19**, 7809–7816.
150 L. Batzdorf, F. Fischer, M. Wilke, K.-J. Wenzel and F. Emmerling, *Angew. Chem., Int. Ed.*, 2015, **54**, 1799–1802.
151 C. A. Schröder, I. A. Baburin, L. van Wüllen, M. Wiebcke and S. Leoni, *CrystEngComm*, 2013, **15**, 4036–4040.
152 T. Friščić, I. Halasz, P. J. Beldon, A. M. Belenguer, F. Adams, S. A. J. Kimber, V. Honkimäki and R. E. Dinnebier, *Nat. Chem.*, 2013, **5**, 66–73.
153 I. Halasz, S. A. J. Kimber, P. J. Beldon, A. M. Belenguer, F. Adams, V. Honkimäki, R. C. Nightingale, R. E. Dinnebier and T. Friščić, *Nat. Protoc.*, 2013, **8**, 1718–1729.
154 I. Halasz, T. Friscic, S. A. J. Kimber, K. Uzarevic, A. Puskaric, C. Mottillo, P. Julien, V. Strukil, V. Honkimaki and R. E. Dinnebier, *Faraday Discuss.*, 2014, **170**, 203–221.
155 I. H. Lim, W. Schrader and F. Schüth, *Chem. Mater.*, 2015, **27**, 3088–3095.
156 J. P. Patterson, P. Abellan, M. S. Denny, C. Park, N. D. Browning, S. M. Cohen, J. E. Evans and N. C. Gianneschi, *J. Am. Chem. Soc.*, 2015, **137**, 7322–7328.
157 J. Cravillon, C. A. Schröder, R. Nayuk, J. Gummel, K. Huber and M. Wiebcke, *Angew. Chem., Int. Ed.*, 2011, **50**, 8067–8071.
158 P. Y. Moh, P. Cubillas, M. W. Anderson and M. P. Attfield, *J. Am. Chem. Soc.*, 2011, **133**, 13304–13307.
159 B. Seoane, S. Castellanos, A. Dikhtiarenko, F. Kapteijn and J. Gascon, *Coord. Chem. Rev.*, 2016, **307**(Part 2), 147–187.
160 P. Cubillas, M. W. Anderson and M. P. Attfield, *Chem. – Eur. J.*, 2013, **19**, 8236–8243.
161 M. Shöâeè, J. R. Agger, M. W. Anderson and M. P. Attfield, *CrystEngComm*, 2008, **10**, 646–648.
162 M. Shoaee, M. W. Anderson and M. P. Attfield, *Angew. Chem., Int. Ed.*, 2008, **47**, 8525–8528.
163 N. S. John, C. Scherb, M. Shoaee, M. W. Anderson, M. P. Attfield and T. Bein, *Chem. Commun.*, 2009, 6294–6296, DOI: 10.1039/B908299A.
164 P. Cubillas, K. Etherington, M. W. Anderson and M. P. Attfield, *CrystEngComm*, 2014, **16**, 9834–9841.
165 P. Cubillas, M. W. Anderson and M. P. Attfield, *Cryst. Growth Des.*, 2013, **13**, 4526–4532.
166 P. Cubillas, M. W. Anderson and M. P. Attfield, *Chem. – Eur. J.*, 2012, **18**, 15406–15415.
167 T. L. Easun, F. Moreau, Y. Yan, S. H. Yang and M. Schroder, *Chem. Soc. Rev.*, 2017, **46**, 239–274.
168 C. L. Hobday, C. H. Woodall, M. J. Lennox, M. Frost, K. Kamenev, T. Düren, C. A. Morrison and S. A. Moggach, *Nat. Commun.*, 2018, **9**, 1429.
169 V. K. Peterson, Y. Liu, C. M. Brown and C. J. Kepert, *J. Am. Chem. Soc.*, 2006, **128**, 15578–15579.
170 T. Yildirim and M. R. Hartman, *Phys. Rev. Lett.*, 2005, **95**, 215504.
171 M. R. Hartman, V. K. Peterson, Y. Liu, S. S. Kaye and J. R. Long, *Chem. Mater.*, 2006, **18**, 3221–3224.
172 J. Getzschmann, I. Senkovska, D. Wallacher, M. Tovar, D. Fairen-Jimenez, T. Düren, J. M. van Baten, R. Krishna and S. Kaskel, *Microporous Mesoporous Mater.*, 2010, **136**, 50–58.
173 Y. Zhao, H. Xu, L. L. Daemen, K. Lokshin, K. T. Tait, W. L. Mao, J. Luo, R. P. Currier and D. D. Hickmott, *Proc. Natl. Acad. Sci. U. S. A.*, 2007, **104**, 5727–5731.
174 X. Lin, I. Telepeni, A. J. Blake, A. Dailly, C. M. Brown, J. M. Simmons, M. Zoppi, G. S. Walker, K. M. Thomas, T. J. Mays, P. Hubberstey, N. R. Champness and M. Schröder, *J. Am. Chem. Soc.*, 2009, **131**, 2159–2171.
175 M. Barter, J. Hartley, F.-J. Yazigi, R. J. Marshall, R. S. Forgan, A. Porch and M. O. Jones, *Phys. Chem. Chem. Phys.*, 2018, **20**, 10460–10469.
176 H. Wu, W. Zhou and T. Yildirim, *J. Am. Chem. Soc.*, 2007, **129**, 5314–5315.
177 H. Wu, W. Zhou and T. Yildirim, *J. Phys. Chem. C*, 2009, **113**, 3029–3035.
178 M. E. Casco, Y. Q. Cheng, L. L. Daemen, D. Fairen-Jimenez, E. V. Ramos-Fernandez, A. J. Ramirez-Cuesta and J. Silvestre-Albero, *Chem. Commun.*, 2016, **52**, 3639–3642.
179 C. Chmelik and J. Karger, *Chem. Soc. Rev.*, 2010, **39**, 4864–4884.
180 J. Kärger and D. Freude, *Chem. Eng. Technol.*, 2002, **25**, 769–778.
181 N. Rosenbach, H. Jobic, A. Ghoufi, F. Salles, G. Maurin, S. Bourrelly, P. L. Llewellyn, T. Devic, C. Serre and G. Férey, *Angew. Chem., Int. Ed.*, 2008, **47**, 6611–6615.
182 Q. Yang, A. D. Wiersum, H. Jobic, V. Guillerm, C. Serre, P. L. Llewellyn and G. Maurin, *J. Phys. Chem. C*, 2011, **115**, 13768–13774.
183 F. Salles, D. I. Kolokolov, H. Jobic, G. Maurin, P. L. Llewellyn, T. Devic, C. Serre and G. Ferey, *J. Phys. Chem. C*, 2009, **113**, 7802–7812.
184 F. Salles, H. Jobic, A. Ghoufi, P. L. Llewellyn, C. Serre, S. Bourrelly, G. Férey and G. Maurin, *Angew. Chem.*, 2009, **121**, 8485–8489.
185 F. Salles, H. Jobic, T. Devic, P. L. Llewellyn, C. Serre, G. Férey and G. Maurin, *ACS Nano*, 2010, **4**, 143–152.

Open Access Article. Published on 20 August 2020. Downloaded on 2/16/2026 6:59:12 AM. This article is licensed under a Creative Commons Attribution 3.0 Unported Licence.

186 D. I. Kolokolov, H. Jobic, A. G. Stepanov, J. Ollivier, S. Rives, G. Maurin, T. Devic, C. Serre and G. Férey, *J. Phys. Chem. C*, 2012, **116**, 15093–15098.
187 S. Rives, H. Jobic, F. Ragon, T. Devic, C. Serre, G. Férey, J. Ollivier and G. Maurin, *Microporous Mesoporous Mater.*, 2012, **164**, 259–265.
188 H. Jobic and D. N. Theodorou, *Microporous Mesoporous Mater.*, 2007, **102**, 21–50.
189 Y. Liu, C. M. Brown, D. A. Neumann, V. K. Peterson and C. J. Kepert, *J. Alloys Compd.*, 2007, **446–447**, 385–388.
190 Q. Yang, H. Jobic, F. Salles, D. Kolokolov, V. Guillerm, C. Serre and G. Maurin, *Chem. – Eur. J.*, 2011, **17**, 8882–8889.
191 E. Pantatosaki, H. Jobic, D. I. Kolokolov, S. Karmakar, R. Biniwale and G. K. Papadopoulos, *J. Chem. Phys.*, 2013, **138**, 034706.
192 H. Jobic, D. I. Kolokolov, A. G. Stepanov, M. M. Koza and J. Ollivier, *J. Phys. Chem. C*, 2015, **119**, 16115–16120.
193 H. Jobic, *Phys. Chem. Chem. Phys.*, 2016, **18**, 17190–17195.
194 K. Sumida, J.-H. Her, M. Dincă, L. J. Murray, J. M. Schloss, C. J. Pierce, B. A. Thompson, S. A. FitzGerald, C. M. Brown and J. R. Long, *J. Phys. Chem. C*, 2011, **115**, 8414–8421.
195 K. Sumida, C. M. Brown, Z. R. Herm, S. Chavan, S. Bordiga and J. R. Long, *Chem. Commun.*, 2011, **47**, 1157–1159.
196 S. Yang, A. J. Ramirez-Cuesta, R. Newby, V. Garcia-Sakai, P. Manuel, S. K. Callear, S. I. Campbell, C. C. Tang and M. Schröder, *Nat. Chem.*, 2015, **7**, 121–129.
197 N. A. Ramsahye, J. Gao, H. Jobic, P. L. Llewellyn, Q. Yang, A. D. Wiersum, M. M. Koza, V. Guillerm, C. Serre, C. L. Zhong and G. Maurin, *J. Phys. Chem. C*, 2014, **118**, 27470–27482.
198 M. E. Casco, F. Rey, J. L. Jordá, S. Rudić, F. Fauth, M. Martínez-Escandell, F. Rodríguez-Reinoso, E. V. Ramos-Fernández and J. Silvestre-Albero, *Chem. Sci.*, 2016, **7**, 3658–3666.
199 F. Stallmach, S. Gröger, V. Künzel, J. Kärger, O. M. Yaghi, M. Hesse and U. Müller, *Angew. Chem., Int. Ed.*, 2006, **45**, 2123–2126.
200 J. A. Gee, J. Chung, S. Nair and D. S. Sholl, *J. Phys. Chem. C*, 2013, **117**, 3169–3176.
201 S. Hertel, M. Wehring, S. Amirjalayer, M. Gratz, J. Lincke, H. Krautscheid, R. Schmid and F. Stallmach, *Eur. Phys. J.: Appl. Phys.*, 2011, **55**, 20702.
202 S. Schlayer, A.-K. Pusch, F. Pielenz, S. Beckert, M. Peksa, C. Horch, L. Moschkowitz, W.-D. Einicke and F. Stallmach, *Materials*, 2012, **5**(4), 617–633.
203 A.-K. Pusch, T. Splith, L. Moschkowitz, S. Karmakar, R. Biniwale, M. Sant, G. B. Suffritti, P. Demontis, J. Cravillon, E. Pantatosaki and F. Stallmach, *Adsorption*, 2012, **18**, 359–366.
204 C. Chmelik, D. Freude, H. Bux and J. Haase, *Microporous Mesoporous Mater.*, 2012, **147**, 135–141.
205 M. Wehring, J. Gascon, D. Dubbeldam, F. Kapteijn, R. Q. Snurr and F. Stallmach, *J. Phys. Chem. C*, 2010, **114**, 10527–10534.
206 F. Stallmach, A.-K. Pusch, T. Splith, C. Horch and S. Merker, *Microporous Mesoporous Mater.*, 2015, **205**, 36–39.
207 K. Díaz, L. Garrido, M. López-González, L. F. del Castillo and E. Riande, *Macromolecules*, 2010, **43**, 316–325.
208 P. V. Kortunov, L. Heinke, M. Arnold, Y. Nedellec, D. J. Jones, J. Caro and J. Kärger, *J. Am. Chem. Soc.*, 2007, **129**, 8041–8047.
209 C. Chmelik, J. Kärger, M. Wiebcke, J. Caro, J. M. van Baten and R. Krishna, *Microporous Mesoporous Mater.*, 2009, **117**, 22–32.
210 C. Chmelik, F. Hibbe, D. Tzoulaki, L. Heinke, J. Caro, J. Li and J. Kärger, *Microporous Mesoporous Mater.*, 2010, **129**, 340–344.
211 H. Bux, C. Chmelik, J. M. van Baten, R. Krishna and J. Caro, *Adv. Mater.*, 2010, **22**, 4741–4743.
212 C. Chmelik, J. van Baten and R. Krishna, *J. Membr. Sci.*, 2012, **397–398**, 87–91.
213 H. Bux, C. Chmelik, R. Krishna and J. Caro, *J. Membr. Sci.*, 2011, **369**, 284–289.
214 L. Hertäg, H. Bux, J. Caro, C. Chmelik, T. Remsungnen, M. Knauth and S. Fritzsche, *J. Membr. Sci.*, 2011, **377**, 36–41.
215 C. Chmelik, H. Bux, J. Caro, L. Heinke, F. Hibbe, T. Titze and J. Kärger, *Phys. Rev. Lett.*, 2010, **104**, 085902.
216 J. Karger, T. Binder, C. Chmelik, F. Hibbe, H. Krautscheid, R. Krishna and J. Weitkamp, *Nat. Mater.*, 2014, **13**, 333–343.
217 D. S. Sholl, *Nat. Chem.*, 2011, **3**, 429–430.
218 D. Tzoulaki, L. Heinke, H. Lim, J. Li, D. Olson, J. Caro, R. Krishna, C. Chmelik and J. Kärger, *Angew. Chem., Int. Ed.*, 2009, **48**, 3525–3528.
219 C. Chmelik, L. Heinke, P. Kortunov, J. Li, D. Olson, D. Tzoulaki, J. Weitkamp and J. Kärger, *ChemPhysChem*, 2009, **10**, 2623–2627.
220 L. Heinke and J. Kärger, *Phys. Rev. Lett.*, 2011, **106**, 074501.
221 F. Hibbe, C. Chmelik, L. Heinke, S. Pramanik, J. Li, D. M. Ruthven, D. Tzoulaki and J. Kärger, *J. Am. Chem. Soc.*, 2011, **133**, 2804–2807.
222 H. Jobic, J. Kärger and M. Bée, *Phys. Rev. Lett.*, 1999, **82**, 4260–4263.
223 E. Pantatosaki, G. Megariotis, A.-K. Pusch, C. Chmelik, F. Stallmach and G. K. Papadopoulos, *J. Phys. Chem. C*, 2012, **116**, 201–207.
224 L. Zhang, G. Wu and J. Jiang, *J. Phys. Chem. C*, 2014, **118**, 8788–8794.
225 X. Wu, J. Huang, W. Cai and M. Jaroniec, *RSC Adv.*, 2014, **4**, 16503–16511.
226 D. I. Kolokolov, A. G. Maryasov, J. Ollivier, D. Freude, J. Haase, A. G. Stepanov and H. Jobic, *J. Phys. Chem. C*, 2017, **121**, 2844–2857.
227 S. Pili, S. P. Argent, C. G. Morris, P. Rought, V. García-Sakai, I. P. Silverwood, T. L. Easun, M. Li, M. R. Warren, C. A. Murray, C. C. Tang, S. Yang and M. Schröder, *J. Am. Chem. Soc.*, 2016, **138**, 6352–6355.
228 D. D. Borges, S. Devautour-Vinot, H. Jobic, J. Ollivier, F. Nouar, R. Semino, T. Devic, C. Serre, F. Paesani and G. Maurin, *Angew. Chem., Int. Ed.*, 2016, **55**, 3919–3924.
229 T. Splith, E. Pantatosaki, P. D. Kolokathis, D. Fröhlich, K. Zhang, G. Füldner, C. Chmelik, J. Jiang, S. K. Henninger, F. Stallmach and G. K. Papadopoulos, *J. Phys. Chem. C*, 2017, **121**, 18065–18074.

 This journal is © The Royal Society of Chemistry 2020

Open Access Article. Published on 20 August 2020. Downloaded on 2/16/2026 6:59:12 AM.
This article is licensed under a Creative Commons Attribution 3.0 Unported Licence.

230 J. Ethiraj, F. Bonino, C. Lamberti and S. Bordiga, *Microporous Mesoporous Mater.*, 2015, **207**, 90–94.
231 A. Dutta, N. Tymińska, G. Zhu, J. Collins, R. P. Lively, J. R. Schmidt and S. Vasenkov, *J. Phys. Chem. C*, 2018, **122**, 7278–7287.
232 C. Chizallet, S. Lazare, D. Bazer-Bachi, F. Bonnier, V. Lecocq, E. Soyer, A.-A. Quoineaud and N. Bats, *J. Am. Chem. Soc.*, 2010, **132**, 12365–12377.
233 C. Chizallet and N. Bats, *J. Phys. Chem. Lett.*, 2010, **1**, 349–353.
234 A. V. Kubarev and M. B. J. Roeffaers, *CrystEngComm*, 2017, **19**, 4162–4165.
235 N. Dvoyashkina, D. Freude, S. S. Arzumanov and A. G. Stepanov, *J. Phys. Chem. C*, 2017, **121**, 25372–25376.
236 T. G. Grissom, C. H. Sharp, P. M. Usov, D. Troya, A. J. Morris and J. R. Morris, *J. Phys. Chem. C*, 2018, **122**, 16060–16069.
237 S. Berens, C. Chmelik, F. Hillman, J. Kärger, H.-K. Jeong and S. Vasenkov, *Phys. Chem. Chem. Phys.*, 2018, **20**, 23967–23975.
238 S. S. Y. Chui, S. M. F. Lo, J. P. H. Charmant, A. G. Orpen and I. D. Williams, *Science*, 1999, **283**, 1148–1150.
239 D. J. Tranchemontagne, J. R. Hunt and O. M. Yaghi, *Tetrahedron*, 2008, **64**, 8553–8557.
240 S. P. Gavrish and Y. D. Lampeka, *Theor. Exp. Chem.*, 2013, **49**, 130–134.
241 Z. G.-S. F. Qian-Rong, X. Ming-Hong, Z. Da-Liang, S. Xin, W. Gang, T. Ge, T. Lu-Lu, X. Ming and Q. Shi-Lun, *Chem. J. Chin. Univ.*, 2004, **25**, 1016–1018.
242 M. Kramer, U. Schwarz and S. Kaskel, *J. Mater. Chem.*, 2006, **16**, 2245–2248.
243 O. Kozachuk, K. Yusenko, H. Noei, Y. Wang, S. Walleck, T. Glaser and R. A. Fischer, *Chem. Commun.*, 2011, **47**, 8509–8511.
244 P. Maniam and N. Stock, *Inorg. Chem.*, 2011, **50**, 5085–5097.
245 C. R. Wade and M. Dinca, *Dalton Trans.*, 2012, **41**, 7931–7938.
246 L. Xie, S. Liu, C. Gao, R. Cao, J. Cao, C. Sun and Z. Su, *Inorg. Chem.*, 2007, **46**, 7782–7788.
247 O. Kozachuk, I. Luz, F. X. Llabrés i Xamena, H. Noei, M. Kauer, H. B. Albada, E. D. Bloch, B. Marler, Y. Wang, M. Muhler and R. A. Fischer, *Angew. Chem., Int. Ed.*, 2014, **53**, 7058–7062.
248 C. H. Hendon and A. Walsh, *Chem. Sci.*, 2015, **6**, 3674–3683.
249 Z. Fang, J. P. Dürholt, M. Kauer, W. Zhang, C. Lochenie, B. Jee, B. Albada, N. Metzler-Nolte, A. Pöppl, B. Weber, M. Muhler, Y. Wang, R. Schmid and R. A. Fischer, *J. Am. Chem. Soc.*, 2014, **136**, 9627–9636.
250 R. Ameloot, F. Vermoortele, J. Hofkens, F. C. De Schryver, D. E. De Vos and M. B. J. Roeffaers, *Angew. Chem., Int. Ed.*, 2013, **52**, 401–405.
251 I. Senkovska and V. Bon, *The Chemistry of Metal–Organic Frameworks: Synthesis, Characterization, and Applications*, Wiley-VCH Verlag GmbH & Co. KGaA, 2016, pp. 691–727, DOI: 10.1002/9783527693078.ch23.
252 M. Mendt, M. Šimėnas and A. Pöppl, *The Chemistry of Metal–Organic Frameworks: Synthesis, Characterization, and Applications*, Wiley-VCH Verlag GmbH & Co. KGaA, 2016, pp. 629–656, DOI: 10.1002/9783527693078.ch21.
253 E. Borfecchia, D. Gianolio, G. Agostini, S. Bordiga and C. Lamberti, *Metal Organic Frameworks as Heterogeneous Catalysts*, The Royal Society of Chemistry, 2013, pp. 143–208, DOI: 10.1039/9781849737586-00143.
254 C. Prestipino, L. Regli, J. G. Vitillo, F. Bonino, A. Damin, C. Lamberti, A. Zecchina, P. L. Solari, K. O. Kongshaug and S. Bordiga, *Chem. Mater.*, 2006, **18**, 1337–1346.
255 K.-S. Lin, A. K. Adhikari, C.-N. Ku, C.-L. Chiang and H. Kuo, *Int. J. Hydrogen Energy*, 2012, **37**, 13865–13871.
256 L. J. Murray, M. Dinca, J. Yano, S. Chavan, S. Bordiga, C. M. Brown and J. R. Long, *J. Am. Chem. Soc.*, 2010, **132**, 7856–7857.
257 E. Borfecchia, S. Maurelli, D. Gianolio, E. Groppo, M. Chiesa, F. Bonino and C. Lamberti, *J. Phys. Chem. C*, 2012, **116**, 19839–19850.
258 N. Nijem, K. Fürsich, H. Bluhm, S. R. Leone and M. K. Gilles, *J. Phys. Chem. C*, 2015, **119**, 24781–24788.
259 H. K. Kim, W. S. Yun, M.-B. Kim, J. Y. Kim, Y.-S. Bae, J. Lee and N. C. Jeong, *J. Am. Chem. Soc.*, 2015, **137**, 10009–10015.
260 H. Wu, J. M. Simmons, G. Srinivas, W. Zhou and T. Yildirim, *J. Phys. Chem. Lett.*, 2010, **1**, 1946–1951.
261 M. C. Brown, Y. Liu, T. Yildirim, V. K. Peterson and C. J. Kepert, *Nanotechnology*, 2009, **20**, 204025.
262 I. Krkljus and M. Hirscher, *Microporous Mesoporous Mater.*, 2011, **142**, 725–729.
263 D. F. Sava, K. W. Chapman, M. A. Rodriguez, J. A. Greathouse, P. S. Crozier, H. Zhao, P. J. Chupas and T. M. Nenoff, *Chem. Mater.*, 2013, **25**, 2591–2596.
264 S. Bordiga, L. Regli, F. Bonino, E. Groppo, C. Lamberti, B. Xiao, P. S. Wheatley, R. E. Morris and A. Zecchina, *Phys. Chem. Chem. Phys.*, 2007, **9**, 2676–2685.
265 N. Nijem, H. Bluhm, M. L. Ng, M. Kunz, S. R. Leone and M. K. Gilles, *Chem. Commun.*, 2014, **50**, 10144–10147.
266 A. H. Khan, K. Peikert, M. Fröba and M. Bertmer, *Microporous Mesoporous Mater.*, 2015, **216**, 111–117.
267 K. Peikert, L. J. McCormick, D. Cattaneo, M. J. Duncan, F. Hoffmann, A. H. Khan, M. Bertmer, R. E. Morris and M. Fröba, *Microporous Mesoporous Mater.*, 2015, **216**, 118–126.
268 B. Jee, M. Hartmann and A. Pöppl, *Mol. Phys.*, 2013, **111**, 2950–2966.
269 B. Jee, P. St. Petkov, G. N. Vayssilov, T. Heine, M. Hartmann and A. Pöppl, *J. Phys. Chem. C*, 2013, **117**, 8231–8240.
270 F. Gul-E-Noor, M. Mendt, D. Michel, A. Pöppl, H. Krautscheid, J. Haase and M. Bertmer, *J. Phys. Chem. C*, 2013, **117**, 7703–7712.
271 A. Kultaeva, W. Böhlmann, M. Hartmann, T. Biktagirov and A. Pöppl, *J. Phys. Chem. C*, 2019, **123**, 26877–26887.
272 A. Kultaeva, W. Böhlmann, M. Hartmann, T. Biktagirov and A. Pöppl, *J. Phys. Chem. Lett.*, 2019, **10**, 7657–7664.
273 D. M. Shakya, O. A. Ejegbavwo, T. Rajeshkumar, S. D. Senanayake, A. J. Brandt, S. Farzandh, N. Acharya, A. M. Ebrahim, A. I. Frenkel, N. Rui, G. L. Tate, J. R. Monnier,

Open Access Article. Published on 20 August 2020. Downloaded on 2/16/2026 6:59:12 AM.
This article is licensed under a Creative Commons Attribution 3.0 Unported Licence.

K. D. Vogiatzis, N. B. Shustova and D. A. Chen, *Angew. Chem., Int. Ed.*, 2019, **58**, 16533.
274 H. Noei, O. Kozachuk, S. Amirjalayer, S. Bureekaew, M. Kauer, R. Schmid, B. Marler, M. Muhler, R. A. Fischer and Y. Wang, *J. Phys. Chem. C*, 2013, **117**, 5658–5666.
275 I. Agirrezabal-Telleria, I. Luz, M. A. Ortuño, M. Oregui-Bengoechea, I. Gandarias, N. López, M. A. Lail and M. Soukri, *Nat. Commun.*, 2019, **10**, 2076.
276 W. R. Heinz, T. Kratky, M. Drees, A. Wimmer, O. Tomanec, S. Günther, M. Schuster and R. A. Fischer, *Dalton Trans.*, 2019, **48**, 12031–12039.
277 D. J. Xiao, E. D. Bloch, J. A. Mason, W. L. Queen, M. R. Hudson, N. Planas, J. Borycz, A. L. Dzubak, P. Verma, K. Lee, F. Bonino, V. Crocellà, J. Yano, S. Bordiga, D. G. Truhlar, L. Gagliardi, C. M. Brown and J. R. Long, *Nat. Chem.*, 2014, **6**, 590–595.
278 Y. Yue, H. Arman, Z. J. Tonzetich and B. Chen, *Z. Anorg. Allg. Chem.*, 2019, **645**, 797–800.
279 J. Bitzer, S. Otterbach, K. Thangavel, A. Kultaeva, R. Schmid, A. Poppl and W. Kleist, *Chem.*, 2020, **26**, 5667–5675.
280 W. Zhang, M. Kauer, O. Halbherr, K. Epp, P. Guo, M. I. Gonzalez, D. J. Xiao, C. Wiktor, F. X. Liabrés i Xamena, C. Wöll, Y. Wang, M. Muhler and R. A. Fischer, *Chem. – Eur. J.*, 2016, **22**, 14297–14307.
281 S. Marx, W. Kleist and A. Baiker, *J. Catal.*, 2011, **281**, 76–87.
282 L. Alaerts, E. Séguin, H. Poelman, F. Thibault-Starzyk, P. A. Jacobs and D. E. De Vos, *Chem. – Eur. J.*, 2006, **12**, 7353–7363.
283 O. Shekhah, J. Liu, R. A. Fischer and C. Woll, *Chem. Soc. Rev.*, 2011, **40**, 1081–1106.
284 J. Szanyi, M. Daturi, G. Clet, D. R. Baer and C. H. F. Peden, *Phys. Chem. Chem. Phys.*, 2012, **14**, 4383–4390.
285 P. St. Petkov, G. N. Vayssilov, J. Liu, O. Shekhah, Y. Wang, C. Wöll and T. Heine, *ChemPhysChem*, 2012, **13**, 2025–2029.
286 Z. Wang, H. Sezen, J. Liu, C. Yang, S. E. Roggenbuck, K. Peikert, M. Fröba, A. Mavrandonakis, B. Supronowicz, T. Heine, H. Gliemann and C. Wöll, *Microporous Mesoporous Mater.*, 2015, **207**, 53–60.
287 C.-Y. Wang, P. Ray, Q. Gong, Y. Zhao, J. Li and A. D. Lueking, *Phys. Chem. Chem. Phys.*, 2015, **17**, 26766–26776.
288 A. S. Duke, E. A. Dolgopolova, R. P. Galhenage, S. C. Ammal, A. Heyden, M. D. Smith, D. A. Chen and N. B. Shustova, *J. Phys. Chem. C*, 2015, **119**, 27457–27466.
289 M. Todaro, G. Buscarino, L. Sciortino, A. Alessi, F. Messina, M. Taddei, M. Ranocchiari, M. Cannas and F. M. Gelardi, *J. Phys. Chem. C*, 2016, **120**, 12879–12889.
290 M. Todaro, A. Alessi, L. Sciortino, S. Agnello, M. Cannas, F. M. Gelardi and G. Buscarino, *J. Spectrosc.*, 2016, **2016**, 7.
291 M. Todaro, L. Sciortino, F. M. Gelardi and G. Buscarino, *J. Phys. Chem. C*, 2017, **121**, 24853–24860.
292 K. Müller, N. Vankova, L. Schöttner, T. Heine and L. Heinke, *Chem. Sci.*, 2019, **10**, 153–160.
293 C. Schneider, M. Mendt, A. Pöppl, V. Crocellà and R. A. Fischer, *ACS Appl. Mater. Interfaces*, 2020, **12**, 1024–1035.
294 A. Terracina, L. N. McHugh, M. Todaro, S. Agnello, P. S. Wheatley, F. M. Gelardi, R. E. Morris and G. Buscarino, *J. Phys. Chem. C*, 2019, **123**, 28219–28232.
295 Z. Wang and S. M. Cohen, *Chem. Soc. Rev.*, 2009, **38**, 1315–1329.
296 K. K. Tanabe and S. M. Cohen, *Chem. Soc. Rev.*, 2011, **40**, 498–519.
297 Y. K. Hwang, D.-Y. Hong, J.-S. Chang, S. H. Jhung, Y.-K. Seo, J. Kim, A. Vimont, M. Daturi, C. Serre and G. Férey, *Angew. Chem., Int. Ed.*, 2008, **47**, 4144–4148.
298 K. K. Tanabe and S. M. Cohen, *Angew. Chem., Int. Ed.*, 2009, **48**, 7424–7427.
299 D. Farrusseng, J. Canivet and A. Quadrelli, *Metal-Organic Frameworks*, Wiley-VCH Verlag GmbH & Co. KGaA, 2011, pp. 23–48, DOI: 10.1002/9783527635856.ch2.
300 S. J. Garibay, Z. Wang, K. K. Tanabe and S. M. Cohen, *Inorg. Chem.*, 2009, **48**, 7341–7349.
301 K. K. Tanabe, Z. Wang and S. M. Cohen, *J. Am. Chem. Soc.*, 2008, **130**, 8508–8517.
302 Z. Yin, S. Wan, J. Yang, M. Kurmoo and M.-H. Zeng, *Coord. Chem. Rev.*, 2019, **378**, 500–512.
303 M. Meilikhov, K. Yusenko and R. A. Fischer, *J. Am. Chem. Soc.*, 2009, **131**, 9644–9645.
304 C. Larabi and E. A. Quadrelli, *Eur. J. Inorg. Chem.*, 2012, 3014–3022.
305 I. S. Kim, J. Borycz, A. E. Platero-Prats, S. Tussupbayev, T. C. Wang, O. K. Farha, J. T. Hupp, L. Gagliardi, K. W. Chapman, C. J. Cramer and A. B. F. Martinson, *Chem. Mater.*, 2015, **27**, 4772–4778.
306 Z. Li, A. W. Peters, V. Bernales, M. A. Ortuño, N. M. Schweitzer, M. R. DeStefano, L. C. Gallington, A. E. Platero-Prats, K. W. Chapman, C. J. Cramer, L. Gagliardi, J. T. Hupp and O. K. Farha, *ACS Cent. Sci.*, 2017, **3**(1), 31–38.
307 A. A. Yakovenko, J. H. Reibenspies, N. Bhuvanesh and H.-C. Zhou, *J. Appl. Crystallogr.*, 2013, **46**, 346–353.
308 A. A. Yakovenko, Z. Wei, M. Wriedt, J.-R. Li, G. J. Halder and H.-C. Zhou, *Cryst. Growth Des.*, 2014, **14**, 5397–5407.
309 I. S. Kim, S. Ahn, N. A. Vermeulen, T. E. Webber, L. C. Gallington, K. W. Chapman, R. L. Penn, J. T. Hupp, O. K. Farha, J. M. Notestein and A. B. F. Martinson, *J. Am. Chem. Soc.*, 2020, **142**, 242–250.
310 T. Drake, P. Ji and W. Lin, *Acc. Chem. Res.*, 2018, **51**, 2129–2138.
311 I. S. Kim, O. K. Farha, J. T. Hupp, L. Gagliardi, K. W. Chapman, C. Cramer and A. B. F. Martinson, *ECS Trans.*, 2016, **75**, 93–99.
312 J. E. Mondloch, W. Bury, D. Fairen-Jimenez, S. Kwon, E. J. DeMarco, M. H. Weston, A. A. Sarjeant, S. T. Nguyen, P. C. Stair, R. Q. Snurr, O. K. Farha and J. T. Hupp, *J. Am. Chem. Soc.*, 2013, **135**, 10294–10297.
313 W. Bury, O. K. Farha, J. T. Hupp and J. E. Mondloch, *US Pat.*, 20150031908A1, 2015.
314 R. C. Klet, T. C. Wang, L. E. Fernandez, D. G. Truhlar, J. T. Hupp and O. K. Farha, *Chem. Mater.*, 2016, **28**, 1213–1219.
315 S. Ahn, N. E. Thornburg, Z. Li, T. C. Wang, L. C. Gallington, K. W. Chapman, J. M. Notestein, J. T. Hupp and O. K. Farha, *Inorg. Chem.*, 2016, **55**, 11954–11961.

This journal is © The Royal Society of Chemistry 2020

Open Access Article. Published on 20 August 2020. Downloaded on 2/16/2026 6:59:12 AM.
This article is licensed under a Creative Commons Attribution 3.0 Unported Licence.

316 A. W. Peters, Z. Li, O. K. Farha and J. T. Hupp, *ACS Nano*, 2015, **9**, 8484–8490.
317 L. C. Gallington, I. S. Kim, W.-G. Liu, A. A. Yakovenko, A. E. Platero-Prats, Z. Li, T. C. Wang, J. T. Hupp, O. K. Farha, D. G. Truhlar, A. B. F. Martinson and K. W. Chapman, *J. Am. Chem. Soc.*, 2016, **138**, 13513–13516.
318 A. W. Peters, Z. Li, O. K. Farha and J. T. Hupp, *ACS Appl. Mater. Interfaces*, 2016, **8**, 20675–20681.
319 A. B. Thompson, D. R. Pahls, V. Bernales, L. C. Gallington, C. D. Malonzo, T. Webber, S. J. Tereniak, T. C. Wang, S. P. Desai, Z. Li, I. S. Kim, L. Gagliardi, R. L. Penn, K. W. Chapman, A. Stein, O. K. Farha, J. T. Hupp, A. B. F. Martinson and C. C. Lu, *Chem. Mater.*, 2016, **28**, 6753–6762.
320 D. Yang, S. O. Odoh, T. C. Wang, O. K. Farha, J. T. Hupp, C. J. Cramer, L. Gagliardi and B. C. Gates, *J. Am. Chem. Soc.*, 2015, **137**, 7391–7396.
321 D. Yang, S. O. Odoh, J. Borycz, T. C. Wang, O. K. Farha, J. T. Hupp, C. J. Cramer, L. Gagliardi and B. C. Gates, *ACS Catal.*, 2016, **6**, 235–247.
322 Z. Li, N. M. Schweitzer, A. B. League, V. Bernales, A. W. Peters, A. B. Getsoian, T. C. Wang, J. T. Miller, A. Vjunov, J. L. Fulton, J. A. Lercher, C. J. Cramer, L. Gagliardi, J. T. Hupp and O. K. Farha, *J. Am. Chem. Soc.*, 2016, **138**, 1977–1982.
323 H. G. T. Nguyen, N. M. Schweitzer, C.-Y. Chang, T. L. Drake, M. C. So, P. C. Stair, O. K. Farha, J. T. Hupp and S. T. Nguyen, *ACS Catal.*, 2014, **4**, 2496–2500.
324 R. C. Klet, S. Tussupbayev, J. Borycz, J. R. Gallagher, M. M. Stalzer, J. T. Miller, L. Gagliardi, J. T. Hupp, T. J. Marks, C. J. Cramer, M. Delferro and O. K. Farha, *J. Am. Chem. Soc.*, 2015, **137**, 15680–15683.
325 O. K. Farha, J. T. Hupp, M. Delferro and R. C. Klet, *US Pat.*, 20160046738A1, 2016.
326 S. T. Madrahimov, J. R. Gallagher, G. Zhang, Z. Meinhart, S. J. Garibay, M. Delferro, J. T. Miller, O. K. Farha, J. T. Hupp and S. T. Nguyen, *ACS Catal.*, 2015, **5**, 6713–6718.
327 M. Rimoldi, A. Nakamura, N. A. Vermeulen, J. J. Henkelis, A. K. Blackburn, J. T. Hupp, J. F. Stoddart and O. K. Farha, *Chem. Sci.*, 2016, **7**, 4980–4984.
328 Z. Li, A. W. Peters, V. Bernales, M. A. Ortuño, N. M. Schweitzer, M. R. DeStefano, L. C. Gallington, A. E. Platero-Prats, K. W. Chapman, C. J. Cramer, L. Gagliardi, J. T. Hupp and O. K. Farha, *ACS Cent. Sci.*, 2017, **3**, 31–38.
329 M. Rimoldi, V. Bernales, J. Borycz, A. Vjunov, L. C. Gallington, A. E. Platero-Prats, I. S. Kim, J. L. Fulton, A. B. F. Martinson, J. A. Lercher, K. W. Chapman, C. J. Cramer, L. Gagliardi, J. T. Hupp and O. K. Farha, *Chem. Mater.*, 2017, **29**, 1058–1068.
330 K. Manna, P. Ji, Z. Lin, F. X. Greene, A. Urban, N. C. Thacker and W. Lin, *Nat. Commun.*, 2016, **7**, 12610.
331 P. Ji, K. Manna, Z. Lin, A. Urban, F. X. Greene, G. Lan and W. Lin, *J. Am. Chem. Soc.*, 2016, **138**, 12234–12242.
332 Z. H. Syed, Z. Chen, K. B. Idrees, T. A. Goetjen, E. C. Wegener, X. Zhang, K. W. Chapman, D. M. Kaphan, M. Delferro and O. K. Farha, *Organometallics*, 2020, **39**, 1123–1133.
333 V. Bernales, D. Yang, J. Yu, G. Gümüşlü, C. J. Cramer, B. C. Gates and L. Gagliardi, *ACS Appl. Mater. Interfaces*, 2017, **9**, 33511–33520.
334 D. Yang, M. R. Momeni, H. Demir, D. R. Pahls, M. Rimoldi, T. C. Wang, O. K. Farha, J. T. Hupp, C. J. Cramer, B. C. Gates and L. Gagliardi, *Faraday Discuss.*, 2017, **201**, 195–206.
335 S. Kim In, Z. Li, J. Zheng, E. Platero-Prats Ana, A. Mavrandonakis, S. Pellizzeri, M. Ferrandon, A. Vjunov, C. Gallington Leighanne, E. Webber Thomas, A. Vermeulen Nicolaas, R. L. Penn, B. Getman Rachel, J. Cramer Christopher, W. Chapman Karena, M. Camaioni Donald, L. Fulton John, A. Lercher Johannes, K. Farha Omar, T. Hupp Joseph and B. F. Martinson Alex, *Angew. Chem., Int. Ed.*, 2018, **57**, 909–913.
336 L. R. Redfern, Z. Li, X. Zhang and O. K. Farha, *ACS Appl. Nano Mater.*, 2018, **1**, 4413–4417.
337 A. E. Platero-Prats, Z. Li, L. C. Gallington, A. W. Peters, J. T. Hupp, O. K. Farha and K. W. Chapman, *Faraday Discuss.*, 2017, **201**, 337–350.
338 J. Liu, J. Ye, Z. Li, K.-I. Otake, Y. Liao, A. W. Peters, H. Noh, D. G. Truhlar, L. Gagliardi, C. J. Cramer, O. K. Farha and J. T. Hupp, *J. Am. Chem. Soc.*, 2018, **140**, 11174–11178.
339 S. P. Desai, J. Ye, J. Zheng, M. S. Ferrandon, T. E. Webber, A. E. Platero-Prats, J. Duan, P. Garcia-Holley, D. M. Camaioni, K. W. Chapman, M. Delferro, O. K. Farha, J. L. Fulton, L. Gagliardi, J. A. Lercher, R. L. Penn, A. Stein and C. C. Lu, *J. Am. Chem. Soc.*, 2018, **140**, 15309–15318.
340 T. A. Goetjen, X. Zhang, J. Liu, J. T. Hupp and O. K. Farha, *ACS Sustainable Chem. Eng.*, 2019, **7**, 2553–2557.
341 J. Liu, L. R. Redfern, Y. Liao, T. Islamoglu, A. Atilgan, O. K. Farha and J. T. Hupp, *ACS Appl. Mater. Interfaces*, 2019, **11**, 47822–47829.
342 T. C. Wang, N. A. Vermeulen, I. S. Kim, A. B. F. Martinson, J. F. Stoddart, J. T. Hupp and O. K. Farha, *Nat. Protoc.*, 2016, **11**, 149–162.
343 M. R. Mian, L. R. Redfern, S. M. Pratik, D. Ray, J. Liu, K. B. Idrees, T. Islamoglu, L. Gagliardi and O. K. Farha, *Chem. Mater.*, 2020, **32**, 3078–3086.
344 A. E. Platero-Prats, A. Bermejo Gómez, L. Samain, X. Zou and B. Martín-Matute, *Chem. – Eur. J.*, 2014, **21**, 861–866.
345 A. E. Platero-Prats, A. Bermejo Gómez, K. W. Chapman, B. Martín-Matute and X. Zou, *CrystEngComm*, 2015, **17**, 7632–7635.
346 S. Øien, G. Agostini, S. Svelle, E. Borfecchia, K. A. Lomachenko, L. Mino, E. Gallo, S. Bordiga, U. Olsbye, K. P. Lillerud and C. Lamberti, *Chem. Mater.*, 2015, **27**, 1042–1056.
347 L. Braglia, E. Borfecchia, A. Martini, A. L. Bugaev, A. V. Soldatov, S. Øien-Ødegaard, B. T. Lønstad-Bleken, U. Olsbye, K. P. Lillerud, K. A. Lomachenko, G. Agostini, M. Manzoli and C. Lamberti, *Phys. Chem. Chem. Phys.*, 2017, **19**, 27489–27507.
348 E. S. Gutterød, S. Øien-Ødegaard, K. Bossers, A.-E. Nieuwelink, M. Manzoli, L. Braglia, A. Lazzarini, E. Borfecchia, S. Ahmadigoltapeh, B. Bouchevreau,

Open Access Article. Published on 20 August 2020. Downloaded on 2/16/2026 6:59:12 AM.
This article is licensed under a Creative Commons Attribution 3.0 Unported Licence.

B. T. Lønstad-Bleken, R. Henry, C. Lamberti, S. Bordiga, B. M. Weckhuysen, K. P. Lillerud and U. Olsbye, *Ind. Eng. Chem. Res.*, 2017, **56**, 13206–13218.

349 A. L. Bugaev, A. A. Guda, K. A. Lomachenko, E. G. Kamyshova, M. A. Soldatov, G. Kaur, S. Øien-Ødegaard, L. Braglia, A. Lazzarini, M. Manzoli, S. Bordiga, U. Olsbye, K. P. Lillerud, A. V. Soldatov and C. Lamberti, *Faraday Discuss.*, 2018, **208**, 287–306.

350 L. Braglia, E. Borfecchia, L. Maddalena, S. Øien, K. A. Lomachenko, A. L. Bugaev, S. Bordiga, A. V. Soldatov, K. P. Lillerud and C. Lamberti, *Catal. Today*, 2017, **283**, 89–103.

351 L. Braglia, E. Borfecchia, K. A. Lomachenko, A. L. Bugaev, A. A. Guda, A. V. Soldatov, B. T. L. Bleken, S. Øien-Ødegaard, U. Olsbye, K. P. Lillerud, S. Bordiga, G. Agostini, M. Manzoli and C. Lamberti, *Faraday Discuss.*, 2017, **201**, 265–286.

352 N. Van Velthoven, M. Henrion, J. Dallenes, A. Krajnc, A. L. Bugaev, P. Liu, S. Bals, A. V. Soldatov, G. Mali and D. E. De Vos, *ACS Catal.*, 2020, **10**, 5077–5085.

353 T. Toyao, K. Miyahara, M. Fujiwaki, T.-H. Kim, S. Dohshi, Y. Horiuchi and M. Matsuoka, *J. Phys. Chem. C*, 2015, **119**, 8131–8137.

354 N. Yuan, V. Pascanu, Z. Huang, A. Valiente, N. Heidenreich, S. Leubner, A. K. Inge, J. Gaar, N. Stock, I. Persson, B. Martín-Matute and X. Zou, *J. Am. Chem. Soc.*, 2018, **140**, 8206–8217.

355 J. Liu and C. Wöll, *Chem. Soc. Rev.*, 2017, **46**, 5730–5770.

356 A. Betard and R. A. Fischer, *Chem. Rev.*, 2012, **112**, 1055–1083.

357 M. Tu, S. Wannapaiboon and R. A. Fischer, *Inorg. Chem. Front.*, 2014, **1**, 442–463.

358 W. J. Li, M. Tu, R. Cao and R. A. Fischer, *J. Mater. Chem. A*, 2016, **4**, 12356–12369.

359 D. Bradshaw, A. Garai and J. Huo, *Chem. Soc. Rev.*, 2012, **41**, 2344–2381.

360 Z. G. Gu, A. Pfriem, S. Hamsch, H. Breitwieser, J. Wohlgemuth, L. Heinke, H. Gliemann and C. Woll, *Microporous Mesoporous Mater.*, 2015, **211**, 82–87.

361 L. Heinke, M. Tu, S. Wannapaiboon, R. A. Fischer and C. Woll, *Microporous Mesoporous Mater.*, 2015, **216**, 200–215.

362 O. Shekhah, H. Wang, S. Kowarik, F. Schreiber, M. Paulus, M. Tolan, C. Sternemann, F. Evers, D. Zacher, R. A. Fischer and C. Woll, *J. Am. Chem. Soc.*, 2007, **129**, 15118–15119.

363 H. Gliemann and C. Woll, *Mater. Today*, 2012, **15**, 110–116.

364 J. X. Liu, O. Shekhah, X. Stammer, H. K. Arslan, B. Liu, B. Schupbach, A. Terfort and C. Woll, *Materials*, 2012, **5**, 1581–1592.

365 O. Shekhah, H. Wang, M. Paradinas, C. Ocal, B. Schupbach, A. Terfort, D. Zacher, R. A. Fischer and C. Woll, *Nat. Mater.*, 2009, **8**, 481–484.

366 D. Zacher, R. Schmid, C. Woll and R. A. Fischer, *Angew. Chem., Int. Ed.*, 2011, **50**, 176–199.

367 J.-L. Zhuang, A. Terfort and C. Wöll, *Coord. Chem. Rev.*, 2016, **307**, 391–424.

368 B. Liu and R. A. Fischer, *Sci. China: Chem.*, 2011, **54**, 1851–1866.

369 O. Shekhah, H. Wang, T. Strunskus, P. Cyganik, D. Zacher, R. Fischer and C. Woll, *Langmuir*, 2007, **23**, 7440–7442.

370 O. Shekhah, *Materials*, 2010, **3**, 1302–1315.

371 L. D. B. Mandemaker, M. Rivera-Torrente, R. Geitner, C. M. Vis and B. M. Weckhuysen, *Angew. Chem., Int. Ed.*, 2020, DOI: 10.1002/anie.202006347.

372 G. Delen, Z. Ristanovic, L. D. B. Mandemaker and B. M. Weckhuysen, *Chem. – Eur. J.*, 2018, **24**, 187–195.

373 L. D. B. Mandemaker, M. Filez, G. Delen, H. S. Tan, X. H. Zhang, D. Lohse and B. M. Weckhuysen, *J. Phys. Chem. Lett.*, 2018, **9**, 1838–1844.

374 B. M. Weckhuysen, Z. Öztürk, R. P. Brand, J. M. Boereboom and F. Meirer, *Chem. – Eur. J.*, 2019, **25**, 8070–8084.

375 Z. Öztürk, M. Filez and M. Weckhuysen Bert, *Chem. – Eur. J.*, 2017, **23**, 10915–10924.

376 L. D. B. Mandemaker, M. Rivera-Torrente, G. Delen, J. P. Hofmann, M. Lorenz, A. Belianinov and B. M. Weckhuysen, *Chem. – Eur. J.*, 2020, **26**, 691–698.

377 M. Tu and R. A. Fischer, *J. Mater. Chem. A*, 2014, **2**, 2018–2022.

378 S. Wannapaiboon, M. Tu and R. A. Fischer, *Adv. Funct. Mater.*, 2014, **24**, 2696–2705.

379 P. De Luna, W. B. Liang, A. Mallick, O. Shekhah, F. P. G. de Arquer, A. H. Proppe, P. Todorovic, S. O. Kelley, E. H. Sargent and M. Eddaoudi, *ACS Appl. Mater. Interfaces*, 2018, **10**, 31225–31232.

380 O. Shekhah, K. Hirai, H. Wang, H. Uehara, M. Kondo, S. Diring, D. Zacher, R. A. Fischer, O. Sakata, S. Kitagawa, S. Furukawa and C. Woll, *Dalton Trans.*, 2011, **40**, 4954–4958.

381 Y. Yoo and H. K. Jeong, *Cryst. Growth Des.*, 2010, **10**, 1283–1288.

382 Z. B. Wang, J. X. Liu, B. Lukose, Z. G. Gu, P. G. Weidler, H. Gliemann, T. Heine and C. Woll, *Nano Lett.*, 2014, **14**, 1526–1529.

383 K. L. Mulfort, O. K. Farha, C. D. Malliakas, M. G. Kanatzidis and J. T. Hupp, *Chem. – Eur. J.*, 2010, **16**, 276–281.

384 R. P. Brand, L. D. B. Mandemaker, G. Delen, N. Rijnveld and B. M. Weckhuysen, *ChemPhysChem*, 2018, **19**, 2397–2404.

385 S. M. J. Rogge, A. Bavykina, J. Hajek, H. Garcia, A. I. Olivos-Suarez, A. Sepulveda-Escribano, A. Vimont, G. Clet, P. Bazin, F. Kapteijn, M. Daturi, E. V. Ramos-Fernandez, F. X. Llabres i Xamena, V. Van Speybroeck and J. Gascon, *Chem. Soc. Rev.*, 2017, **46**, 3134–3184.

386 C. J. Doonan and C. J. Sumby, *CrystEngComm*, 2017, **19**, 4044–4048.

387 A. Burgun, C. J. Coghlan, D. M. Huang, W. Chen, S. Horike, S. Kitagawa, J. F. Alvino, G. F. Metha, C. J. Sumby and C. J. Doonan, *Angew. Chem., Int. Ed.*, 2017, **56**, 8412–8416.

388 R. Peralta, M. Huxley, R. Young, O. M. Linder-Patton, J. D. Evans, C. J. Doonan and C. J. Sumby, *Faraday Discuss.*, 2020, DOI: 10.1039/D0FD00012D.

 This journal is © The Royal Society of Chemistry 2020

Open Access Article. Published on 20 August 2020. Downloaded on 2/16/2026 6:59:12 AM. This article is licensed under a Creative Commons Attribution 3.0 Unported Licence.

389 R. J. Young, M. T. Huxley, E. Pardo, N. R. Champness, C. J. Sumby and C. J. Doonan, *Chem. Sci.*, 2020, **11**, 4031–4050.
390 J. D. Evans, C. J. Sumby and C. J. Doonan, *Chem. Soc. Rev.*, 2014, **43**, 5933–5951.
391 Z. Huang, M. Ge, F. Carraro, C. J. Doonan, P. Falcaro and X. Zou, *Faraday Discuss.*, 2020, DOI: 10.1039/D0FD00015A.
392 V. Bon, E. Brunner, A. Pöppl and S. Kaskel, *Adv. Funct. Mater.*, 2020, 1907847.
393 M. C. Simons, J. G. Vitillo, M. Babucci, A. S. Hoffman, A. Boubnov, M. L. Beauvais, Z. Chen, C. J. Cramer, K. W. Chapman, S. R. Bare, B. C. Gates, C. C. Lu, L. Gagliardi and A. Bhan, *J. Am. Chem. Soc.*, 2019, **141**, 18142–18151.
394 Z. L. Fang, B. Bueken, D. E. De Vos and R. A. Fischer, *Angew. Chem., Int. Ed.*, 2015, **54**, 7234–7254.
395 R. A. Dodson, A. G. Wong-Foy and A. J. Matzger, *Chem. Mater.*, 2018, **30**, 6559–6565.
396 R. Medishetty, J. K. Zaręba, D. Mayer, M. Samoć and R. A. Fischer, *Chem. Soc. Rev.*, 2017, **46**, 4976–5004.
397 L. R. Mingabudinova, V. V. Vinogradov, V. A. Milichko, E. Hey-Hawkins and A. V. Vinogradov, *Chem. Soc. Rev.*, 2016, **45**, 5408–5431.
398 P. Horcajada, R. Gref, T. Baati, P. K. Allan, G. Maurin, P. Couvreur, G. Férey, R. E. Morris and C. Serre, *Chem. Rev.*, 2012, **112**, 1232–1268.
399 A. Dhakshinamoorthy, Z. Li and H. Garcia, *Chem. Soc. Rev.*, 2018, **47**, 8134–8172.
400 M. F. de Lange, K. J. F. M. Verouden, T. J. H. Vlugt, J. Gascon and F. Kapteijn, *Chem. Rev.*, 2015, **115**, 12205–12250.
401 A. A. Talin, A. Centrone, A. C. Ford, M. E. Foster, V. Stavila, P. Haney, R. A. Kinney, V. Szalai, F. El Gabaly, H. P. Yoon, F. Léonard and M. D. Allendorf, *Science*, 2014, **343**, 66.
402 L. Sun, G. Campbell Michael and M. Dincă, *Angew. Chem., Int. Ed.*, 2016, **55**, 3566–3579.
403 C. Schneider, D. Ukaj, R. Koerver, A. A. Talin, G. Kieslich, S. P. Pujari, H. Zuilhof, J. Janek, M. D. Allendorf and R. A. Fischer, *Chem. Sci.*, 2018, **9**, 7405–7412.
404 L. E. Kreno, K. Leong, O. K. Farha, M. Allendorf, R. P. Van Duyne and J. T. Hupp, *Chem. Rev.*, 2012, **112**, 1105–1125.
405 F. Nouar, T. Devic, H. Chevreau, N. Guillou, E. Gibson, G. Clet, M. Daturi, A. Vimont, J. M. Grenèche, M. I. Breeze, R. I. Walton, P. L. Llewellyn and C. Serre, *Chem. Commun.*, 2012, **48**, 10237–10239.
406 M. I. Breeze, G. Clet, B. C. Campo, A. Vimont, M. Daturi, J.-M. Grenèche, A. J. Dent, F. Millange and R. I. Walton, *Inorg. Chem.*, 2013, **52**, 8171–8182.
407 L. Mitchell, P. Williamson, B. Ehrlichová, A. E. Anderson, V. R. Seymour, S. E. Ashbrook, N. Acerbi, L. M. Daniels, R. I. Walton, M. L. Clarke and P. A. Wright, *Chem. – Eur. J.*, 2014, **20**, 17185–17197.
408 L. M. Aguirre-Díaz, F. Gándara, M. Iglesias, N. Snejko, E. Gutiérrez-Puebla and M. Á. Monge, *J. Am. Chem. Soc.*, 2015, **137**, 6132–6135.
409 C. Castillo-Blas and F. Gándara, *Isr. J. Chem.*, 2018, **58**, 1036–1043.
410 A. D. Burrows, *CrystEngComm*, 2011, **13**, 3623–3642.
411 M. Giménez-Marqués, A. Santiago-Portillo, S. Navalón, M. Álvaro, V. Briois, F. Nouar, H. Garcia and C. Serre, *J. Mater. Chem. A*, 2019, **7**, 20285–20292.
412 A. F. Sapnik, H. S. Geddes, E. M. Reynolds, H. H. M. Yeung and A. L. Goodwin, *Chem. Commun.*, 2018, **54**, 9651–9654.
413 C. Castillo-Blas, N. López-Salas, M. C. Gutiérrez, I. Puente-Orench, E. Gutiérrez-Puebla, M. L. Ferrer, M. Á. Monge and F. Gándara, *J. Am. Chem. Soc.*, 2019, **141**, 1766–1774.
414 D. Zhang, Y. Zhu, L. Liu, X. Ying, C.-E. Hsiung, R. Sougrat, K. Li and Y. Han, *Science*, 2018, **359**, 675.
415 L. Zhu, D. Zhang, M. Xue, H. Li and S. Qiu, *CrystEngComm*, 2013, **15**, 9356–9359.
416 Q. Chen, C. Dwyer, G. Sheng, C. Zhu, X. Li, C. Zheng and Y. Zhu, *Adv. Mater.*, 2020, **32**, e1907619.
417 T.-Y. Luo, C. Liu, X. Y. Gan, P. F. Muldoon, N. A. Diemler, J. E. Millstone and N. L. Rosi, *J. Am. Chem. Soc.*, 2019, **141**, 2161–2168.
418 X. Kong, H. Deng, F. Yan, J. Kim, J. A. Swisher, B. Smit, O. M. Yaghi and J. A. Reimer, *Science*, 2013, **341**, 882–885.
419 A. M. Katzenmeyer, J. Canivet, G. Holland, D. Farrusseng and A. Centrone, *Angew. Chem., Int. Ed.*, 2014, **53**, 2852–2856.
420 J. Lyu, X. Gong, S.-J. Lee, K. Gnanasekaran, X. Zhang, M. C. Wasson, X. Wang, P. Bai, X. Guo, N. C. Gianneschi and O. K. Farha, *J. Am. Chem. Soc.*, 2020, **142**, 4609–4615.
421 I. L. C. Buurmans and B. M. Weckhuysen, *Nat. Chem.*, 2012, **4**, 873–886.
422 N. Kumar, B. Stephanidis, R. Zenobi, A. J. Wain and D. Roy, *Nanoscale*, 2015, **7**, 7133–7137.
423 F. Meirer, D. T. Morris, S. Kalirai, Y. Liu, J. C. Andrews and B. M. Weckhuysen, *J. Am. Chem. Soc.*, 2015, **137**, 102–105.
424 T. Hartman, C. S. Wondergem, N. Kumar, A. van den Berg and B. M. Weckhuysen, *J. Phys. Chem. Lett.*, 2016, **7**, 1570–1584.
425 D. E. Perea, I. Arslan, J. Liu, Z. Ristanovic, L. Kovarik, B. W. Arey, J. A. Lercher, S. R. Bare and B. M. Weckhuysen, *Nat. Commun.*, 2015, **6**, 7589.
426 K. C. Jayachandrababu, D. S. Sholl and S. Nair, *J. Am. Chem. Soc.*, 2017, **139**, 5906–5915.
427 W. Schrimpf, J. Jiang, Z. Ji, P. Hirschle, D. C. Lamb, O. M. Yaghi and S. Wuttke, *Nat. Commun.*, 2018, **9**, 1647.
428 A. Ghosh, P. Mukherjee, S. Deb and R. Bhargava, *J. Phys. Chem. Lett.*, 2017, **8**, 5325–5330.
429 O. I. Lebedev, F. Millange, C. Serre, G. Van Tendeloo and G. Férey, *Chem. Mater.*, 2005, **17**, 6525–6527.
430 A. Mayoral, M. Sanchez-Sanchez, A. Alfayate, J. Perez-Pariente and I. Diaz, *ChemCatChem*, 2015, **7**, 3719–3724.
431 A. Mayoral, R. Mahugo, M. Sánchez-Sánchez and I. Díaz, *ChemCatChem*, 2017, **9**, 3497–3502.
432 M. Rivera-Torrente, M. Filez, F. Meirer and B. M. Weckhuysen, *Chem. – Eur. J.*, 2020, **26**, 3614–3625.
433 M. Rivera-Torrente, M. Filez, C. Schneider, E. C. van der Feltz, K. Wolkersdörfer, D. H. Taffa, M. Wark, R. A. Fischer and B. M. Weckhuysen, *Phys. Chem. Chem. Phys.*, 2019, **21**, 25678–25689.

Open Access Article. Published on 20 August 2020. Downloaded on 2/16/2026 6:59:12 AM.
This article is licensed under a Creative Commons Attribution 3.0 Unported Licence.

434 X. Cao, S. Hong, Z. Jiang, Y. She, S. Wang, C. Zhang, H. Li, F. Jin, M. Jin and J. Wang, *Analyst*, 2017, **142**, 2640–2647.
435 K. Sugikawa, Y. Furukawa and K. Sada, *Chem. Mater.*, 2011, **23**, 3132–3134.
436 X. Ma, S. Wen, X. Xue, Y. Guo, J. Jin, W. Song and B. Zhao, *ACS Appl. Mater. Interfaces*, 2018, **10**, 25726–25736.
437 Y. Cai, Y. Wu, T. Xuan, X. Guo, Y. Wen and H. Yang, *ACS Appl. Mater. Interfaces*, 2018, **10**, 15412–15417.
438 X. Qiao, B. Su, C. Liu, Q. Song, D. Luo, G. Mo and T. Wang, *Adv. Mater.*, 2018, **30**, 1702275.
439 Z. Jiang, P. Gao, L. Yang, C. Huang and Y. Li, *Anal. Chem.*, 2015, **87**, 12177–12182.
440 C. S. L. Koh, H. K. Lee, X. Han, H. Y. F. Sim and X. Y. Ling, *Chem. Commun.*, 2018, **54**, 2546–2549.
441 X. Kuang, S. Ye, X. Li, Y. Ma, C. Zhang and B. Tang, *Chem. Commun.*, 2016, **52**, 5432–5435.
442 G. Zheng, S. de Marchi, V. López-Puente, K. Sentosun, L. Polavarapu, I. Pérez-Juste, E. H. Hill, S. Bals, L. M. Liz-Marzán, I. Pastoriza-Santos and J. Pérez-Juste, *Small*, 2016, **12**, 3935–3943.
443 Y. Zhao, N. Kornienko, Z. Liu, C. Zhu, S. Asahina, T.-R. Kuo, W. Bao, C. Xie, A. Hexemer, O. Terasaki, P. Yang and O. M. Yaghi, *J. Am. Chem. Soc.*, 2015, **137**, 2199–2202.
444 H. Y. F. Sim, H. K. Lee, X. Han, C. S. L. Koh, G. C. Phan-Quang, C. L. Lay, Y.-C. Kao, I. Y. Phang, E. K. L. Yeow and X. Y. Ling, *Angew. Chem., Int. Ed.*, 2018, **57**, 17058–17062.
445 T.-H. Yu, C.-H. Ho, C.-Y. Wu, C.-H. Chien, C.-H. Lin and S. Lee, *J. Raman Spectrosc.*, 2013, **44**, 1506–1511.
446 H. Sun, S. Cong, Z. Zheng, Z. Wang, Z. Chen and Z. Zhao, *J. Am. Chem. Soc.*, 2019, **141**, 870–878.
447 E. S. Gutterød, A. Lazzarini, T. Fjermestad, G. Kaur, M. Manzoli, S. Bordiga, S. Svelle, K. P. Lillerud, E. Skúlason, S. Øien-Ødegaard, A. Nova and U. Olsbye, *J. Am. Chem. Soc.*, 2020, **142**, 999–1009.
448 Y. Chen, O. Sakata, Y. Nanba, L. S. R. Kumara, A. Yang, C. Song, M. Koyama, G. Li, H. Kobayashi and H. Kitagawa, *Commun. Chem.*, 2018, **1**, 61.
449 M. Köppen, A. Dhakshinamoorthy, A. K. Inge, O. Cheung, J. Ångström, P. Mayer and N. Stock, *Eur. J. Inorg. Chem.*, 2018, 3496–3503.
450 N. Heidenreich, S. Waitschat and H. Reinsch, *Z. Anorg. Allg. Chem.*, 2018, **644**, 1826–1831.
451 S. Van Cleuvenbergen, Z. J. Smith, O. Deschaume, C. Bartic, S. Wachsmann-Hogiu, T. Verbiest and M. A. van der Veen, *Nat. Commun.*, 2018, **9**, 3418.
452 N. Hosono, A. Terashima, S. Kusaka, R. Matsuda and S. Kitagawa, *Nat. Chem.*, 2019, **11**, 109–116.
453 F. C. Hendriks, D. Valencia, P. C. A. Bruijnincx and B. M. Weckhuysen, *Phys. Chem. Chem. Phys.*, 2017, **19**, 1857–1867.
454 F. C. Hendriks, J. E. Schmidt, J. A. Rombouts, K. Lammertsma, P. C. A. Bruijnincx and B. M. Weckhuysen, *Chem. – Eur. J.*, 2017, **23**, 6305–6314.
455 F. C. Hendriks, F. Meirer, A. V. Kubarev, Z. Ristanović, M. B. J. Roeffaers, E. T. C. Vogt, P. C. A. Bruijnincx and B. M. Weckhuysen, *J. Am. Chem. Soc.*, 2017, **139**, 13632–13635.
456 F. C. Hendriks, S. Mohammadian, Z. Ristanović, S. Kalirai, F. Meirer, E. T. C. Vogt, P. C. A. Bruijnincx, H. C. Gerritsen and B. M. Weckhuysen, *Angew. Chem., Int. Ed.*, 2018, **57**, 257–261.
457 G. T. Whiting, N. Nikolopoulos, I. Nikolopoulos, A. D. Chowdhury and B. M. Weckhuysen, *Nat. Chem.*, 2019, **11**, 23–31.
458 Z. Ristanović, A. V. Kubarev, J. Hofkens, M. B. J. Roeffaers and B. M. Weckhuysen, *J. Am. Chem. Soc.*, 2016, **138**, 13586–13596.
459 Z. Ristanović, M. M. Kerssens, A. V. Kubarev, F. C. Hendriks, P. Dedecker, J. Hofkens, M. B. J. Roeffaers and B. M. Weckhuysen, *Angew. Chem., Int. Ed.*, 2015, **54**, 1836–1840.
460 G. Fleury, J. A. Steele, I. C. Gerber, F. Jolibois, P. Puech, K. Muraoka, S. H. Keoh, W. Chaikittisilp, T. Okubo and M. B. J. Roeffaers, *J. Phys. Chem. Lett.*, 2018, **9**, 1778–1782.
461 F. Meirer, S. Kalirai, D. Morris, S. Soparawalla, Y. Liu, G. Mesu, J. C. Andrews and B. M. Weckhuysen, *Sci. Adv.*, 2015, **1**, e1400199.
462 I. Strauss, A. Mundstock, D. Hinrichs, R. Himstedt, A. Knebel, C. Reinhardt, D. Dorfs and J. Caro, *Angew. Chem., Int. Ed.*, 2018, **57**, 7434–7439.
463 X. Teng, F. Li and C. Lu, *Chem. Soc. Rev.*, 2020, **49**, 2408–2425.
464 Y. Shen, B. Shan, B. Mu and S. Tongay, *Angew. Chem., Int. Ed.*, 2020, **59**, 9408.
465 D. N. Johnstone, F. C. N. Firth, C. P. Grey, P. A. Midgley, M. J. Cliffe and S. M. Collins, *J. Am. Chem. Soc.*, 2020, **142**(30), 13081–13089.

This journal is © The Royal Society of Chemistry 2020